AD-A068 462 GENERAL ELECTRIC CO ALBUQUERQUE N MEX TEMPO F/G 19/4
HIGH EXPLOSIVE MULTIBURST AIRBLAST PHENOMENA (SIMULTANEOUS AND --ETC(U)
FEB 79 R E REISLER, L W KENNEDY, J H KEEFER DNA001-77-C-0305
UNCLASSIFIED ARBRL-TR-02142 NL

1 OF 2
AD
A068462

(12) LEVEL VII

AD-E430 208

TECHNICAL REPORT ARBRL-TR-02142

HIGH EXPLOSIVE MULTIBURST AIRBLAST PHENOMENA (SIMULTANEOUS AND NON-SIMULTANEOUS DETONATIONS)

Ralph E. Reisler
Lynn W. Kennedy
John H. Keefer

February 1979

US ARMY ARMAMENT RESEARCH AND DEVELOPMENT COMMAND
BALLISTIC RESEARCH LABORATORY
ABERDEEN PROVING GROUND, MARYLAND

Destroy this report when it is no longer needed.
Do not return it to the originator.

Secondary distribution of this report by originating or sponsoring activity is prohibited.

Additional copies of this report may be obtained from the National Technical Information Service, U.S. Department of Commerce, Springfield, Virginia 22161.

The findings in this report are not to be construed as an official Department of the Army position, unless so designated by other authorized documents.

The use of trade names or manufacturers' names in this report does not constitute indorsement of any commercial product.

UNCLASSIFIED

SECURITY CLASSIFICATION OF THIS PAGE *(When Data Entered)*

REPORT DOCUMENTATION PAGE		READ INSTRUCTIONS BEFORE COMPLETING FORM
1. REPORT NUMBER TECHNICAL REPORT ARBRL-TR-02142	2. GOVT ACCESSION NO.	3. RECIPIENT'S CATALOG NUMBER
4. TITLE *(and Subtitle)* HIGH EXPLOSIVE MULTIBURST AIRBLAST PHENOMENA (SIMULTANEOUS AND NON-SIMULTANEOUS DETONATIONS)		5. TYPE OF REPORT & PERIOD COVERED Final 6. PERFORMING ORG. REPORT NUMBER
7. AUTHOR(s) Ralph E. Reisler (BRL) Lynn W. Kennedy (GE-TEMPO) John H. Keefer (BRL)		8. CONTRACT OR GRANT NUMBER(s) DNA 001-77-C-0305
9. PERFORMING ORGANIZATION NAME AND ADDRESS USA Armament Research & Development Command USA Ballistic Research Laboratory (DRDAR-BLT) Aberdeen Proving Ground, MD 21005		10. PROGRAM ELEMENT, PROJECT, TASK AREA & WORK UNIT NUMBERS NWED-62704H-N99QAXA-A111-14
11. CONTROLLING OFFICE NAME AND ADDRESS Defense Nuclear Agency Washington, DC 20305		12. REPORT DATE FEBRUARY 1979 13. NUMBER OF PAGES 131
14. MONITORING AGENCY NAME & ADDRESS*(if different from Controlling Office)*		15. SECURITY CLASS. *(of this report)* UNCLASSIFIED 15a. DECLASSIFICATION/DOWNGRADING SCHEDULE

16. DISTRIBUTION STATEMENT *(of this Report)*

Approved for public release; distribution unlimited.

17. DISTRIBUTION STATEMENT *(of the abstract entered in Block 20, if different from Report)*

18. SUPPLEMENTARY NOTES

19. KEY WORDS *(Continue on reverse side if necessary and identify by block number)*

Air Blast
Multiburst Detonations
Hydrodynamic Airblast Codes
High Explosives
TNT or Pentolite Charges
Non-Simultaneous Detonations

20. ABSTRACT *(Continue on reverse side if necessary and identify by block number)*

This document is the final summary report on a series of sixteen high explosive multiburst detonations which were carried out as part of Project DIPOLE WEST. The series was conducted during the summers of 1973, 1974, and 1975 at the Defence Research Establishment, Suffield, Alberta, Canada, and was sponsored by the Defense Nuclear Agency.

The sixteen events were divided into three ph[illegible]. In the first phase, two charges at the same elevation [illegible] were detonated simultaneously. In the second pha[illegible] one above the

DD FORM 1 JAN 73 1473 EDITION OF 1 NOV 65 IS OB[illegible]

UNCLASSIFIED

SECURITY CLASSIFICATION OF THIS PAGE *(When Data Entered)*

20. (cont'd)

other, but still detonated simultaneously. Finally, in the third phase, vertically separated, non-simultaneous detonations were investigated.

The report summarizes the information obtained from electronic pressure transducers and from high-speed photography. The latter was subjected to extensive photogrammetric analysis. Significant insight into the redistribution of energy in blast waves as they pass over real and ideal surfaces was gained, and information was obtained about the interaction of Mach stem shocks under various conditions. General validation of hydrodynamic calculational techniques, plus the development of code modifications appropriate for multiburst situations, was a major accomplishment from this analysis.

FOREWORD

This document is the final summary report on a series of high explosive multiburst detonations which were carried out as part of Project DIPOLE WEST. The series was detonated during the summers of 1973, 1974, and 1975 at the Defence Research Establishment, Suffield (DRES) in Alberta, Canada. A number of earlier reports have been published presenting the data obtained from these tests. The present report summarizes this information and discusses conclusions reached as a result of analysis of the data.

The DIPOLE WEST project and subsequent analysis were sponsored by the Defense Nuclear Agency (DNA) and were executed under the direct management of Mr. James F. Moulton, Jr., Chief, Aerospace Systems Division, DNA. The staff at DRES, along with Mr. A.P.R. Lambert, Canadian General Electric, provided expert assistance and excellent support during fielding of the project. This support is gratefully acknowledged. Participants with major responsibilities in data collection and analysis were Dr. John Dewey, University of Victoria; Mr. Charles Needham, Air Force Weapons Laboratory; and Mr. John Wisotski, Denver Research Institute.

TABLE OF CONTENTS

LIST OF ILLUSTRATIONS

List of Illustrations (cont'd)

List of Illustrations (cont'd)

List of Illustrations (cont'd)

List of Illustrations (cont'd)

List of Illustrations (cont'd)

LIST OF TABLES

Chapter 1

INTRODUCTION

1.1 Background

Over the past five or six years, interest of the defense community has been turning away from consideration of the effects of large, devastating nuclear encounters toward consideration of "tactical" conflicts, in which a number of smaller weapons, specifically designed to destroy or damage certain targets, would be fired by both sides. This new interest opens questions which had previously been of only peripheral significance, and requires a whole new spectrum of nuclear effects information.

One area in which there has been considerable interest is that of multiburst phenomena. If two (or more) weapons are detonated at the same or nearly the same time in the same general vicinity, how will the nuclear effects combine to produce the environment that is experienced by the target? It is obvious that a large number of battle scenarios are possible. In attempting to answer the question, many scenarios have been studied using computer codes to model the various detonations. The results have been consistent for the most part if a quality model is used, and a high degree of confidence is placed on these results.

Models, however, should always be subject to experimental verification. It is not feasible, of course, to reproduce the postulated nuclear encounter by detonating a series of nuclear weapons. Certain effects of interest, however, specifically air blast effects, can be well simulated using conventional high explosives such as TNT or pentolite. With this in mind, the multiburst phases of the DIPOLE WEST experimental test series were planned. The overall objective was to verify and develop the Low Altitude Multiple Burst (LAMB) computer model (Reference 1), and at the same time to obtain some experimental information about shock-fireball, shock-shock, and shock-ground surface interactions in a multiburst situation.

1.2 The DIPOLE WEST Multiburst Program

Specific experiments were conducted with charges weighing 490 kilograms (1080 pounds) and 98 kilograms (216 pounds) under a Defense

---

1. *C. E. Needham and L. A. Wittwer, "The Air Force Weapons Laboratory Low Altitude Multiple Burst (LAMB) Model," AFWL-DYT-75-2, Air Force Weapons Laboratory, Kirtland Air Force Base, New Mexico 87117 (unpublished).*

Nuclear Agency (DNA) sponsored program. Both pentolite and TNT charges were used. The program was carried out at the Defence Research Establishment, Suffield (DRES) near Medicine Hat in Alberta, Canada, between the summer of 1973 and the spring of 1975. The experimental program was divided into three phases, as outlined in Table 1.1.

In the first phase, two charges were detonated in the same horizontal plane. An illustration of the shock interactions, with each other and with the ground, for a horizontally separated two-charge detonation is given in Figure 1.1. Charge separation distances of approximately one, two, and three fireball radii were used for this phase. The fireball radius for a 454-kilogram (1000-pound) detonation is about 15.2 metres (50 feet). The three-fireball-radius separation event was actually fired with a distance between charges of 50.5 metres (165 feet) in order to insure that pressure equilibrium of the fireballs would be attained before the shock wave from the adjacent burst arrived at the fireball surface. The first phase was designed to examine the effects of an incident shock wave on fireball deformation and on fireball rise characteristics. The effects of neighboring fireball flow fields on fireball rise and expansion were also of interest. The charges were detonated at heights of approximately 40 metres (130 feet) so that ground reflections during the early stages of the interaction could be neglected.

In the second phase, the charges were placed one above the other in a vertical plane. This arrangement, first used by the Swedish scientists Karlsson and Wagner (Reference 2), provides both an ideal and a real shock reaction plane when the charges are detonated simultaneously. The real plane is the ground surface, and the ideal plane lies midway between charges, perpendicular to a line joining the charge centers. A three-dimensional visualization of the shocks produced by the simultaneous detonation of two vertically separated charges is shown in Figure 1.2. A lack of symmetry caused by the fact that the line joining the two charge centers may not be exactly vertical has been exaggerated in the diagram.

The Phase II experiments utilized vertical charge separation distances of approximately 15.2 metres (50 feet) and 9.1 metres (30 feet). The height of the lower charge above the ground was in each case approximately half the charge separation distance. These experiments were designed to examine shock interactions from real and ideal reflecting surfaces as well as to investigate shock/fireball interactions and fireball growth and rise. The smaller charge separation

---

2. *A. Karlsson and H. Wagner, "Photographic Study of the Reflection of Spherical Shock Waves, Mach Front Formation, and Front Velocities," August 1961. Translation by SCITRAN (Scientific Translation Service), Santa Barbara, California 93108.*

Table 1.1. Events Comprising DIPOLE WEST Multiburst Test Series

Shot No.	Date Fired	Total Charge Weight (kg)	(lb)	No. and Material of Chgs.	Distance Between Charges (m)	(ft)	Height of Burst Upper (m)	(ft)	Lower (m)	(ft)	Time Between Bursts (ms)	Surface Condition
Phase I: Horizontal Charge Separation; Simultaneous Detonation												
1	6 July 73	489.9	1080	1 Pent	-	-	37.86	124.21	-	-	0	
2	12 July 73	985.2	2172	2 TNT	30.67	100.61	38.44	126.10	38.31	125.68	0	Smooth (Treated alluvium)
3	18 July 73	985.2	2172	2 TNT	15.15	49.72	39.03	128.05	38.99	127.92	0	
4	24 July 73	985.2	2172	2 TNT	50.46	165.55	40.23	131.99	40.14	131.69	0	
5	26 July 73	979.7	2160	2 Pent	30.53	100.15	39.38	129.19	39.15	128.46	0	
6	31 July 73	492.6	1086	1 TNT	-	-	40.75	133.71	-	-	0	
Phase II: Vertical Charge Separation; Simultaneous Detonation												
7	4 Sept 73	979.7	2160	2 Pent	14.24	46.73	22.00	72.19	7.76	25.46	0	Smooth (Treated alluvium)
8	17 Sept 73	979.7	2160	2 Pent	15.20	49.86	22.65	74.31	7.45	24.45	0	
9	22 Oct 73	979.7	2160	2 Pent	9.24	30.30	13.85	45.45	4.62	15.15	0	
10	2 Nov 73	979.7	2160	2 Pent	9.31	30.54	13.86	45.46	4.55	14.92	0	Rough (Furrowed)
11	8 Nov 73	979.7	2160	2 Pent	15.28	50.13	22.59	74.12	7.31	23.99	0	
Phase III: Vertical Charge Separation; Non-Simultaneous Detonations												
12	24 Oct 74	196.0	432	2 Pent	9.18	30.11	13.67	44.85	4.49	14.74	0	Smooth (asphalt)
13	28 Oct 74	196.0	432	2 Pent	9.15	30.02	13.68	44.87	4.53	14.86	10.09	
14	30 Oct 74	98.0	216	1 Pent	-	-	4.53	14.86	-	-	-	
15	1 Nov 74	196.0	432	2 Pent	9.17	30.09	13.70	44.96	4.53	14.87	5.09	
16	10 June 75	196.0	432	2 Pent	9.23	30.29	13.82	45.34	4.59	15.05	2.90	

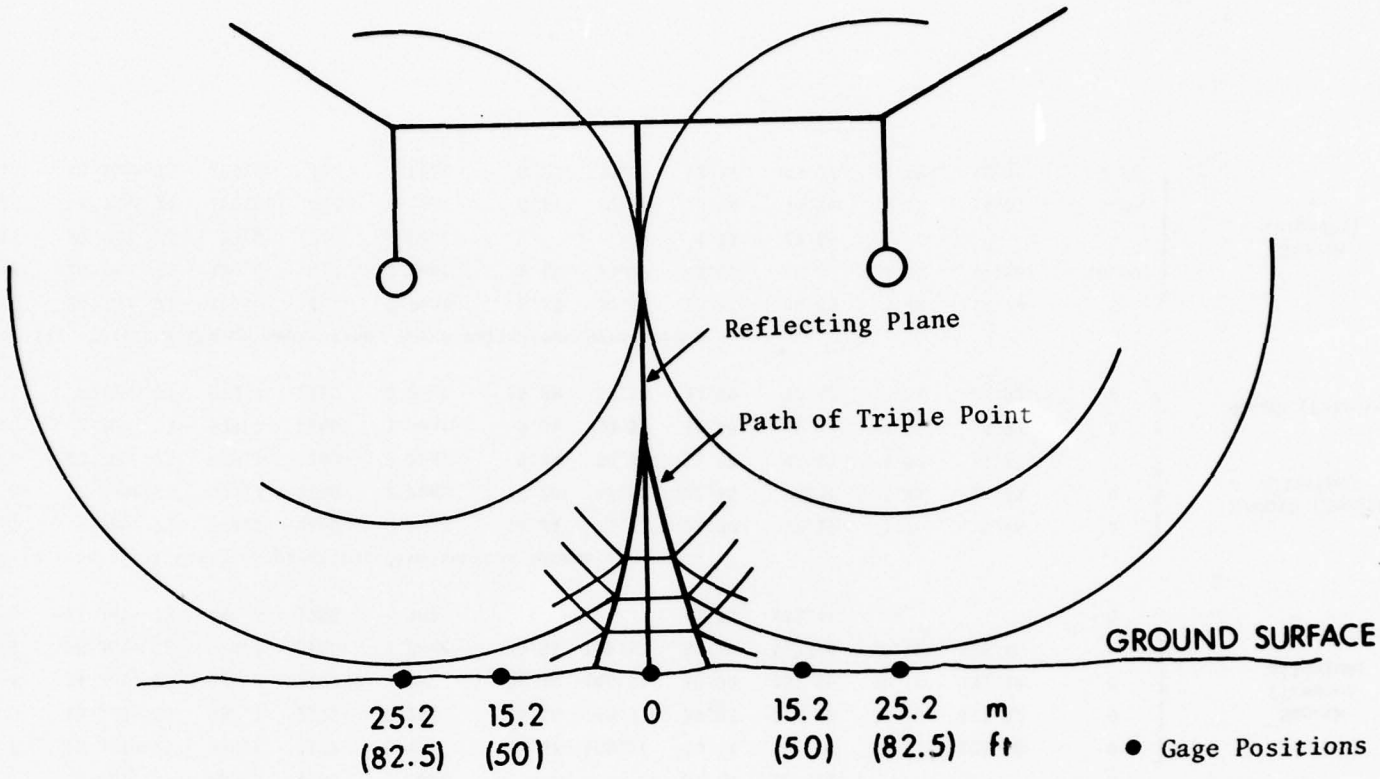

Figure 1.1. Shock Interactions for the Horizontally-Separated, Two-Charge Configuration

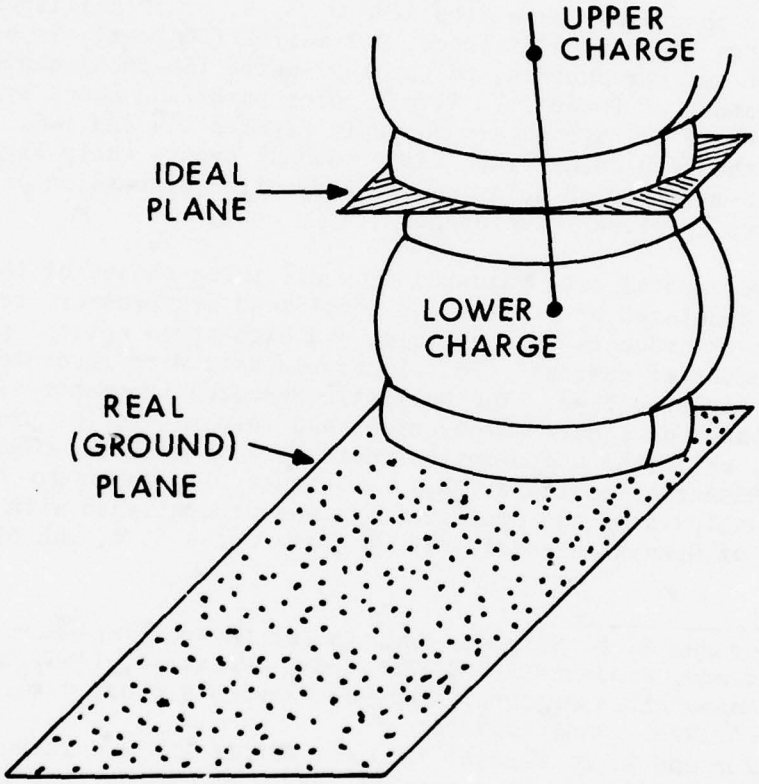

Figure 1.2. Three-Dimensional View of Shocks Produced by the Vertically-Separated Charge Configuration

distance experiments were performed to obtain information in the strong-shock interaction region.

Two types of real reflecting surfaces were used. The surface for the first three shots in Phase II was the original hard, smooth prairie soil. For the last two shots, the ground was plowed and furrowed to provide a soft, rough surface. Illustrated in Figure 1.3 are triple-point paths and shocks resulting from detonation over the two types of surfaces. Details are given in Reference 3.

The Phase III experiments were designed to provide information on the shock interaction effects of non-simultaneous detonations. Pentolite charges containing 98 kilograms (216 pounds) of explosive were used in Phase III. In these experiments the upper charge was detonated first; the lower charge was then detonated 0, 3, 5, or 10 milliseconds later. The charge separation distance, 9.2 metres (30 feet), is equivalent, using the smaller charges, to the 15.2-metre (50-foot) charge separation distance of Phase II. Triple-point paths and shock systems for two of the Phase III events are shown in Figures 1.4 and 1.5. Figure 1.4 is for the zero delay time (simultaneous) event, while Figure 1.5 is for the 5-millisecond delay shot. A detailed discussion of these two figures is given in Reference 4.

The experimental data gathered from all three phases of the multiburst series consisted of side-on and total head overpressure records from electronic transducers in the field, and high-speed optical photography from a number of cameras. The electronic data were recorded in analog form on magnetic tape. The Ballistic Research Laboratory (BRL), with the assistance of Bendix Corporation, was responsible for pressure data recording, while the photo-optical data were obtained by DRES and by the Denver Research Institute (DRI) (Reference 5). Analog-to-digital reduction and analysis of the pressure data was accomplished with the assistance of General Electric—TEMPO (References 3, 4, and 6); the

---

3. *J. H. Keefer and R. E. Reisler, "Multiburst Environment—Simultaneous Detonations, Project DIPOLE WEST," BRL Report No. 1766, USA Ballistic Research Laboratory, Aberdeen Proving Ground, Maryland 21005, March 1975. (AD# A009485)*
4. *R. E. Reisler and B. A. Pettit, "Project DIPOLE WEST—Multiburst Environment (Non-Simultaneous Detonations)," BRL Report No. 1921, USA Ballistic Research Laboratory, Aberdeen Proving Ground, Maryland 21005, September 1976. (AD# A031985)*
5. *John Wisotsky, "DIPOLE WEST Technical Photography," Denver Research Institute, University of Denver, Denver, Colorado 80208, DNA 4325F, Defense Nuclear Agency, Washington, D. C. 20305, February 1977*
6. *R. E. Reisler and L. W. Kennedy, "Air Blast Dynamic Pressures from Simultaneous and Non-Simultaneous Multiburst Detonations," BRL Report TR-02043, USA Ballistic Research Laboratory, Aberdeen Proving Ground, Maryland 21005, February 1978.* (AD #B027298L)

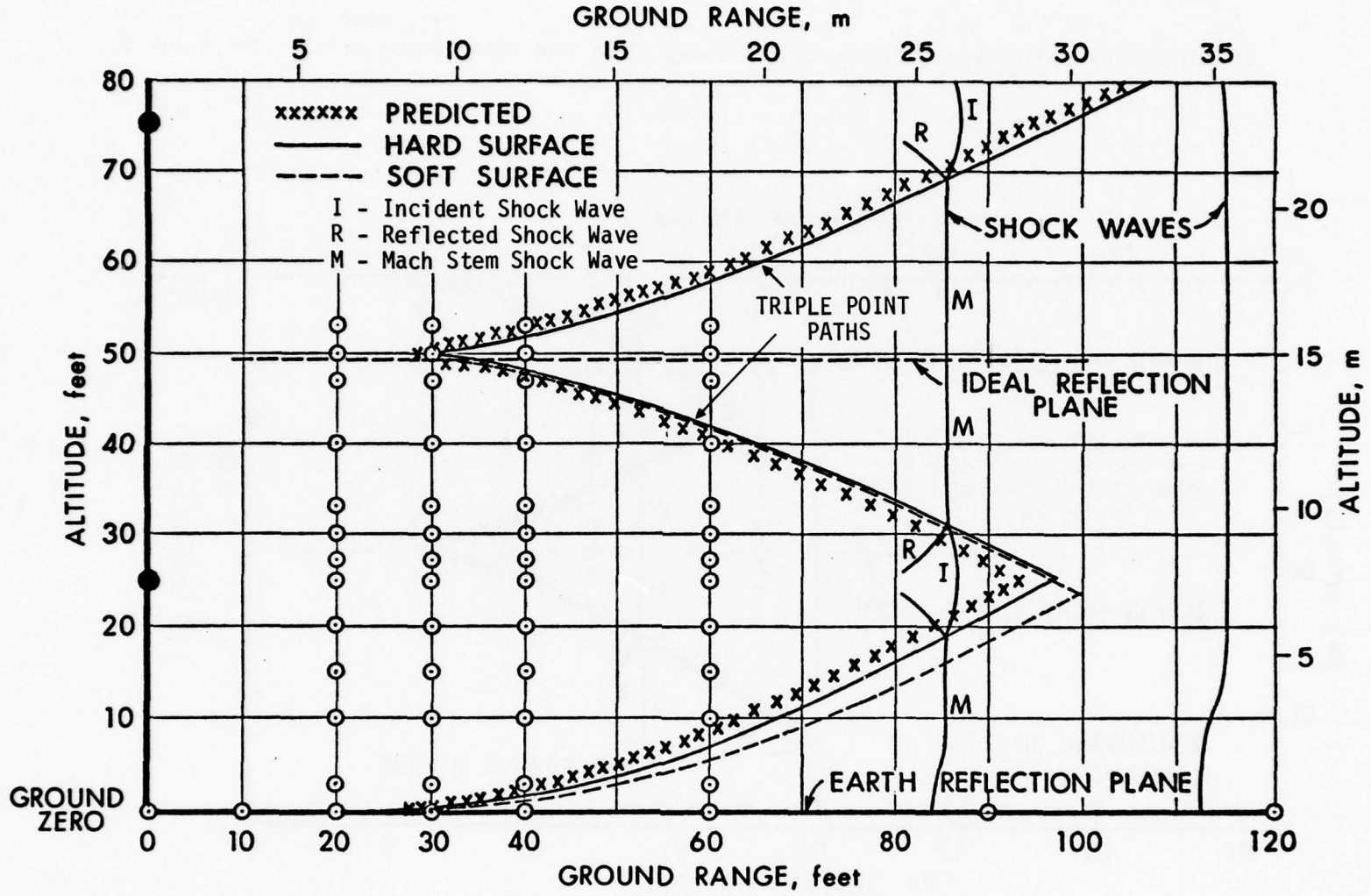

Figure 1.3. Triple-Point Paths and Shock Systems from Detonation Over Different Types of Surfaces

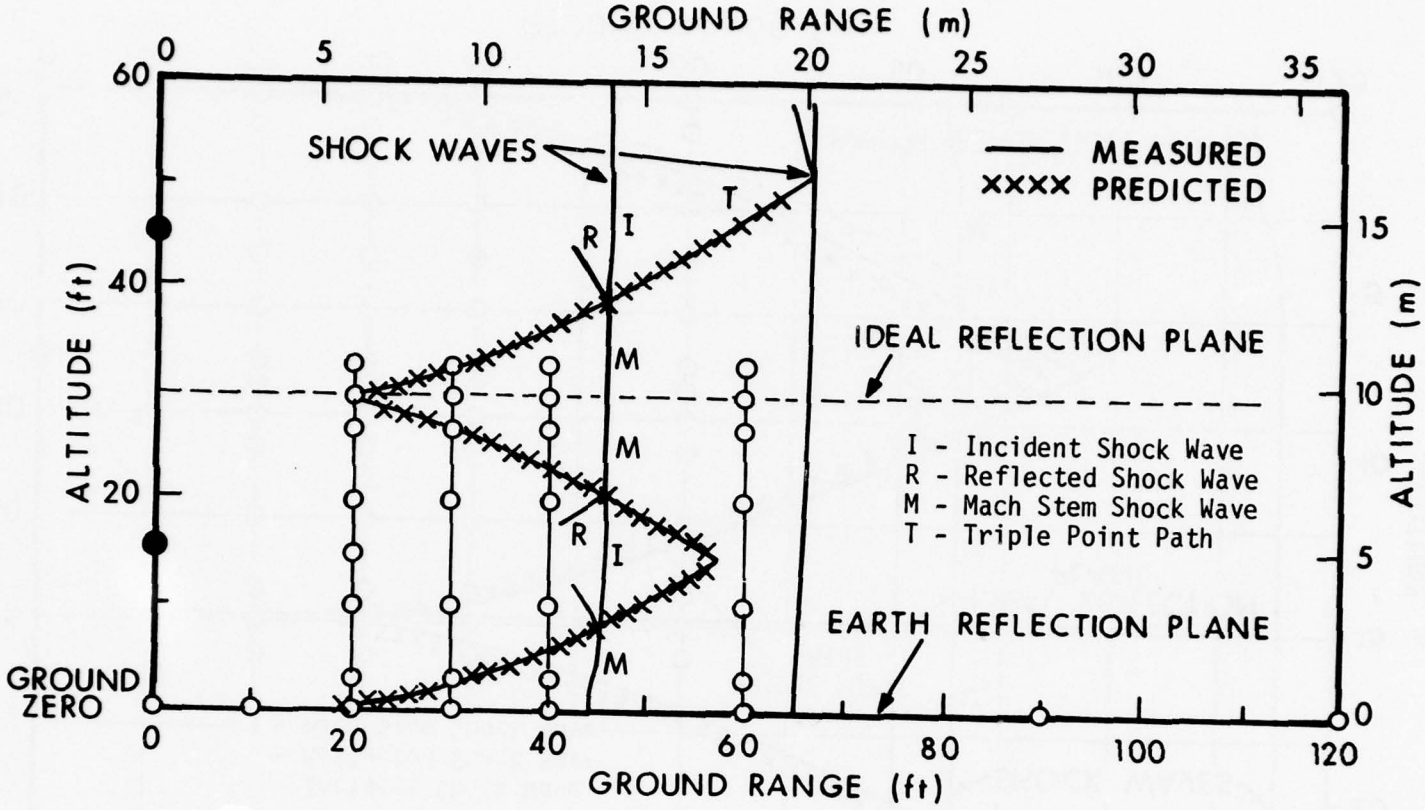

Figure 1.4. Triple-Point Paths and Shock Systems for the Simultaneously-Detonated Event of Phase III

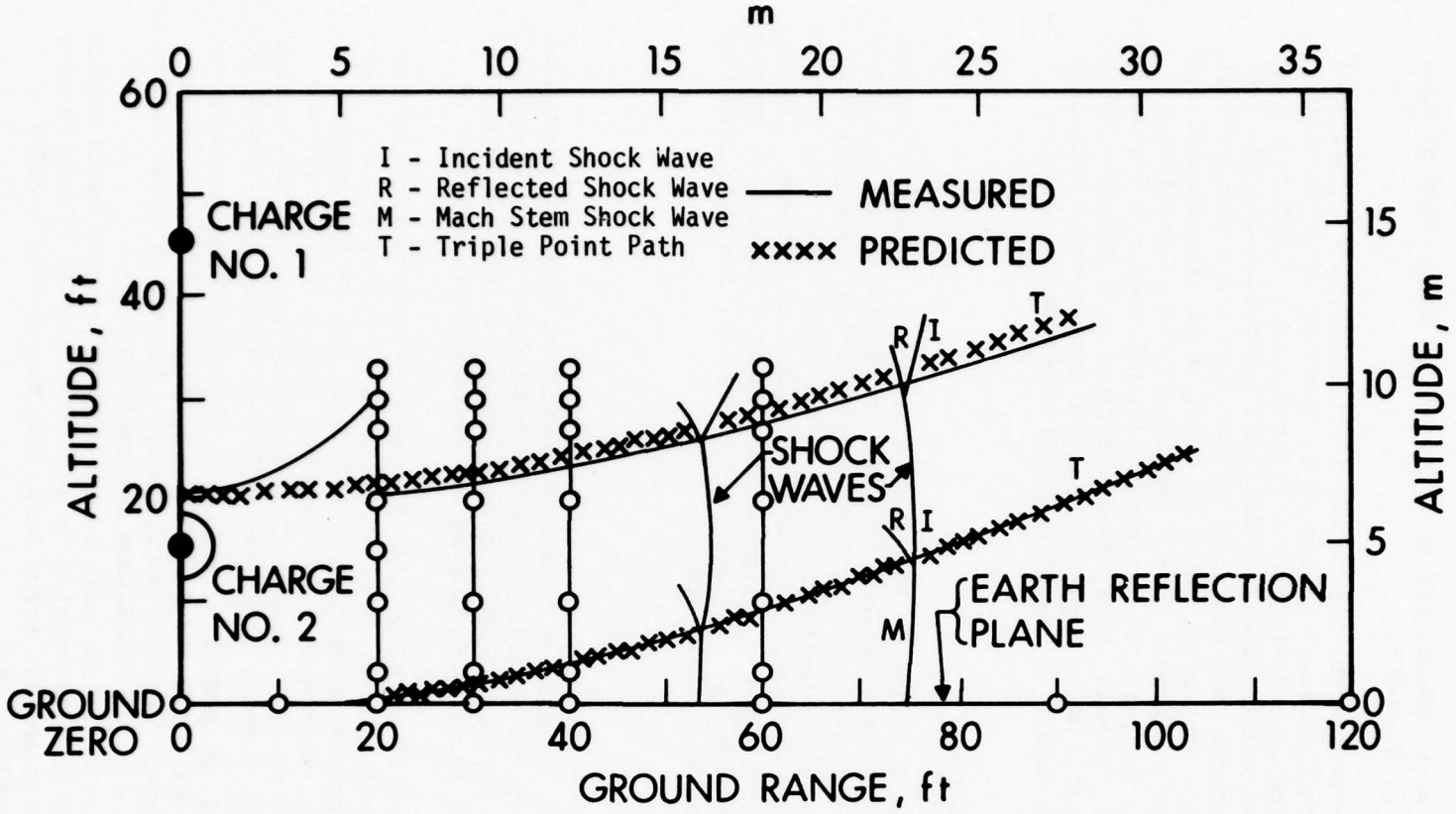

Figure 1.5. Triple-Point Paths and Shock Systems for the 5-Millisecond Delay Event

photographic data were reduced and analyzed by the University of Victoria (References 7, 8, and 9).

The Air Force Weapons Laboratory (AFWL) conducted theoretical calculations on configurations analogous to those of the test series with LAMB (Reference 1) and with HULL (Reference 10). LAMB is a low altitude multiburst model especially designed for predicting the free field blast environment from multiple nuclear explosions occurring in close time and space proximity. HULL is a full-blown two-dimensional hydrodynamic finite difference code. The comparison of experimental data with the calculational results provided input required for development of a multiple fireball interaction and cloud rise model to be incorporated into LAMB. Other modifications and improvements were made to both codes as a result of the DIPOLE WEST experimental input.

1.3 Report Objectives

The primary objective of the present report is to summarize and correlate all of the data obtained from the 16 events of the multiburst portion of the DIPOLE WEST high explosive test series. The series includes simultaneous and non-simultaneous charge detonations, as well as single charge events detonated to develop baseline conditions. Reports dealing with specific topics, listed as References 3 through 9, provide additional details about the fielding of the events, the data gathering techniques, and the analysis procedure.

---

7. *J. M. Dewey, D. F. Classen, and D. J. McMillin, "Photogrammetry of the Shock Front Trajectories on DIPOLE WEST Shots 8, 9, 10 and 11," UVIC PF 1-75, University of Victoria, British Columbia, Canada V8W 2Y2, July 1975 (also published by the Defense Nuclear Agency as DNA 3777F).*
8. *J. M. Dewey, D. J. McMillin, and D. Trill, "Photogrammetry of the Particle Trajectories on DIPOLE WEST Shots 8, 9, 10, and 11," University of Victoria, Victoria B.C., Canada, DNA 4326F, Defense Nuclear Agency, Washington, D.C. 20305. Volume I (Shot 10) was published in June 1977; Volume II (Shot 9) in October 1977; Volume III (Shot 8) in January 1978; and Volume IV (Shot 11) in March 1978.*
9. *J. M. Dewey, D. J. McMillin, and D. F. Classen, "Photogrammetry of Spherical Shocks Reflected from Real and Ideal Surfaces," University of Victoria, Victoria, B.C., Canada, Journal of Fluid Mechanics vol. 81, part 4, 1977 (Published in Great Britain).*
10. *HULL documentation exists only in the form of comment cards within the code. Further information is available from Air Force Weapons Laboratory, Kirtland Air Force Base, New Mexico 87117, ATTN: Mr. Charles Needham, DES.*

1.4 Sachs Scaling Factors

Because it is often of interest to compare airblast data from a series of high explosive events with data obtained using charges of different weights or from different locations, all airblast data are commonly scaled to data which would be obtained from a standard one-kilogram charge detonated at sea level. (In English units, the standard charge is one pound.) Commonly used Sachs scaling laws take into account differences in ambient pressure and temperature, as well as differences in charge weight.

In order to apply the scaling laws, a number of scaling factors are calculated appropriate to a given event. There is a scaling factor for each quantity of interest; that is, pressure, distance, time, and impulse. To obtain data corresponding to that which would be recorded if the event were a one-kilogram charge detonated at standard temperature (288°K) at sea level, the parameter concerned then needs only to be multiplied by the appropriate scaling factor. Scaling factors for all of the events in the multiburst series are given in Table 1.2. The expressions from which these scaling factors were calculated are given in Reference 11 (page 143). Environmental conditions prevailing at the time of detonation for each event, required as input to the scaling expressions, are given in Reference 3 (pages 78-80) and in Reference 4 (page 37).

Actual and scaled heights of burst (HOB) for all of the charges detonated in the series are given in Table 1.3. The first two columns present the actual and scaled distances from the lower or single charge of each shot to the real interaction plane. In all cases, this real interaction plane is the ground surface. The second group of two columns gives the actual and scaled distances from either charge to the interaction plane between them. This distance has been calculated as half of the charge separation distance in all cases, although in Phase III, because of the non-simultaneity of the detonations, the designation as distance to the interaction plane is not accurate. Finally, for Phases II and III, the average of the two previous distances, both actual and scaled, is given in the last two-column group. This distance is meaningful as an average effective height of burst only in the case of simultaneous detonations.

---

11. *R. E. Reisler, B. A. Pettit, and L. W. Kennedy, "Air Blast Data from Height-of-Burst Studies in Canada; Volume II, HOB 45.4 to 144.5 Feet," BRL Report No. 1990, USA Ballistic Research Laboratory, Aberdeen Proving Ground, Maryland 21005, May 1977.*

Table 1.2. Factors for Scaling Multiburst Data to a One-Kilogram Charge at Sea Level

Shot	S_p (Pressure)	S_d (Distance)	S_t (Time)	S_I (Impulse)
1	1.1009	0.1226	0.1240	0.1365
2	1.0846	0.1231	0.1231	0.1335
3	1.0800	0.1232	0.1244	0.1343
4	1.0784	0.1233	0.1280	0.1380
5	1.0831	0.1233	0.1257	0.1361
6	1.0889	0.1229	0.1273	0.1386
7	*	*	*	*
8	1.0872	0.1234	0.1244	0.1352
9	1.0900	0.1233	0.1230	0.1341
10	1.0738	0.1239	0.1193	0.1281
11	1.0738	0.1239	0.1163	0.1249
12	1.0792	0.2134	0.2101	0.2265
13	1.1089	0.2115	0.2123	0.2352
14	1.0927	0.2125	0.2180	0.2381
15	1.0915	0.2126	0.2144	0.2339
16	1.0826	0.2132	0.2065	0.2234

*Shot 7 produced a major blast wave anomaly along the gage line, so data from this event have not generally been used. Shot 8 was identical to Shot 7 in configuration.

Table 1.3. Actual and Scaled Values of Effective Heights-of-Burst

Shot	Distance from Lower Charge to Ground (m)		One-Half Charge Separation Distance (m)		Average HOB (m)	
	Actual	Scaled	Actual	Scaled	Actual	Scaled
1	37.86	4.642	*	*	**	**
2	38.31	4.716	15.34	1.888	**	**
3	38.99	4.804	7.58	0.934	**	**
4	40.14	4.949	25.23	3.111	**	**
5	39.15	4.827	15.27	1.883	**	**
6	40.75	5.008	*	*	**	**
8	7.45	0.919	7.60	0.938	7.53	0.929
9	4.62	0.570	4.62	0.570	4.62	0.570
10	4.55	0.564	4.66	0.577	4.61	0.571
11	7.31	0.906	7.64	0.947	7.48	0.927
12	4.49	0.958	4.59	0.980	4.54	0.969
13	4.53	0.958	4.58	0.969	4.56	0.964
14	4.53	0.963	*	*	**	**
15	4.53	0.963	4.59	0.976	4.56	0.970
16	4.59	0.979	4.62	0.985	4.61	0.982

* Single charge event.
** Average not meaningful in this configuration.

CHAPTER 2

HORIZONTALLY SEPARATED SIMULTANEOUS BURSTS

The first six events of the series, known as Phase I, were detonated in July of 1973. For this phase, the charges were separated horizontally and fired simultaneously. The charges were detonated at heights of 38 to 41 metres (124 to 134 feet) above ground, where it was felt that ground interactions would not be a factor in the analysis. Interest in this configuration stemmed from a desire to better understand shock-fireball interactions; specifically, (a) the effect of a shock wave on fireball deformation, (b) the effect of a shock wave on fireball rise characteristics, and (c) the effect of neighboring fireball flow fields on fireball rise and expansion. It was expected that information obtained from ground and airborne photography would serve to verify details of shock-fireball interactions observed in results of hydrodynamic computer code calculations.

The series was begun using 490-kilogram (1080-pound) pentolite charges. Delays in delivery of the pentolite, however, required that most of the series be carried out with 493-kilogram (1086-pound) TNT charges. Shots were fired with the distance between the two charges equal to approximately one, two, and three fireball radii (fireball radius is approximately 15 metres or 50 feet). In addition, two single-charge shots, one each of pentolite and TNT, were fired. Details of the fielding of these events, plus reproductions of the overpressure records obtained, are given in Reference 3.

2.1 Fireball Motion and Cloud Rise

In the study of nuclear and high explosive effects, fireball expansion and subsequent torus formation are important phenomena. These phenomena cannot be studied without considering the effects of blast waves, which interact with the fireballs in the early stages. A significant portion of the LAMB model deals with fireball behavior and shock-fireball interactions. A major purpose of performing the horizontally separated Phase I events was to obtain, in addition to air blast data, information on fireball behavior and cloud rise for correlation with and input to LAMB.

Unfortunately, the photographic data obtained on cloud rise and torus formation were not as useful as had been anticipated. The detonations produced so little in the way of smoke and detonation products that the clouds remained visible to the cameras for only a few seconds. In addition, due to either less than ideal symmetry of the detonations or higher than anticipated upper level wind velocities, good torus formation in the clouds was not observed.

Some analysis, however, of the ground level photographic data was undertaken. Figure 2.1 shows the top and bottom extent of the smoke cloud as determined for the single-charge TNT event, Shot 6. Shot 6 was chosen for comparison with calculated results because the length of time over which the cloud remained visible, six seconds, was the longest of any of the shots. The hydrodynamic code predictions in the figure are from a HULL calculation for which the height of burst was 41.1 metres (135 feet). The actual height of burst for Shot 6 was 40.8 metres (133.7 feet). The code predictions of cloud vertical diameter and cloud rise versus time compare favorably with the experimental results, particularly in the interval between two and six seconds after detonation.

In the case of simultaneous, horizontally separated detonations, the vertical plane perpendicular to the line joining the two charge centers serves as an ideal shock-reflection plane. Hence, reflected shock waves distort the two fireballs into twin tori lying in vertical planes parallel to the shock-reflection plane. As buoyant forces begin to take over, the tori rotate in opposite directions until they lie in a single horizontal plane. (The lower portions of the tori move outward and upward to accomplish this rotation.) As the twin tori expand and drift upward, they may, if they are sufficiently close together, eventually coalesce to form a single torus.

The DIPOLE WEST photographic data could not be used either to confirm or deny this double torus phenomenology, which has been developed primarily from calculational results. Some information about comparative rise rates of single- and double-burst clouds was obtained, however, and this is illustrated in Figure 2.2. The single-burst Shot 6 data are compared with those from Shot 3, a double-burst event. The horizontal charge separation distance for Shot 3 was 15.2 metres (49.7 feet). Again, Shot 3 was chosen for the comparison because cloud rise data were available over a longer period of time for this event than for any of the other horizontally separated double-burst events. The average height of burst for Shot 3 was 39.0 metres (128.0 feet), as compared to 40.8 metres (133.7 feet) for Shot 6.

As illustrated in the figure, the rise rate for the double-burst cloud was about 6.1 metres/second (20 feet/second), whereas that for the single-burst cloud was 10.1 metres/second (33 feet/second). The slower rise of the double-burst cloud is consistent with expectations because of interaction of the flow fields. Downward flowing air from one cloud is opposed by upward flowing air from the neighboring cloud, and hence the net buoyant force on the system is decreased.

2.2 Shock Interactions and Mach Stem Behavior

For horizontally separated charges, a Mach stem forms at the vertical ideal reflection plane midway between the charges, as illustrated in Figure 1.1. This Mach stem extends its length as the shock

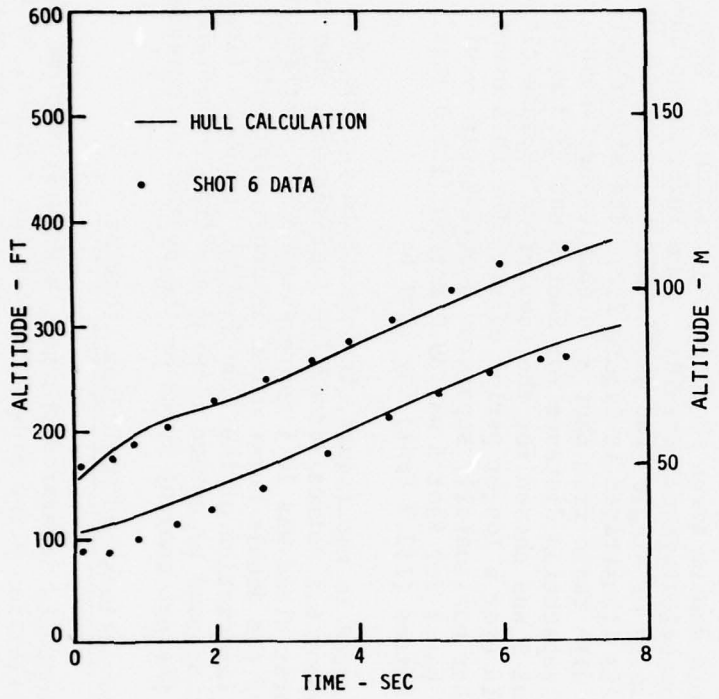

Figure 2.1. Top and Bottom Extent of Smoke Cloud; Single-Charge TNT Event

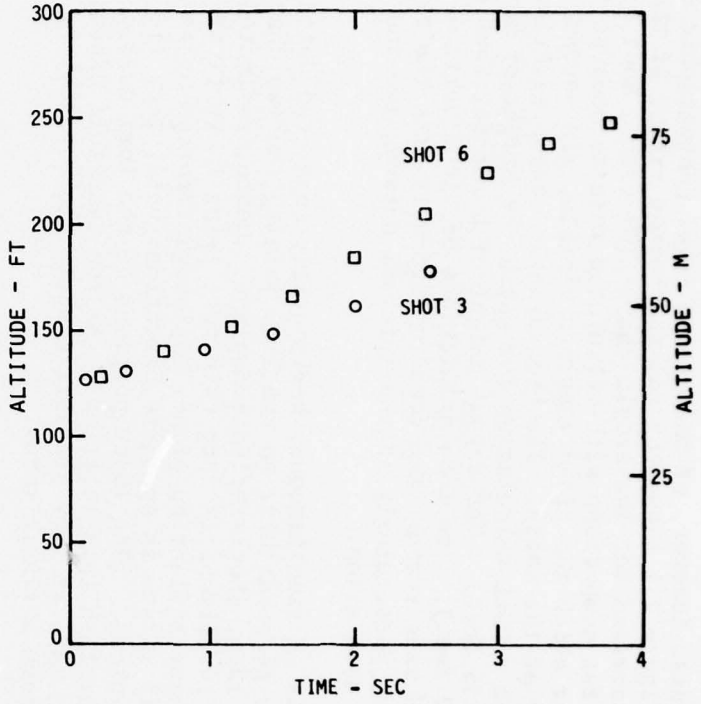

Figure 2.2. Comparative Rise Rates of Single-Burst (Shot 6) and Double-Burst (Shot 3) Smoke Clouds

system moves toward the ground; the rate of growth depends on the charge separation distance and on the charge size. Two overpressure records taken at the same location in two different events illustrate the dependence of Mach stem growth on charge separation. The gage location is at ground level, 7.6 metres (25 feet) from ground zero, in the plane containing the charges. Ground zero is the point on the ground midway between charges.

The records in Figure 2.3 are from Shot 2, for which the charge separation distance was 30.5 metres (100 feet). In these records the incident and reflected shock peaks are clearly separated in time, indicating that the transducer was located in the regular reflection region; that is, the length of the Mach stem on each side of the reflecting plane as the system reached the ground was less than 7.6 metres (25 feet). In Figure 2.4, the records show a single shock, indicating that the transducer was located within the Mach reflection region. The records of Figure 2.4 are from Shot 3, for which the charge separation distance was 15.2 metres (50 feet).

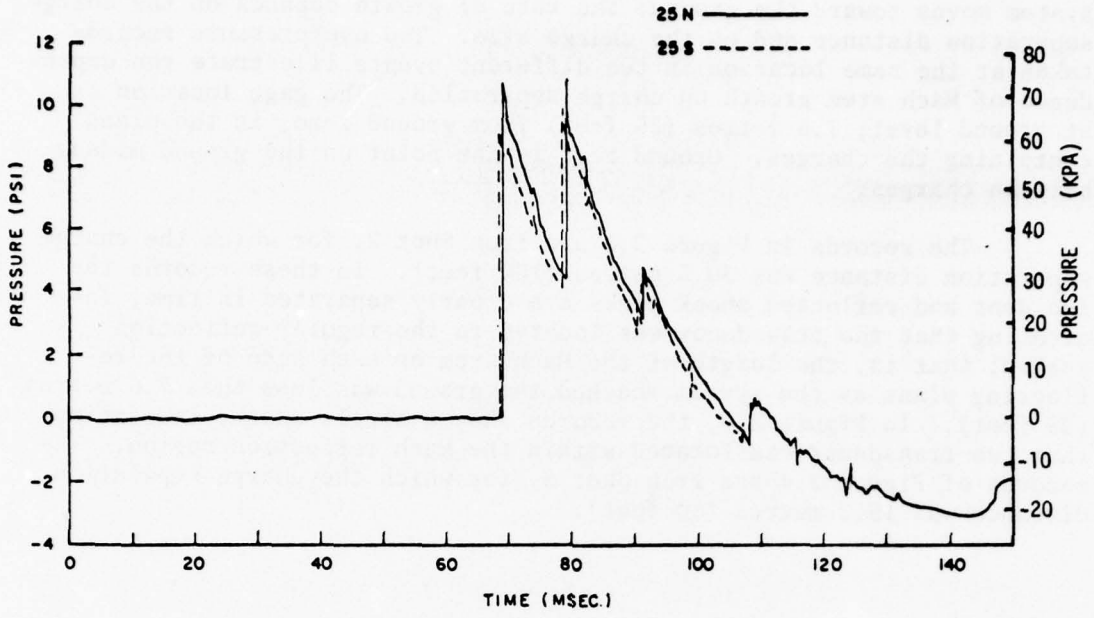

Figure 2.3. Pressure Records from the Regular Reflection Region; Charge Separation Distance, 30.5 Metres (100 Feet)

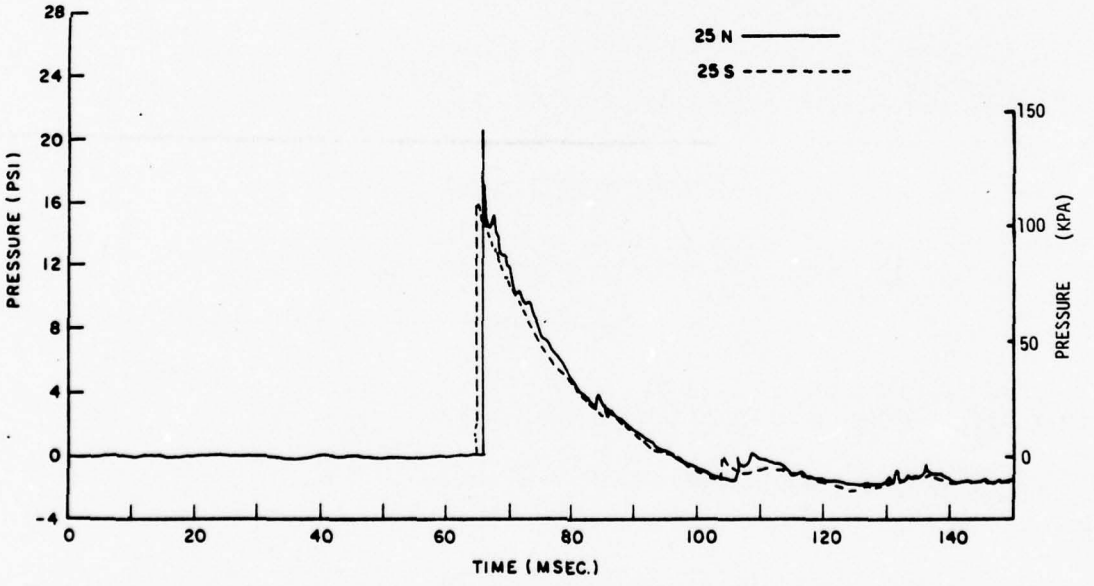

Figure 2.4. Pressure Records from the Mach Reflection Region; Charge Separation Distance, 15.2 Metres (50 Feet)

CHAPTER 3

VERTICALLY SEPARATED SIMULTANEOUS BURSTS

Phase II of DIPOLE WEST is the series of events in which two charges, in a configuration with identical charges suspended one above the other, were fired simultaneously. Phase II consists of five events, Shots 7 through 11, which were fired in September, October and November of 1973. Details of the fielding and firing of these events, plus the records obtained from the overpressure and total head pressure transducer array, are contained in Reference 3. Analysis of the photographic data obtained is given in Reference 7 (refractive image analysis) and in Reference 8 (particle trajectory analysis). Although data were obtained on Shot 7, a significant blast anomaly propagating directly along the gage line was observed on this event, and so the data have generally been discounted. The configuration of Shot 8 was the same as that of Shot 7.

This series of events was designed specifically to examine the differences between shock wave interaction with an ideal reflecting plane and with a real surface. Hydrodynamic code calculations used to model detonations of this kind generally assume that the surface of the ground is a perfectly reflecting, frictionless boundary. In reality, of course, some energy from the shock system is transferred into the ground. Discrepancies between calculated and experimental results (especially in horizontal dynamic pressures) near the ground surface indicate that the calculational modeling is indeed inadequate and needs to be improved.

Configuration of this series was as shown in Figure 3.1. The lower charge is a distance X above the ground and the upper charge is 3X above ground. If the charges are detonated simultaneously, the interaction of the shock systems at the plane halfway between the charges (at a distance 2X above ground) will be like that at an ideally reflecting, frictionless surface. Measurements made near this surface may then be compared with similar measurements made near the actual ground surface. For Shots 7, 8 and 11, the distance X was approximately 7.62 metres (25 feet); for Shots 9 and 10 it was approximately 4.57 metres (15 feet). Actual detonated charge heights, with corresponding distances to the ideal reflecting planes, are given in Tables 1.1 and 1.3.

Two different conditions were used for the real ground surface in an attempt to determine whether surface conditions had a discernible effect on the shock-ground interactions. For Shots 7, 8 and 9, the natural, hard-packed, smooth prairie surface was used. In Shots 10 and 11, an attempt was made to create a rough, soft, more energy-absorbent surface by concentric furrowing of the test bed area. Dimension of the furrows was approximately 14 inches.

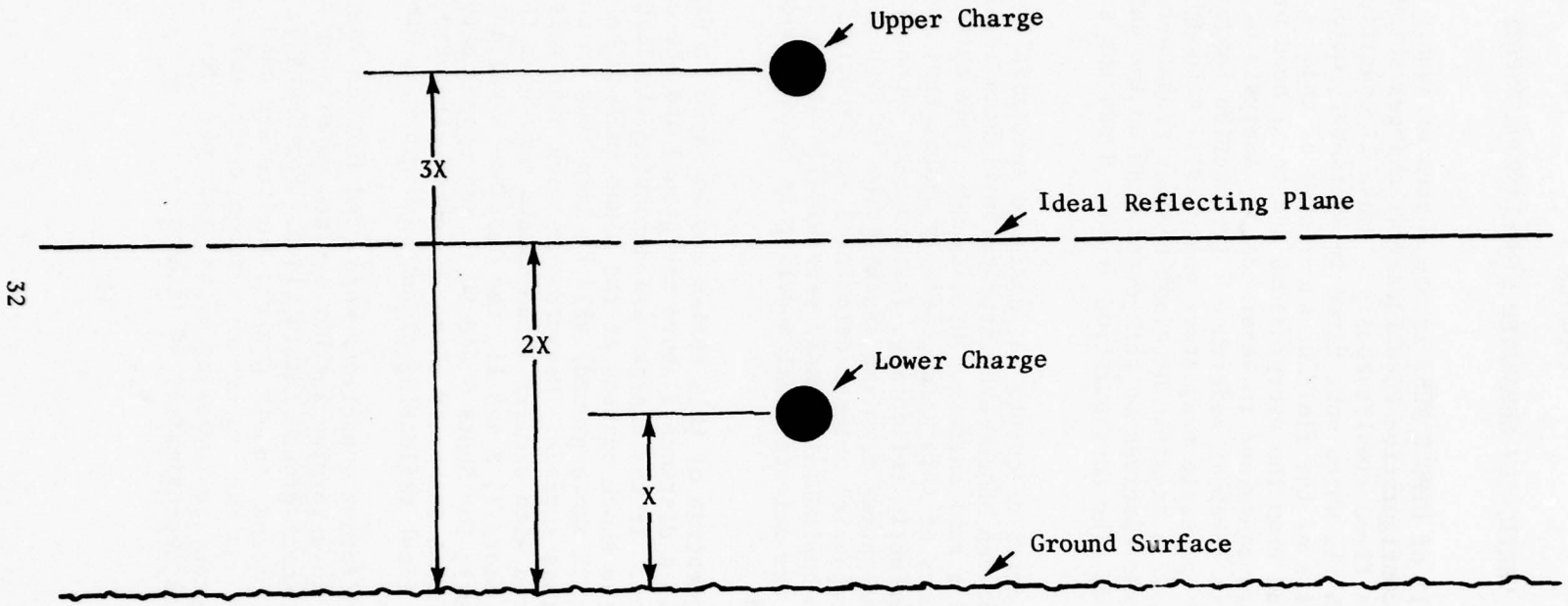

Figure 3.1. Position of Reflecting Planes for Vertically-Separated, Simultaneously-Detonated Charges

3.1 Fireball Motion and Cloud Rise

In the case where two equal simultaneous bursts are separated vertically by a distance of several fireball radii, each fireball behaves initially like that from a single burst. Each shock arrives at the other fireball at approximately the same time. The lower fireball, rising at the time of shock incidence because of buoyant forces, is slowed by the shock. If the shock strength is sufficient to reduce fireball acceleration to zero, then the lower fireball will form a torus.

The rise of the upper fireball is boosted by the incident shock wave, and hence it tends to rise more rapidly. The increased rise rate generates increased drag forces, and these forces may cause the upper fireball also to torus. Following torus formation, both fireballs and the clouds formed from them drift upward, controlled by the torus flow fields.

When the vertically separated charges are one fireball radius or less apart, as in the DIPOLE WEST events, the phenomenology of fireball and cloud behavior is less well understood. The fireballs are observed to merge at an early time, and hence to react essentially like a single-burst system. Unfortunately, as with the horizontally separated events, the clouds from the vertically separated double-burst events remained visible to the cameras for only a few seconds, and good torus formation was not observed.

3.2 Shock Systems and Triple-Point Behavior

When a charge is detonated near a surface, such as the surface of the ground, a reflected shock wave will form as the incident shock strikes the surface. If the incident and reflected shocks are strong enough, the point at which these shock waves come together moves away from the surface. A third shock wave, called the Mach stem, then forms in the region between the point and the surface. The point at which the three shocks meet is called the triple point. The triple point forms at the reflection plane and moves away from it along a curved trajectory as the shock system moves outward. Triple-point paths developed from the detonations at 7.6 and 22.8 metres (25 and 75 feet) were shown in Figure 1.3. Those from the detonations at 4.6 and 13.7 metres (15 and 45 feet) are illustrated in Figure 3.2. The actual shock-front shapes, as measured from high-speed photographic data on Shot 10, are given in Figure 3.3. This latter figure has been scaled to show the data as if they had been obtained from a one-kilogram charge at 15°C in dry air at sea level, as explained in Chapter 1 and in more detail in Reference 9.

The behavior of the Mach stem shock wave, and particularly any differences in this behavior which might be attributed to differences in the texture of the surface, was of particular interest for the

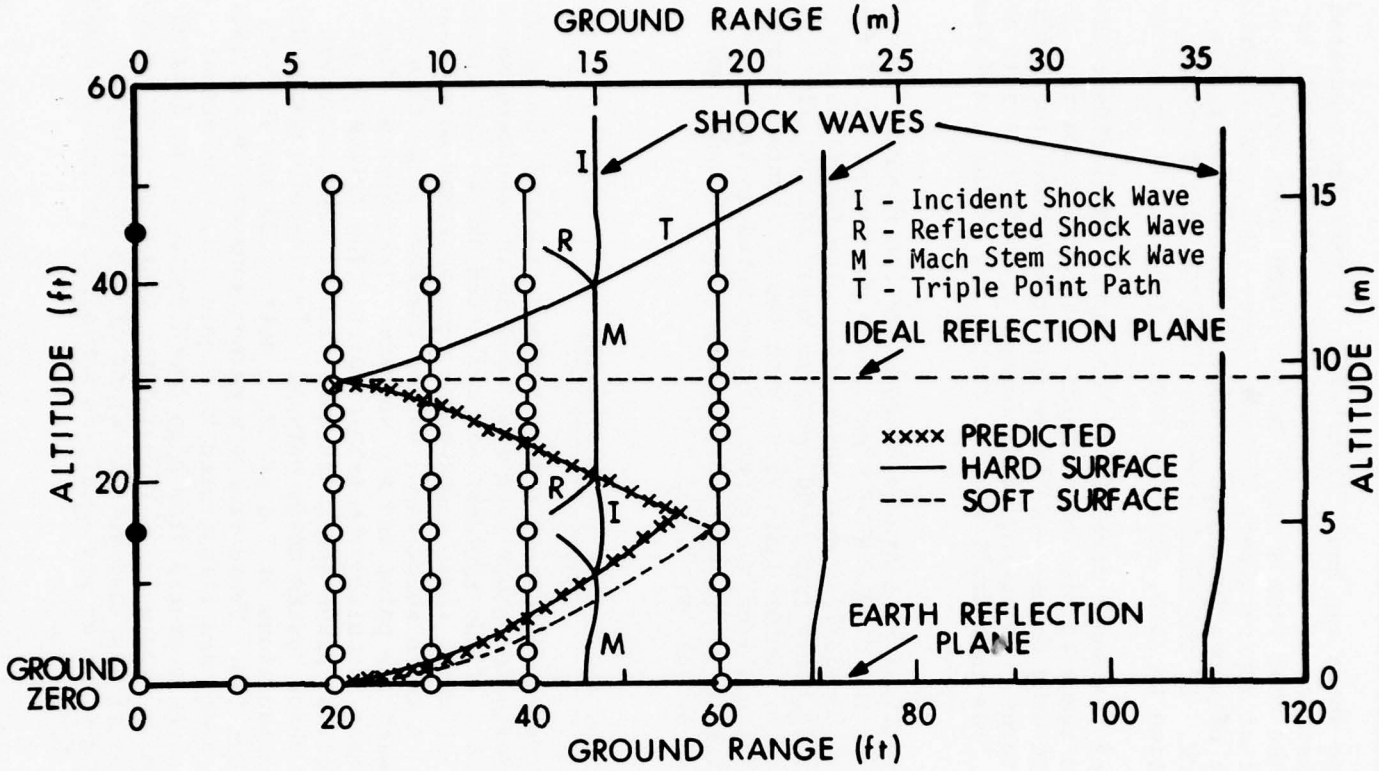

Figure 3.2. Triple-Point Paths and Shock Systems for the More Compact Configuration of Phase II

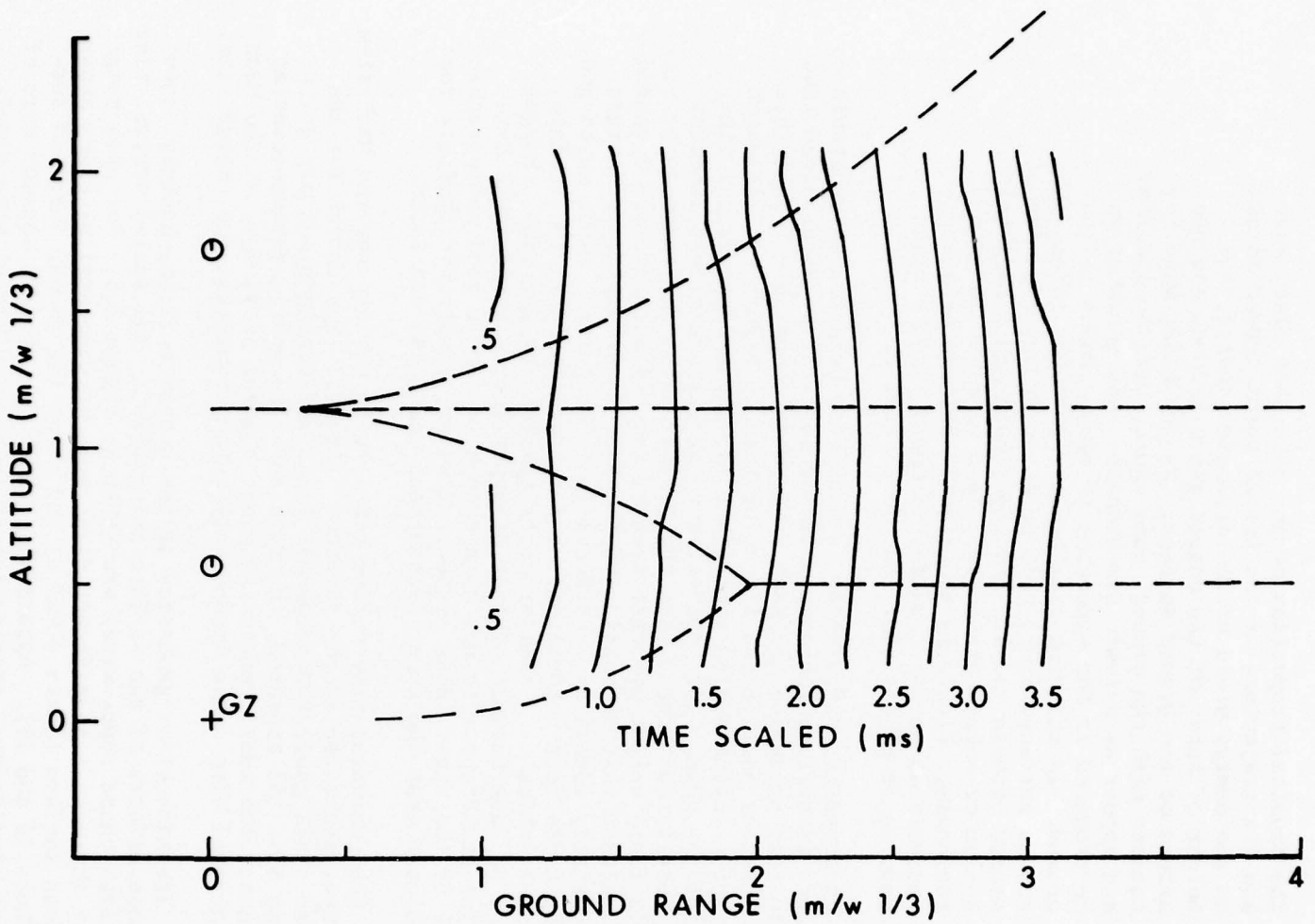

Figure 3.3. Scaled Shock-Front Shapes from High-Speed Photographic Data; Shot 10

present study. Quoting from Reference 9:

> *The physical properties of the Mach-stem blast wave and the trajectory of the triple point depend mainly on the energy yield of the explosive charge, the height of burst of the charge above ground, and the nature of the ground surface. As the blast wave interacts with the ground, some energy will be absorbed and appear as seismic disturbances, and a crater may be produced if the explosion is close enough to the ground. As the Mach-stem blast wave moves across the ground surface, there will be a continuous transfer of energy between the air and the ground and a redistribution of energy within the blast wave due to ground roughness. Little is known qualitatively or quantitatively about the transfer of energy from a blast wave as it passes over the ground surface.*

In assessing differences in Mach-stem behavior attributable to differences in surface roughness, it should first be ascertained that the explosions producing the Mach stems were comparable. That this was the case for Shots 8 and 11 can be seen in Figure 3.4, in which scaled radius versus scaled time (that is, shock-wave arrival time) curves for the primary or incident wave shocks are almost identical. Similar results were found when the primary shock curves from the 4.6-metre (15-foot) height-of-burst events, Shots 9 and 10, were compared. It is concluded that detonation of the four lower explosive charges was essentially identical, and hence that the primary shock waves generated by these four detonations, before reflection at the surface, were also identical. A similar determination for the upper charges could not be made because of lack of upper-level photographic data. The canvas backdrops were not high enough to permit good photographic coverage of the upper shock system. However, electronic pressure records indicate that the upper detonations were also consistent.

Scaled radius-time curves can also be plotted for the Mach-stem shock waves generated at the surfaces. Arrival-time curves for the Mach-stem shock generated below the ideal reflecting plane are given in Figure 3.5. As expected, the data for like configurations overlap each other. The ideal reflecting plane absorbs no energy, so the Mach stem generated here would depend only on configuration and charge size.

The Mach stems generated at the ground surface, however, show noticeable effects of the surface interaction. The scaled arrival-time curves from these shock waves are shown in Figure 3.6. For each height of burst there is a significant difference between arrival times above the smooth surface (Shots 8 and 9) and above the rough, furrowed surface (Shots 10 and 11). Apparently, the rough surface absorbs more of the shock-wave energy, causing the shock wave to travel more slowly. The measurements from which these curves were plotted were taken at

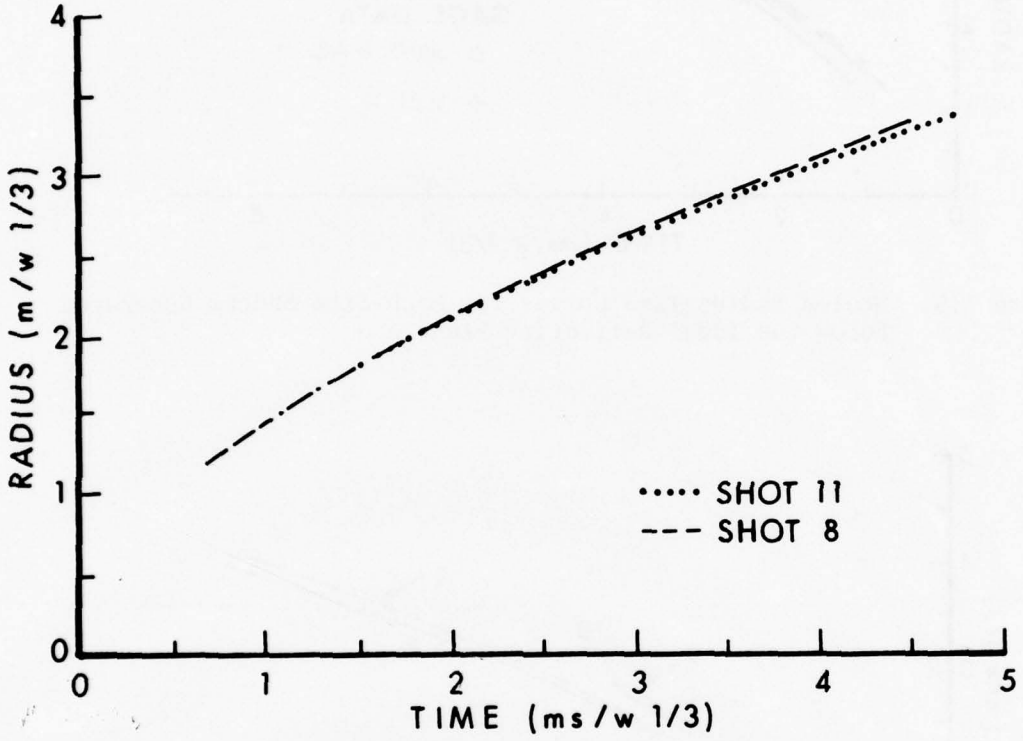

Figure 3.4. Scaled Radius-Time Curves for the Incident Wave Shocks; Shots 8 and 11

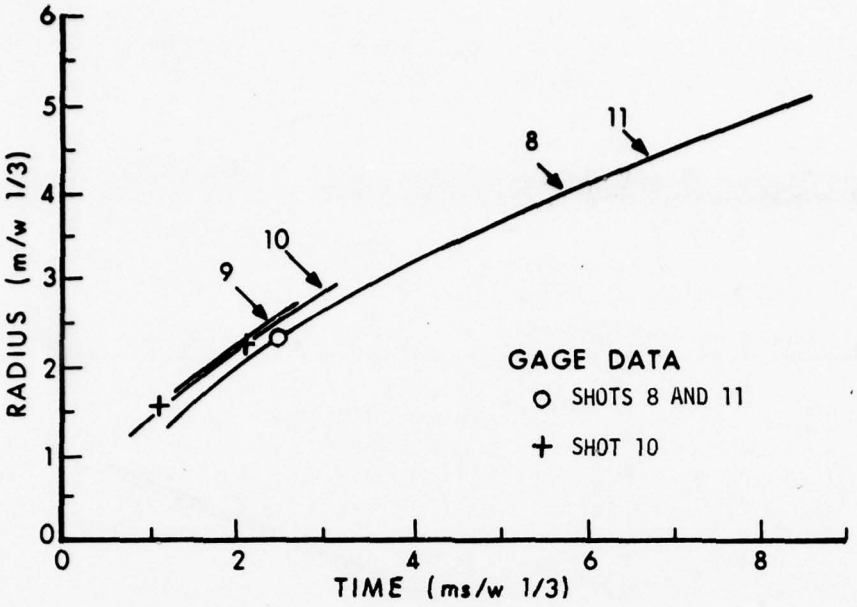

Figure 3.5. Scaled Radius-Time Curves for Mach-Stem Shocks Generated Below the Ideal Reflecting Plane

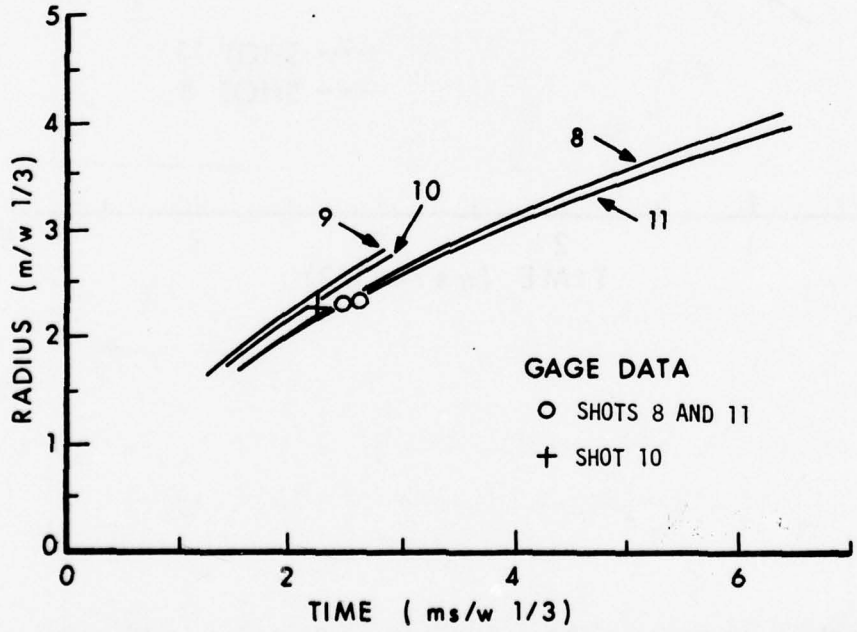

Figure 3.6. Scaled Radius-Time Curves for Mach-Stem Shocks Generated at the Real Surface

approximately 0.5 metres (20 inches) above the ground. The ideal-plane measurements were taken at approximately 0.2 metres (8 inches) below the reflecting plane.

The loci of the triple points, or triple-point paths, observed on Shots 8 and 11 are plotted in Figure 3.7. The paths below the ideal reflecting plane were essentially identical in the two experiments. The ordinate axis for the ideal-surface curve in this figure is actually scaled distance measured downward from the ideal reflecting surface. As can be seen, the effect of the ground surface is to lower the triple-point trajectories. The rough, furrowed surface produces the more marked deviation from the ideal-surface curve. This modification of triple-point behavior is also noticeable in Figures 1.3 and 3.2.

3.3 Single- versus Double-Burst Overpressures

When two charges in close proximity are detonated simultaneously, overpressure records measured near the charge array will show separate peaks, arriving at different times, for the shock pulses from the two charges. The relative magnitude and separation in time of the peaks depends on the separation distance of the charges. As the measurement point is moved farther away from the charges, however, a radial distance is reached where details of the charge array are no longer discernible. The shock systems have coalesced, and pressure records are the same as would be obtained from a single burst of double the individual charge weight.

This phenomenon can be observed in Figures 3.8 and 3.9, in which peak overpressures measured at ground level are plotted as a function of radial distance from ground zero. Single-burst data from an earlier series (Reference 12), scaled to appropriate charge weights, was used to develop the solid line base. As can be seen, at close-in ranges the data fall on the 490-kilogram (1080-pound) curve, equivalent to what would be expected from a single charge. Farther out, a transfer to the 980-kilogram (2160-pound) double-weight curve occurs. The transition range depends on charge separation. For the 15.2-metre (50-foot) separation events, Shots 8 and 11, the transition occurs at about 30 metres (98 feet). For Shots 9 and 10, however, in which the charge separation was 9.1 metres (30 feet), the transition to conditions like that of a single, double-weight charge occurs at a range of 20 metres (65 feet).

---

12. *R. E. Reisler, B. A. Pettit, and L. W. Kennedy, "Air Blast Data from Height-of-Burst Studies in Canada; Volume I, HOB 5.4 to 71.9 Feet," BRL Report No. 1950, USA Ballistic Research Laboratory, Aberdeen Proving Ground, Maryland 21005, December 1976.* (AD #B016344L)

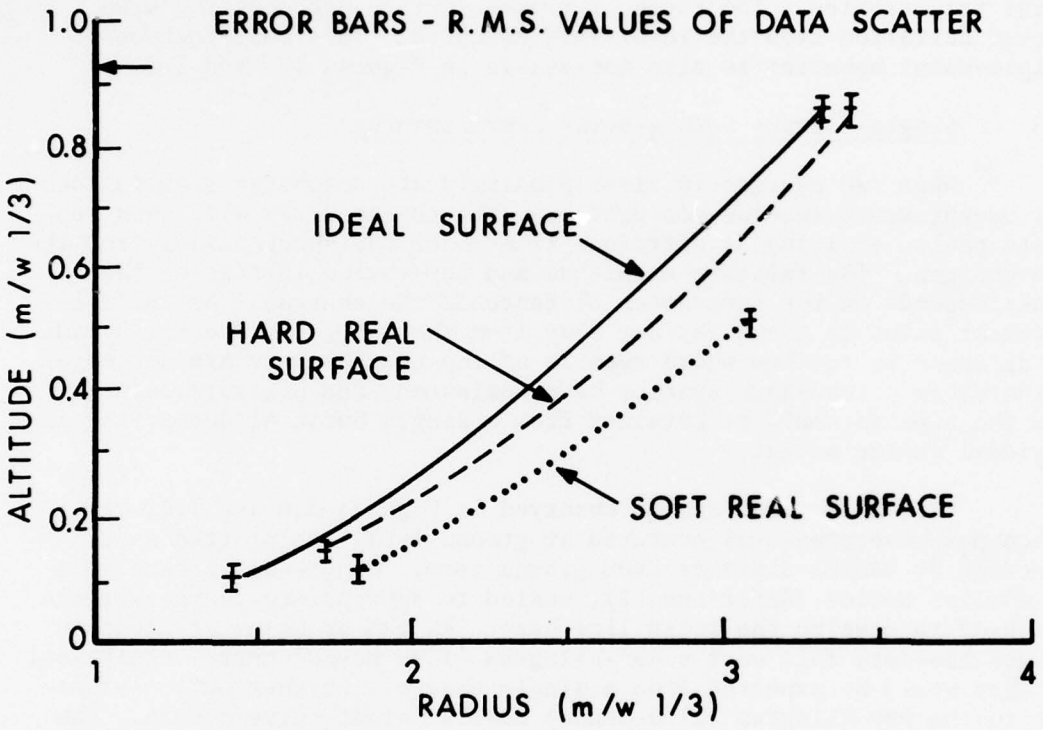

Figure 3.7. Scaled Triple-Point Paths for Real and Ideal Surfaces; Shots 8 and 11

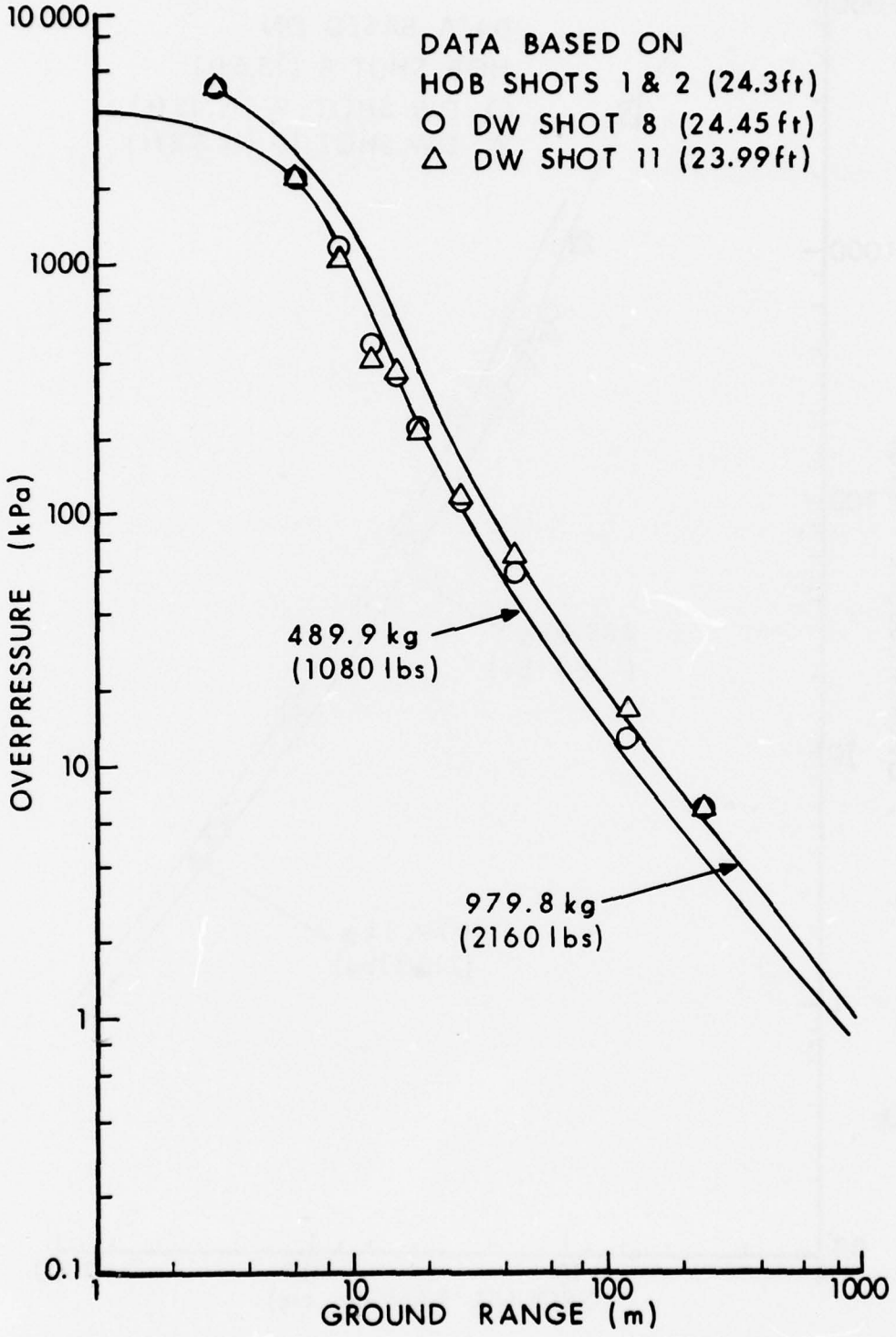

Figure 3.8. Peak Overpressures at Ground Level, Plotted to Show Transition from Single- to Double-Weight Charge Curve; Shots 8 and 11

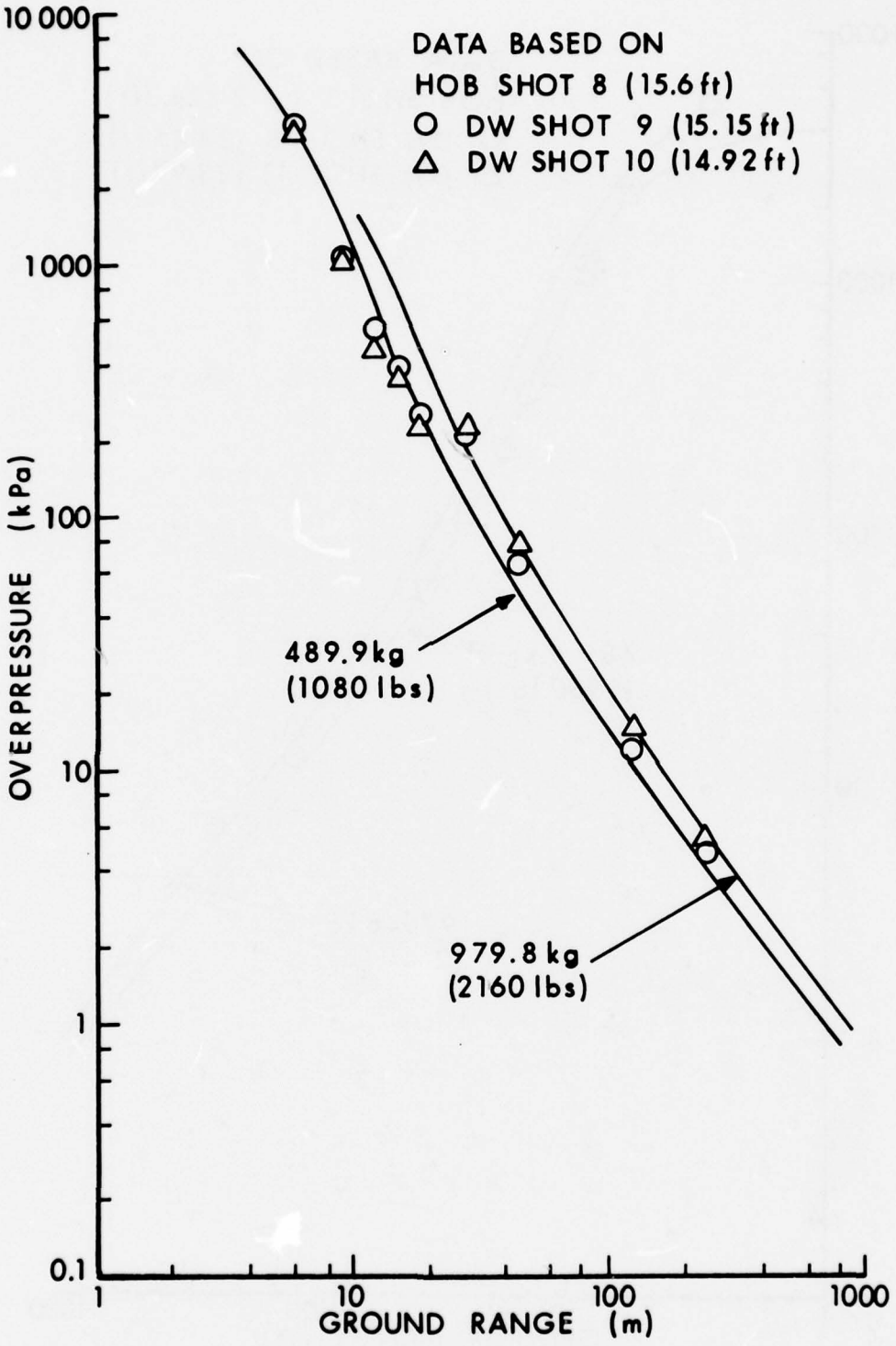

Figure 3.9. Peak Overpressures at Ground Level, Plotted to Show Transition from Single- to Double-Weight Charge Curve; Shots 9 and 10

The change from single- to double-weight charge phenomenology does not appear in the maximum impulse versus range curves, as shown in Figures 3.10 and 3.11. The impulse apparently follows the double-weight curve regardless of range. This is because overpressure impulse is an integrated effect, contributed to by all portions of the incident pressure waveform. Differences in time of arrival between pressure pulses from different sources strongly influence the superimposed overpressure, but have little effect on the total impulse, or momentum, carried by the pressure system.

3.4 Parametric Studies of Overpressure Waveforms

An interesting comparison of the effects of real and ideal reflecting planes can be made by studying the overpressure records obtained from gages positioned along these planes. In Figures 3.12 and 3.13, gage records at ground level from Shots 8 and 11 are compared with those at 15.2 metres (50 feet), which is the height of the ideal reflecting plane. At the close-in stations, the records are quite similar, except for the double-peaked nature of those from Station 20.50. The double peaks probably arise because the gage was not located exactly on the reflecting plane. For close-in stations, where the shock system passes before the Mach stem has begun to develop, the position of the plane is critically dependent on charge placement. As can be seen by referring to Table 1.1, the charge positions were not exact, and hence it was to be expected that the ideal reflecting plane would not develop at precisely the preset gage elevations. Once the Mach stem has begun to form, as at the 9.1-metre (30-foot) range and beyond, gage elevation is not so critical.

The point to be observed from this series of comparisons is that, while the real and ideal plane records are quite similar close-in, they become more divergent as ground range increases. At the 12.2- and 18.3-metre (40- and 60-foot) ranges, as shown in Figure 3.13, the real-plane ground-level overpressures fall below those from the ideal plane in every case. The effect is most noticeable in the records from Shot 11, for which the ground surface was furrowed. It is apparent that, as the shock system advances outward from the source, some of the energy in the system is being absorbed by the soft, rough surface.

A similar series of comparisons from Shots 9 and 10 is shown in Figures 3.14 and 3.15. The quality of the records obscures the effect somewhat in these cases. However, it is still apparent that the overpressures deteriorate more rapidly at the energy-absorbing real surface than they do at the ideal reflecting plane.

Direct comparisons between the two types of real reflecting surfaces are given in Figures 3.16 through 3.19, in which both overpressure and total head pressure records taken at 0.91 metres above the surface are compared. In every case in which the records are clean enough that a difference can be observed, the pressures from the

(Text continued on page 54.)

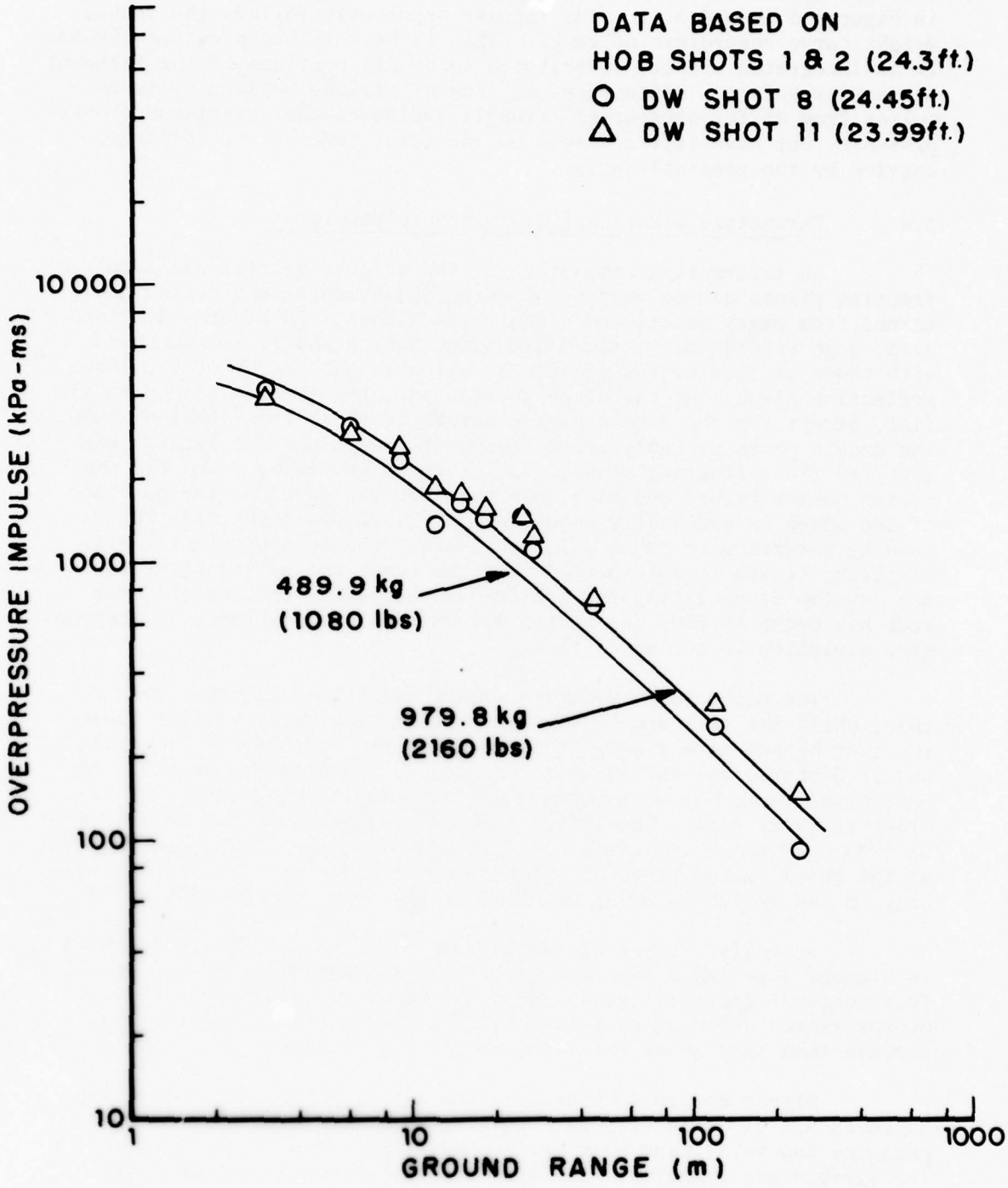

Figure 3.10. Maximum Impulse at Ground Level versus Range; Shots 8 and 11

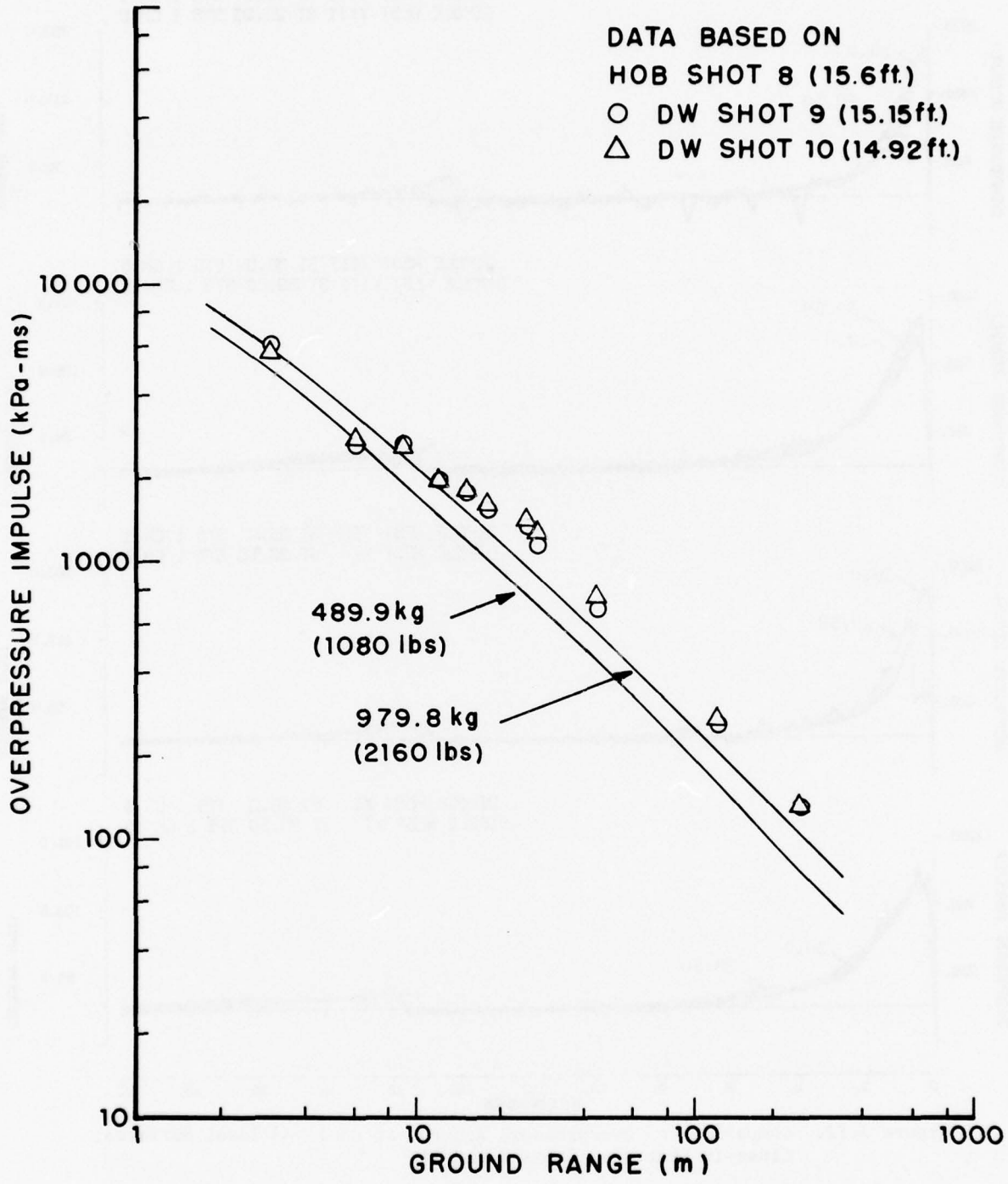

Figure 3.11. Maximum Impulse at Ground Level versus Range; Shots 9 and 10

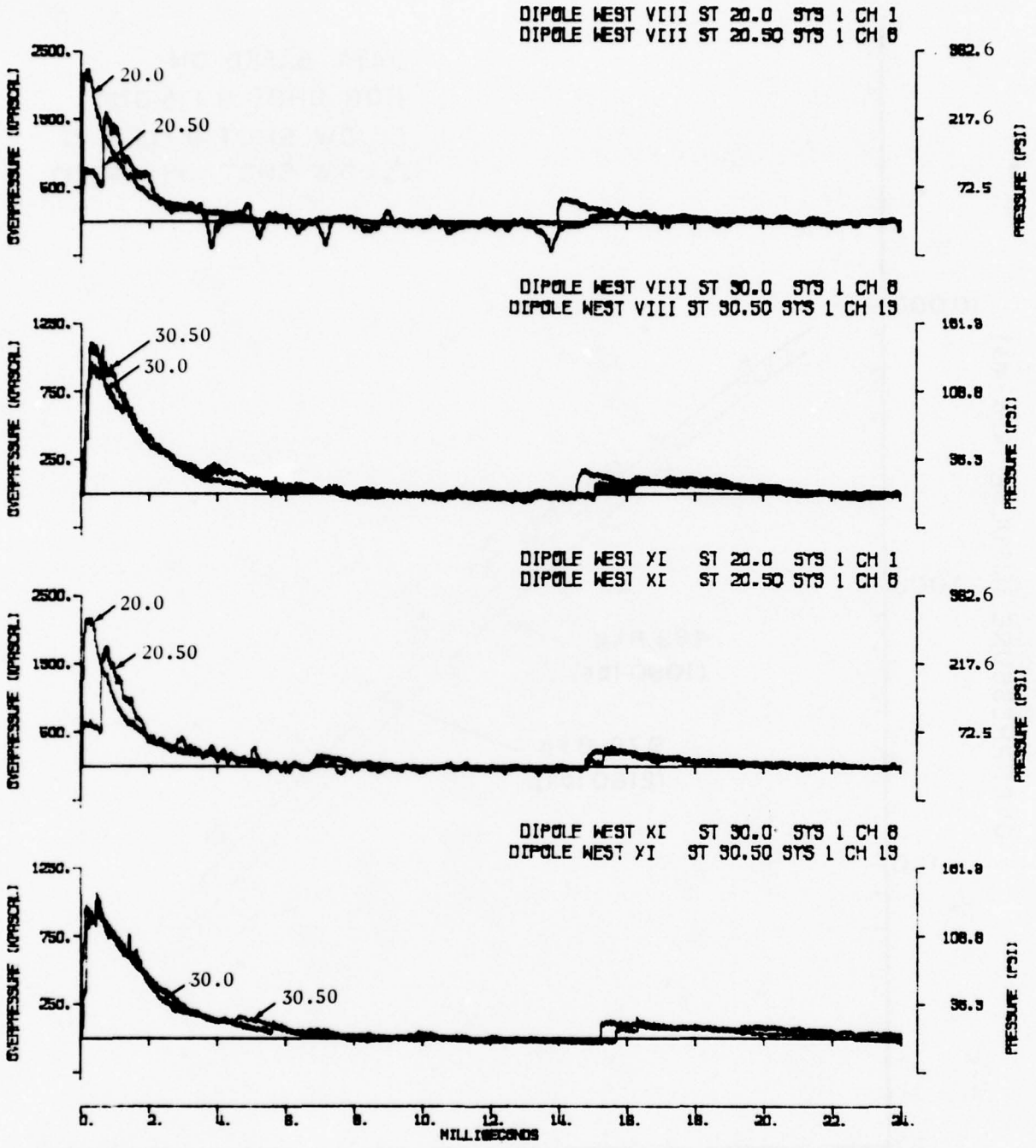

Figure 3.12. Comparison of Overpressure Records at Real and Ideal Surfaces; Close-In Stations, Shots 8 and 11

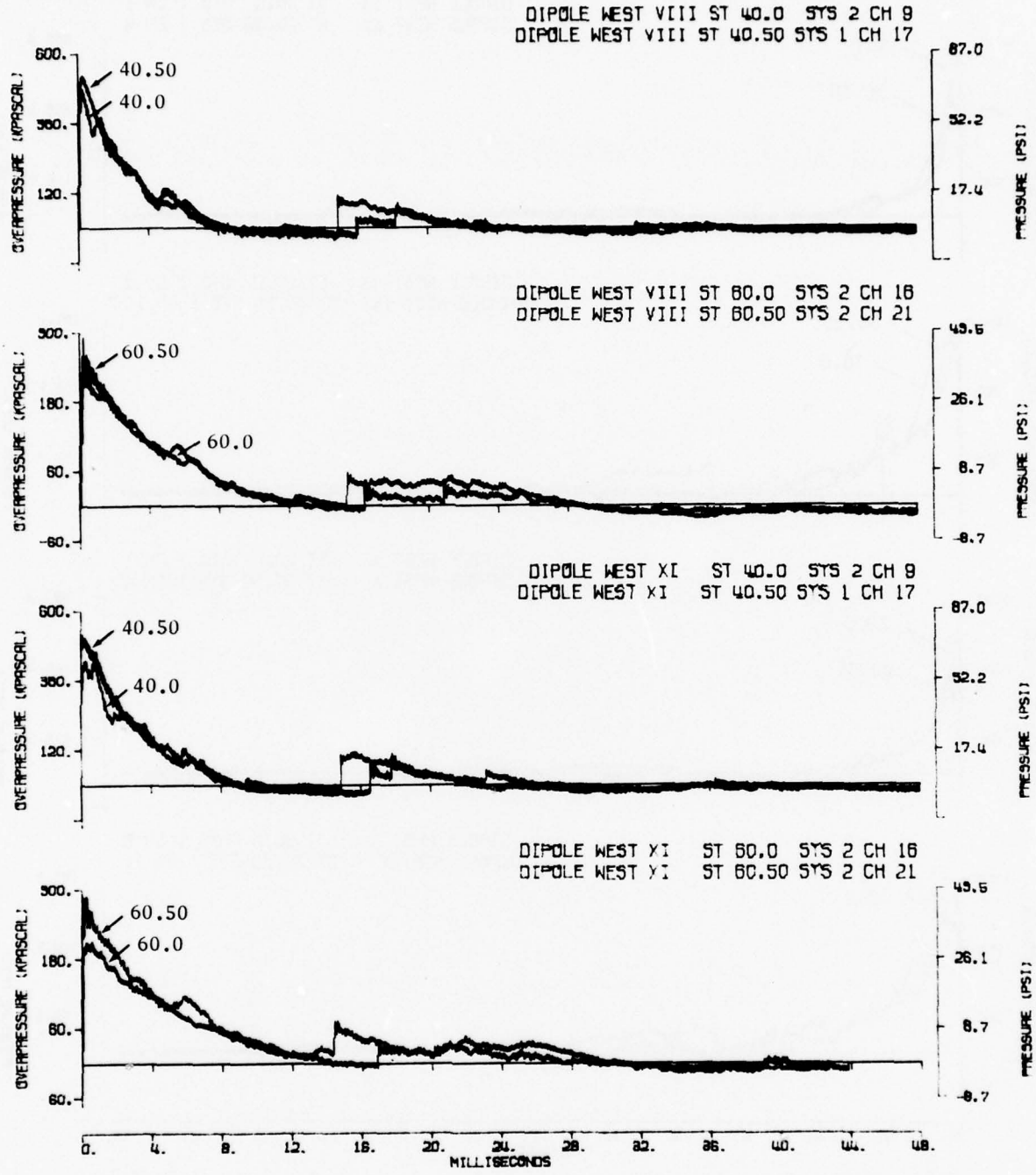

Figure 3.13. Comparison of Overpressure Records at Real and Ideal Surfaces; More Remote Stations, *Shots 8 and 11*

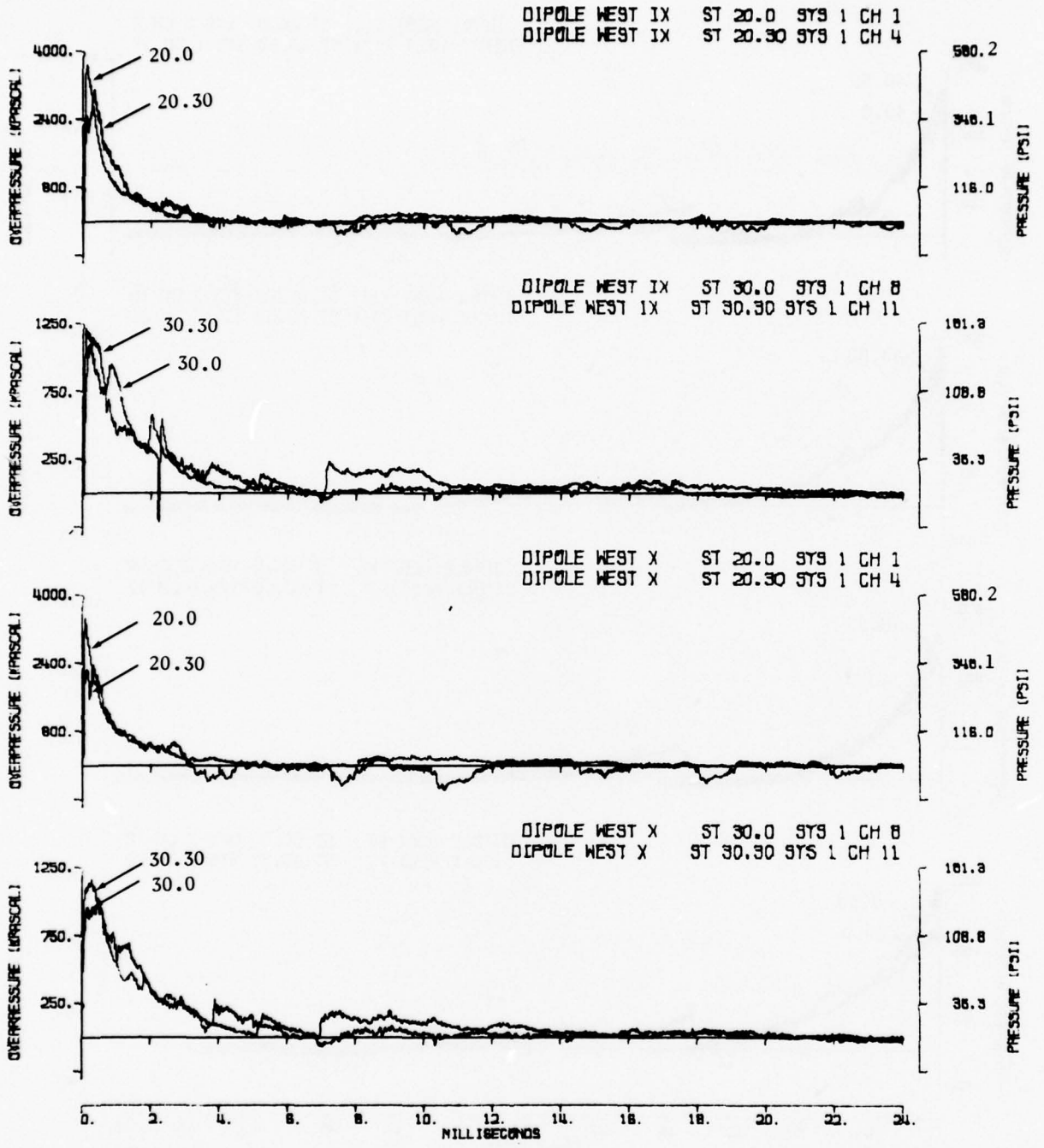

Figure 3.14. Comparison of Overpressure Records at Real and Ideal Surfaces; Close-In Stations, Shots 9 and 10

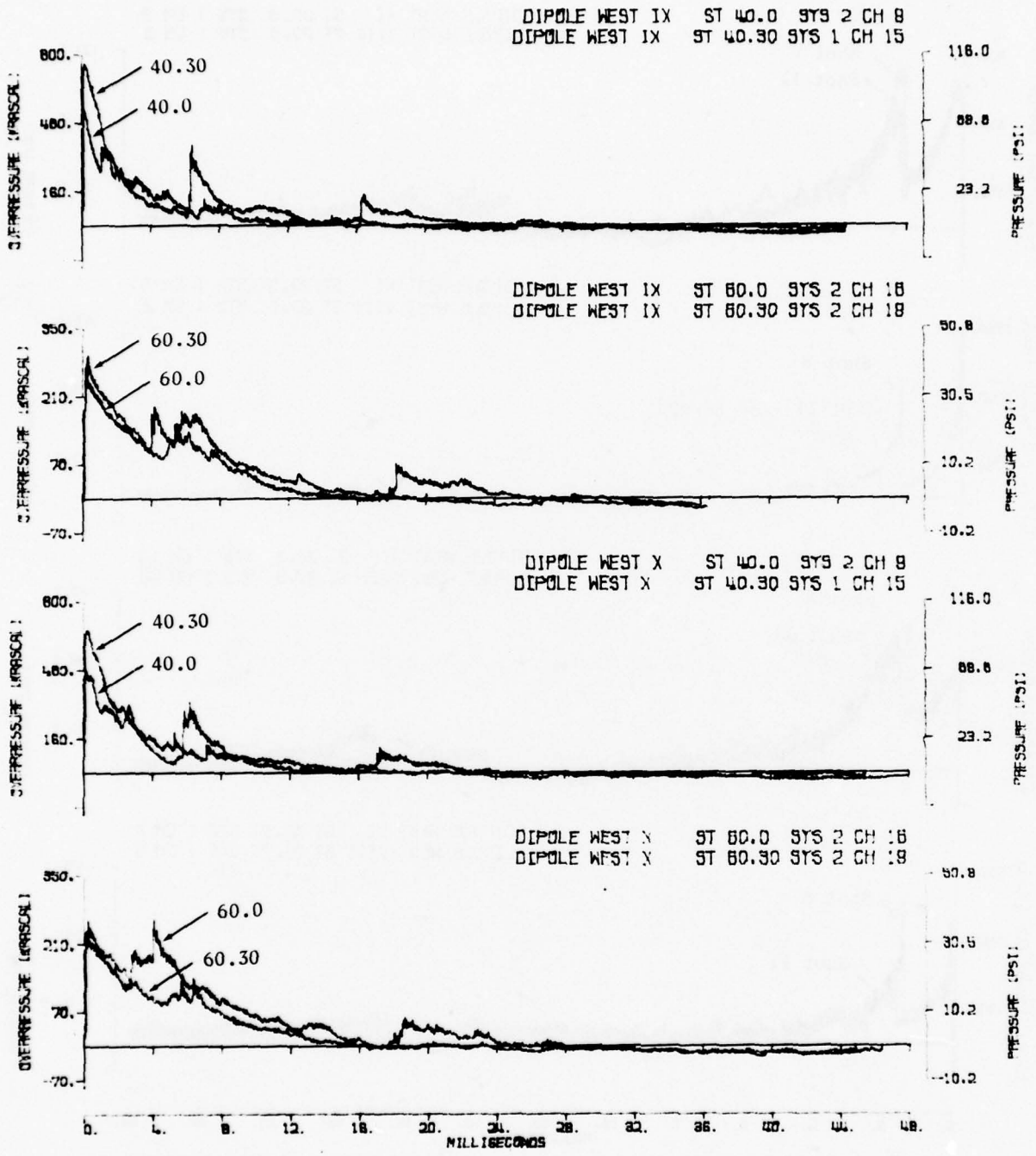

Figure 3.15. Comparison of Overpressure Records at Real and Ideal Surfaces; More Remote Stations, Shots 9 and 10

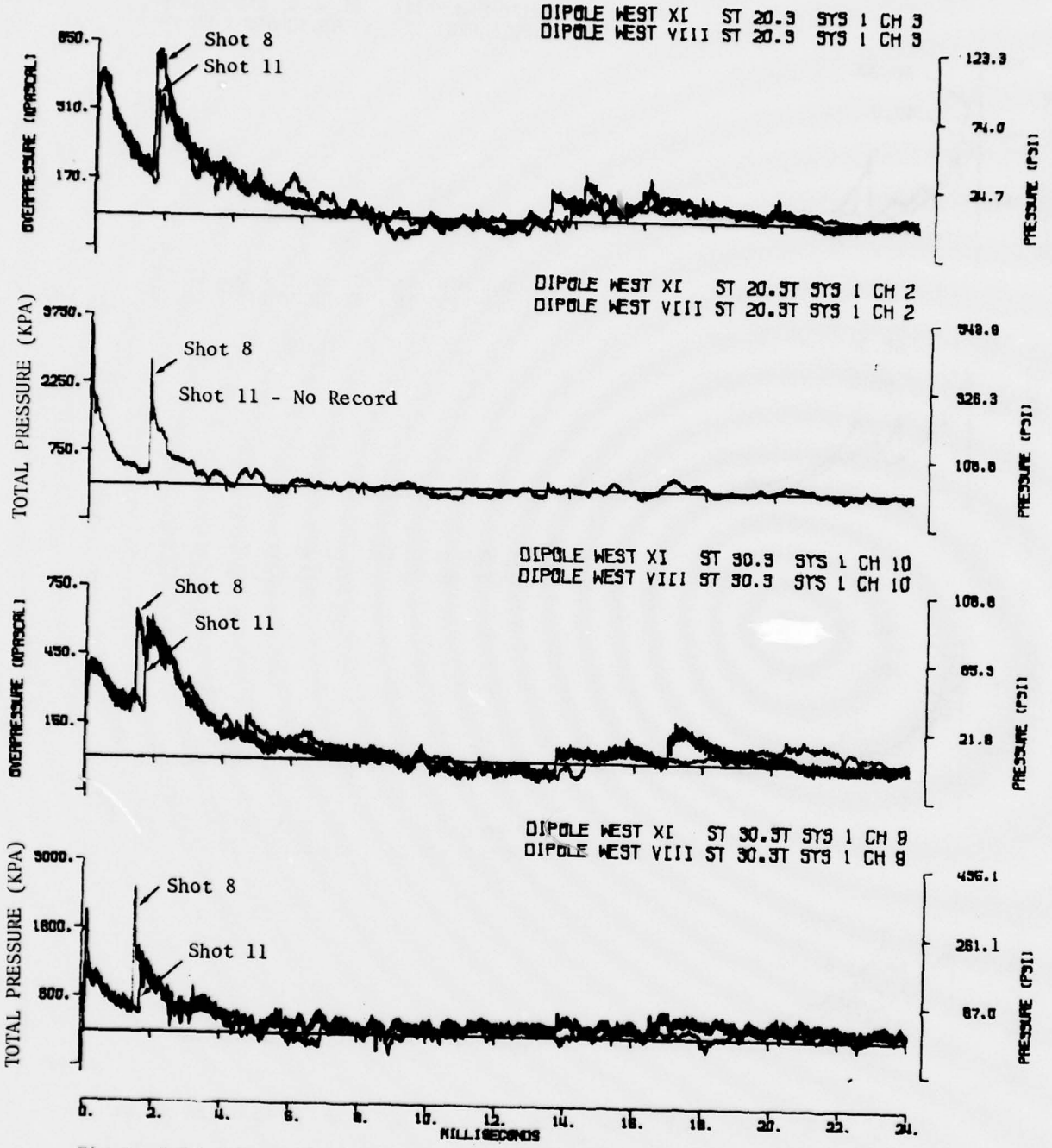

Figure 3.16. Comparison of Pressure Records Near Rough and Smooth Surfaces; Close-In Stations, Shots 8 and 11

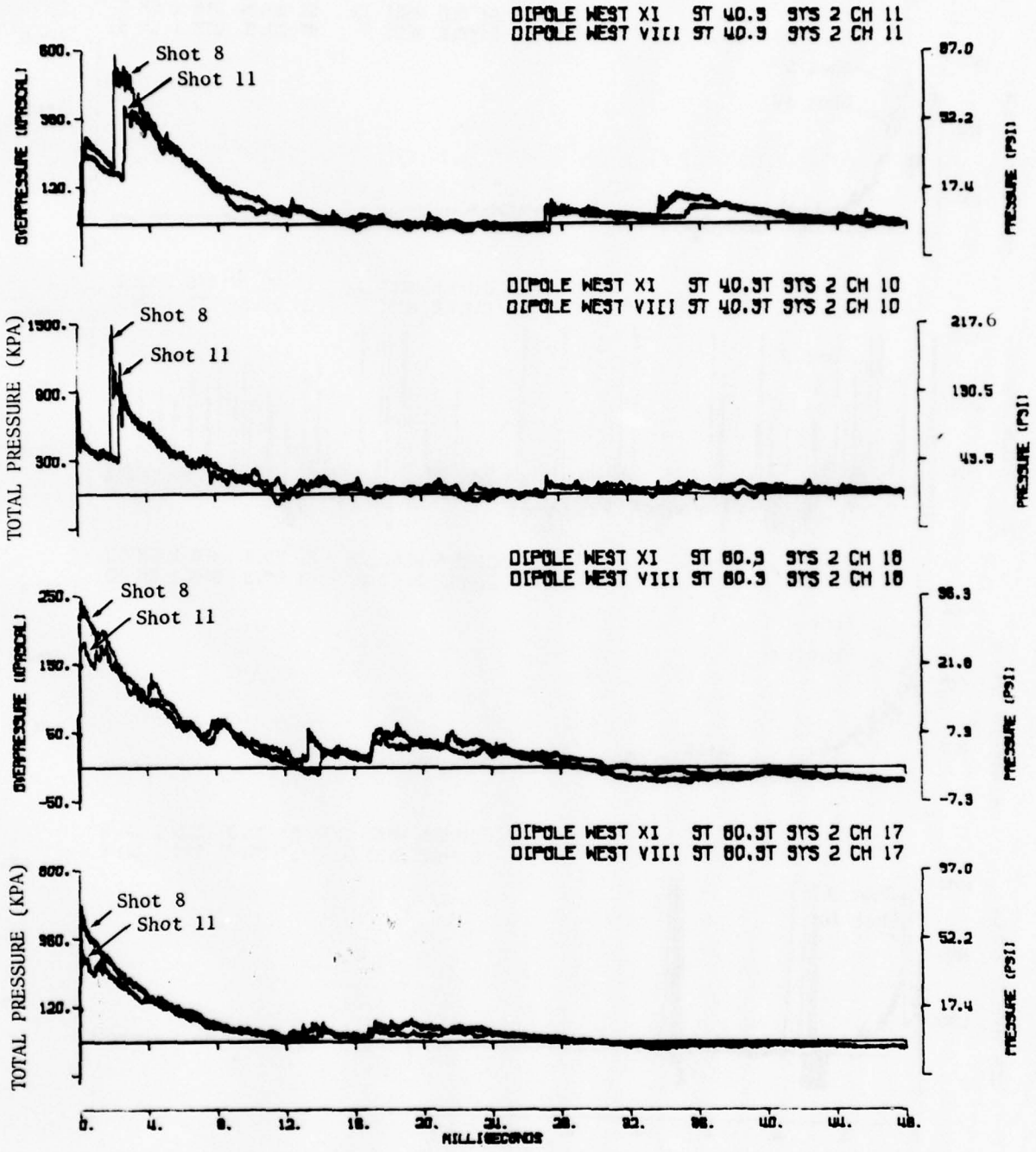

Figure 3.17. Comparison of Pressure Records Near Rough and Smooth Surfaces; More Remote Stations, Shots 8 and 11

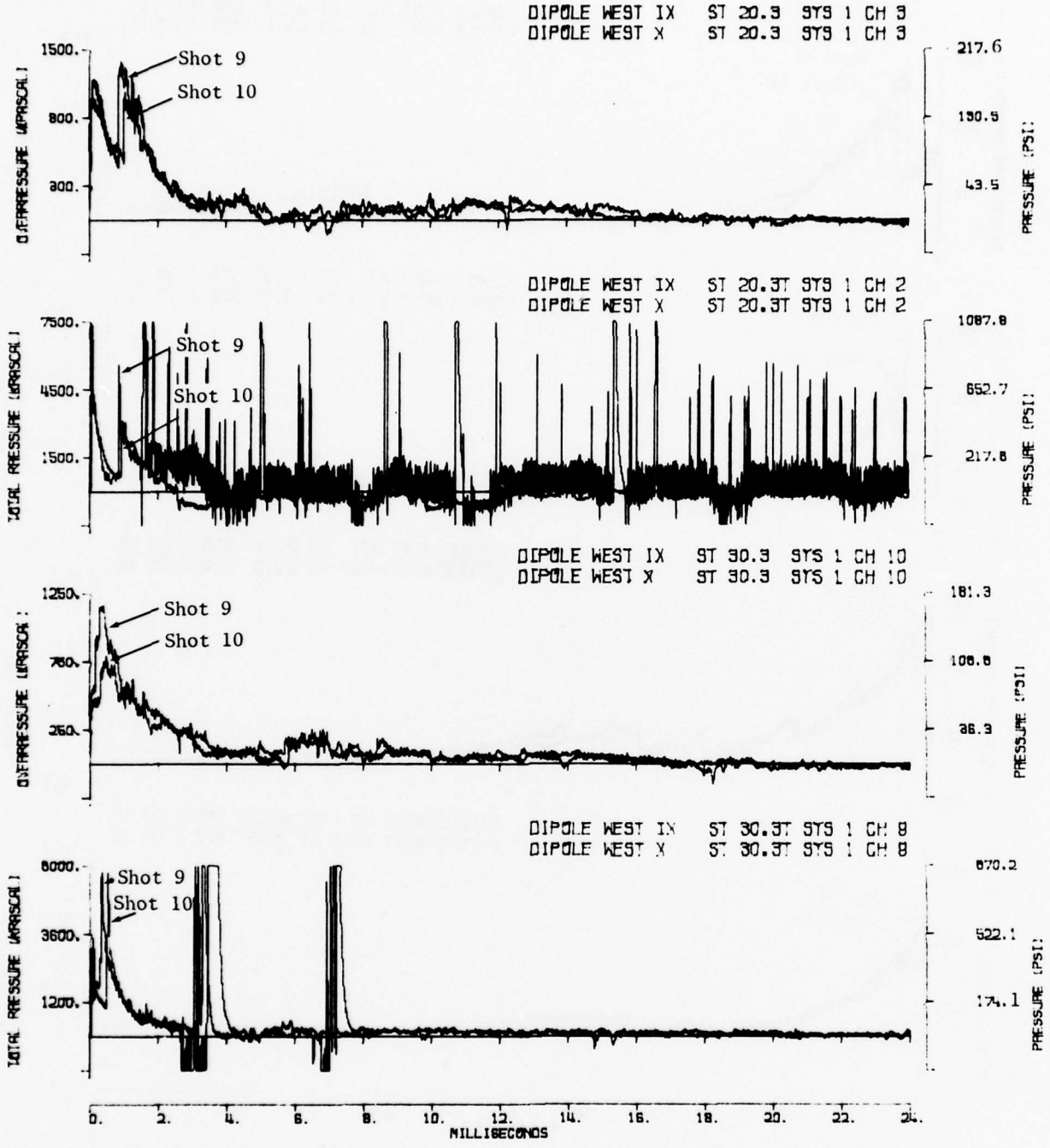

Figure 3.18. Comparison of Pressure Records Near Rough and Smooth Surfaces; Close-In Stations, Shots 9 and 10

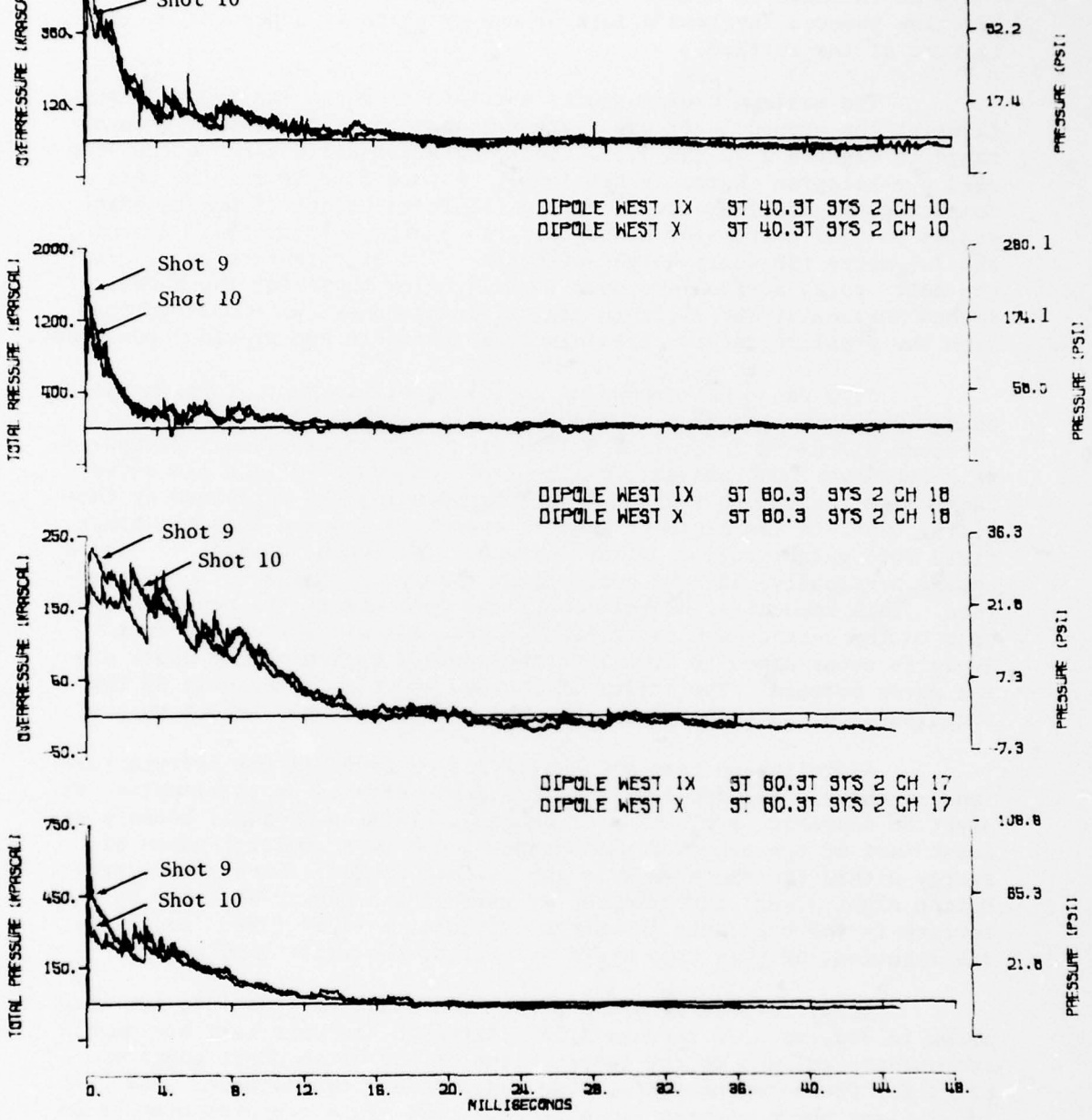

Figure 3.19. Comparison of Pressure Records Near Rough and Smooth Surfaces; More Remote Stations, Shots 9 and 10

furrowed surface fall below those from the hard surface. The secondary pulses, which arise from shock waves reflected from the surface, arrive later and are lower in magnitude when the surface is soft and rough as in Shots 10 and 11. The indication is clearly that the reflective process involves a loss of energy which is dependent on the texture of the surface.

The maximum overpressures obtained from the two types of surfaces at the ground level gages are presented as functions of ground range in Figures 3.20 and 3.21. These data are all scaled to the standard one-kilogram charge at sea level. Figure 3.20 is for the more compact configuration, the 4.6-metre (15-foot) height-of-burst, which scales to 0.57 metres for a one-kilogram charge. Figure 3.21 is for the 7.6-metre (25-foot) height-of-burst. The overpressure curves for the soft, rough surface are seen to fall below those for the hard, smooth surface at the close-in ranges, in agreement with observations from the pressure records themselves, as noted in the previous paragraph.

At a range corresponding approximately to that at which the change from single-charge to double-charge maximum overpressure occurs, as discussed in Section 3.3, a crossover takes place. Beyond this crossover, overpressure maxima from the rough surface lie above those from the smooth surface. The phenomenology is explained by theorizing that, in the close-in region, energy is removed from the blast field through absorption by the surface. The rough surface, as discussed previously, absorbs more energy than does the hard, smooth surface. This removal of energy lowers the pressure in the region adjacent to the surface and establishes a gradient whereby energy from above is constrained to move into the surface region as the shock system moves outward. The influx of energy, greater in the case of the rough surface, in turn raises the pressure at the more remote ranges.

A similar pattern of behavior is observed in the overpressure-impulse curves, Figures 3.22 and 3.23. The effects on the impulse, as might be expected, are not as pronounced. This is probably because at least part of the observed phenomenon is due to a redistribution of energy within the shock wave in the surface region. Such a redistribution might occur, for example, if part of the energy absorbed by the surface is fed back into the shock system at a later time. Local redistributions of this type would not affect the total impulse.

Ideal reflecting plane data, from elevated stations, are also shown in Figures 3.20 through 3.23. Although the data here are much less extensive due to the complication of having to mount gages on poles for these measurements, some observations can be made. The ideal plane overpressures lie above the real plane overpressures by as much as 10 to 30 percent. The ideal plane overpressure-impulses, on the other hand, are lower than the real plane overpressure-impulses by 5 to 10 percent. The first observation is consistent with the previous discussion; the second observation, apparently inconsistent,

(Text continued on page 59.)

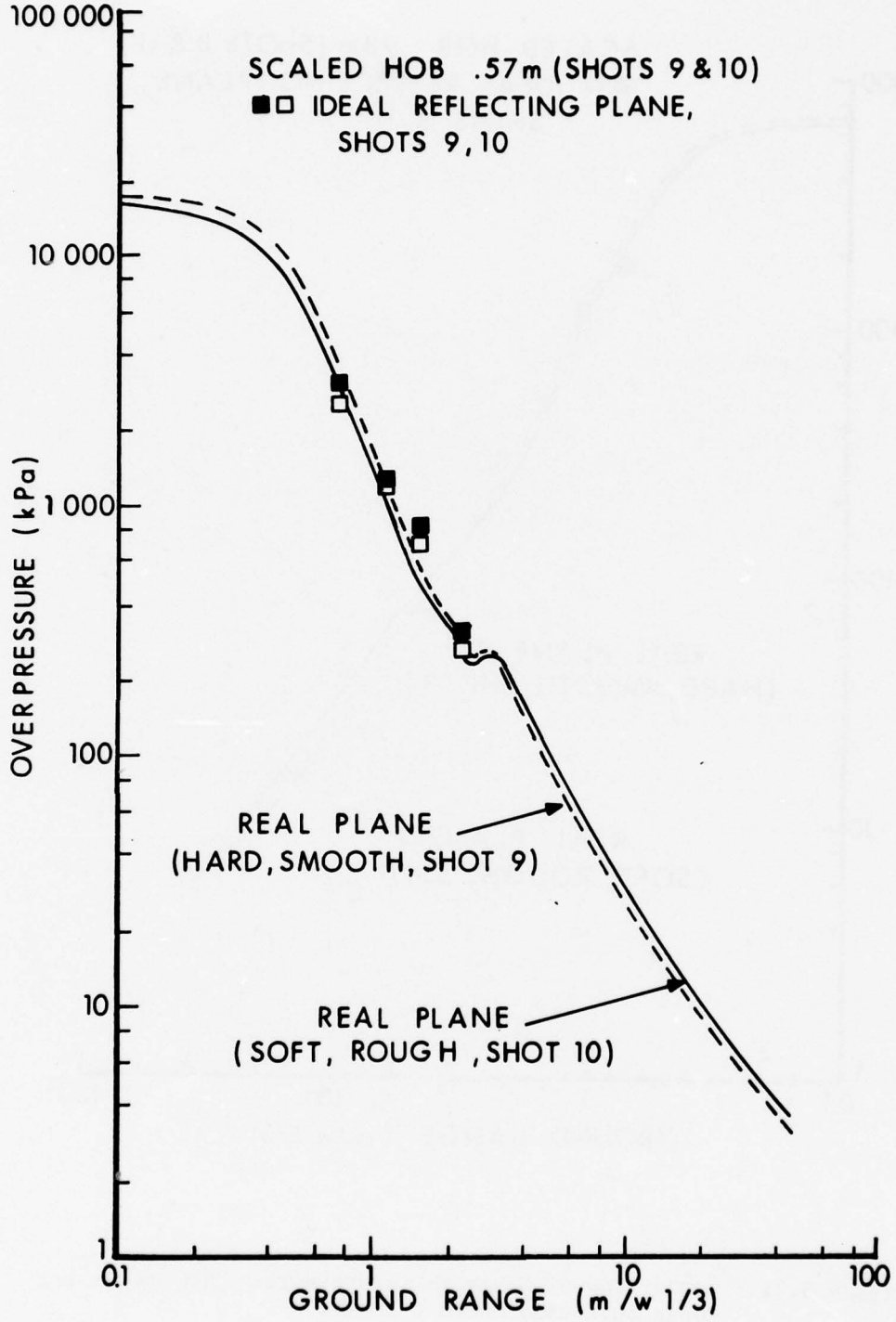

Figure 3.20. Comparison of Maximum Overpressures from Smooth and Rough Surfaces; Shots 9 and 10

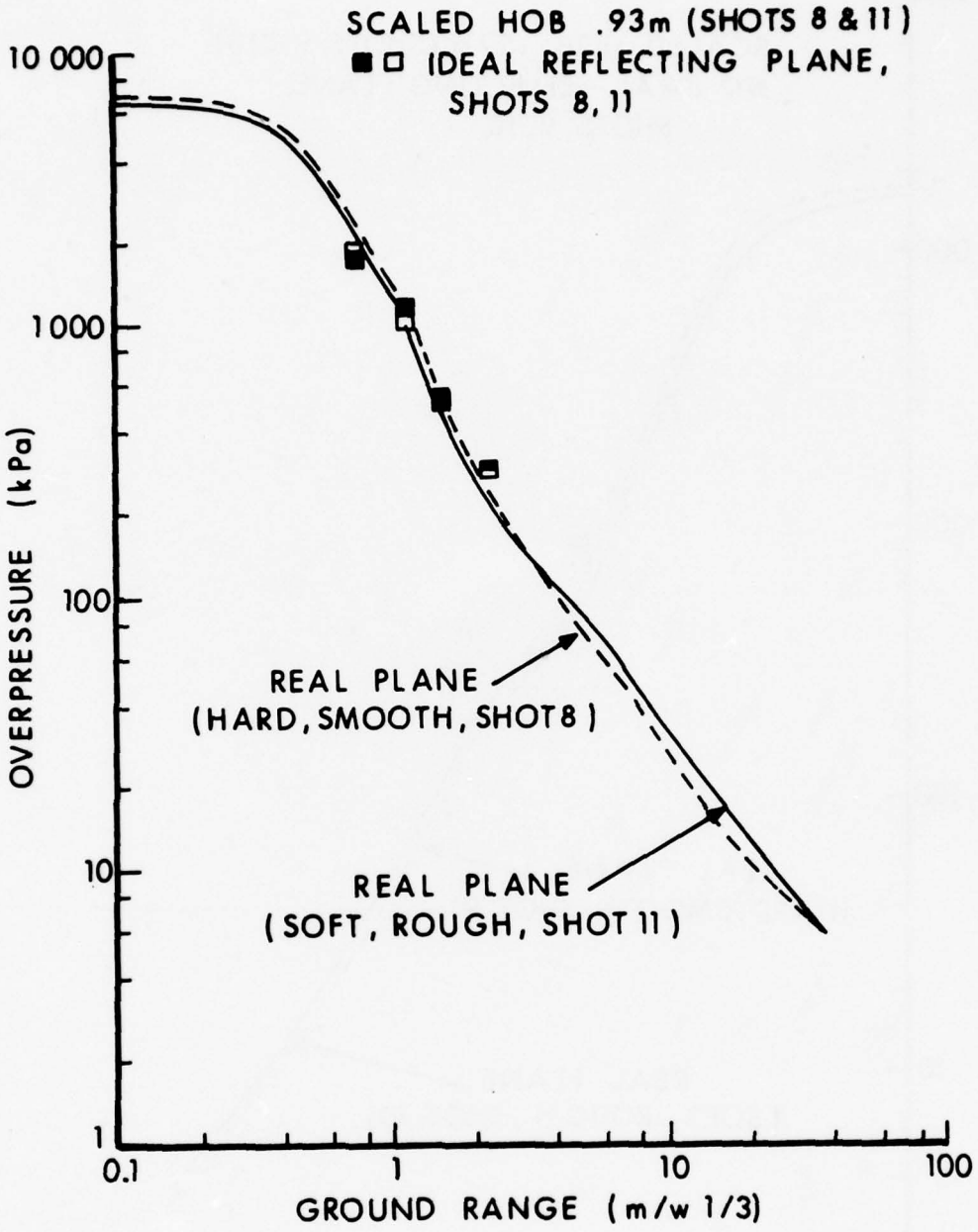

Figure 3.21. Comparison of Maximum Overpressures from Smooth and Rough Surfaces; Shots 8 and 11

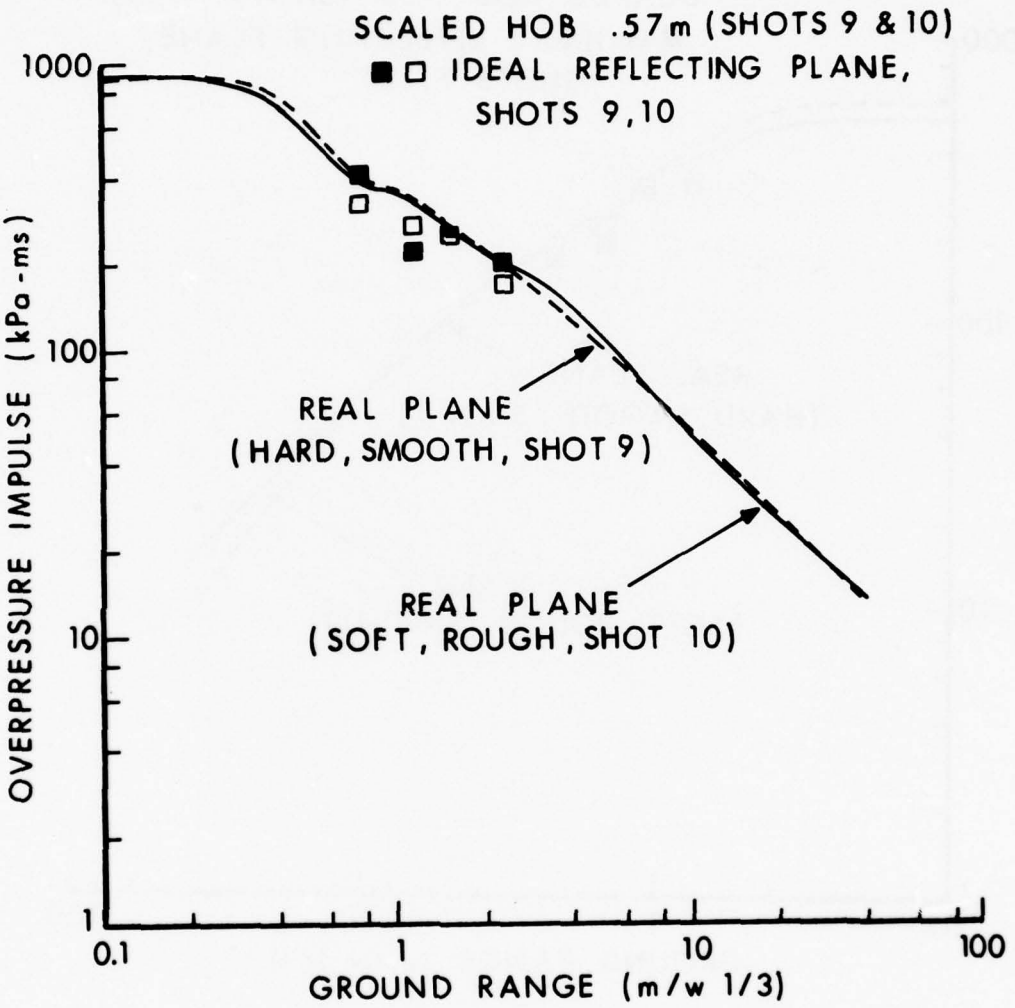

Figure 3.22. Comparison of Maximum Overpressure-Impulses from Smooth and Rough Surfaces; Shots 9 and 10

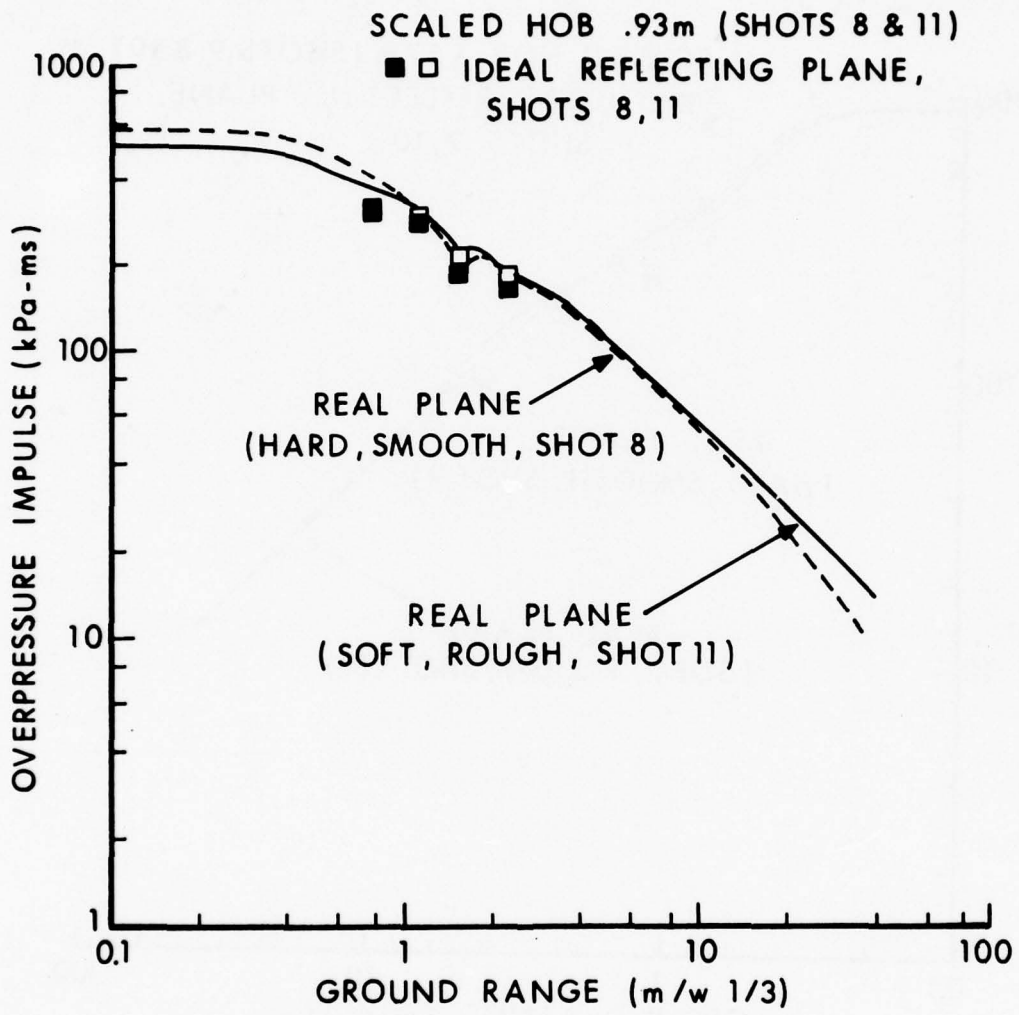

Figure 3.23. Comparison of Maximum Overpressure-Impulses from Smooth and Rough Surfaces; Shots 8 and 11

may result from data scatter or from the fact that measurement points were slightly off-plane.

The question of energy redistribution within a shock system as it passes over a surface is an interesting one, and on-going studies, at the University of Victoria and elsewhere, are addressing it. The observations discussed in this section are preliminary and largely qualitative. Additional results may be expected in future publications.

3.5 Dynamic Pressure Studies

Experimental dynamic pressure information was obtained using two quite different techniques. In the first technique, digitized side-on overpressure and total head pressure records from the electronic transducer array were treated point-by-point with a computer program to produce digital dynamic pressure records. The procedure, which included digital smoothing and then taking the difference (essentially) between corresponding side-on and total head points, is outlined in Reference 6. The dynamic pressure records obtained are also reproduced in this reference.

The second technique depended on data from high-speed photography of the movement of particles, or "smoke puffs," in the air flow. Photogrammetric and calculational techniques were used to develop particle velocity and density fields, from which the dynamic pressure fields were simply obtained from

$$q = \tfrac{1}{2}\rho u^2 ,$$

where q is dynamic pressure, ρ is density, and u is particle velocity. Details of this technique appear in Reference 8.

Dynamic pressure records obtained from the first technique are given in Figures 3.24 through 3.27. In each case, the dynamic pressure obtained just above the real reflecting plane (at 0.91 metres or 3 feet) is compared with that from just above the ideal reflecting plane (at 16.1 metres or 53 feet in Shots 8 and 11; at 10.0 metres or 33 feet in Shots 9 and 10). Except in a few cases where a bad or noisy total head record generated a correspondingly bad dynamic pressure, the records show good correlation. The result observed from the overpressure records in the previous section—namely, that records from near the real surface are somewhat degraded by absorption of energy into the ground—also appears in the dynamic pressures. Overpressure comparisons from the same stations at which the dynamic pressure comparisons were made are given in Figures 3.28 through 3.31. Note, however, that the time scales are not the same.

Scaled maximum dynamic pressure and dynamic pressure impulse values obtained close to the reflecting surfaces are plotted versus ground range in Figures 3.32 through 3.35. Although the data at the

(Text continued on page 72.)

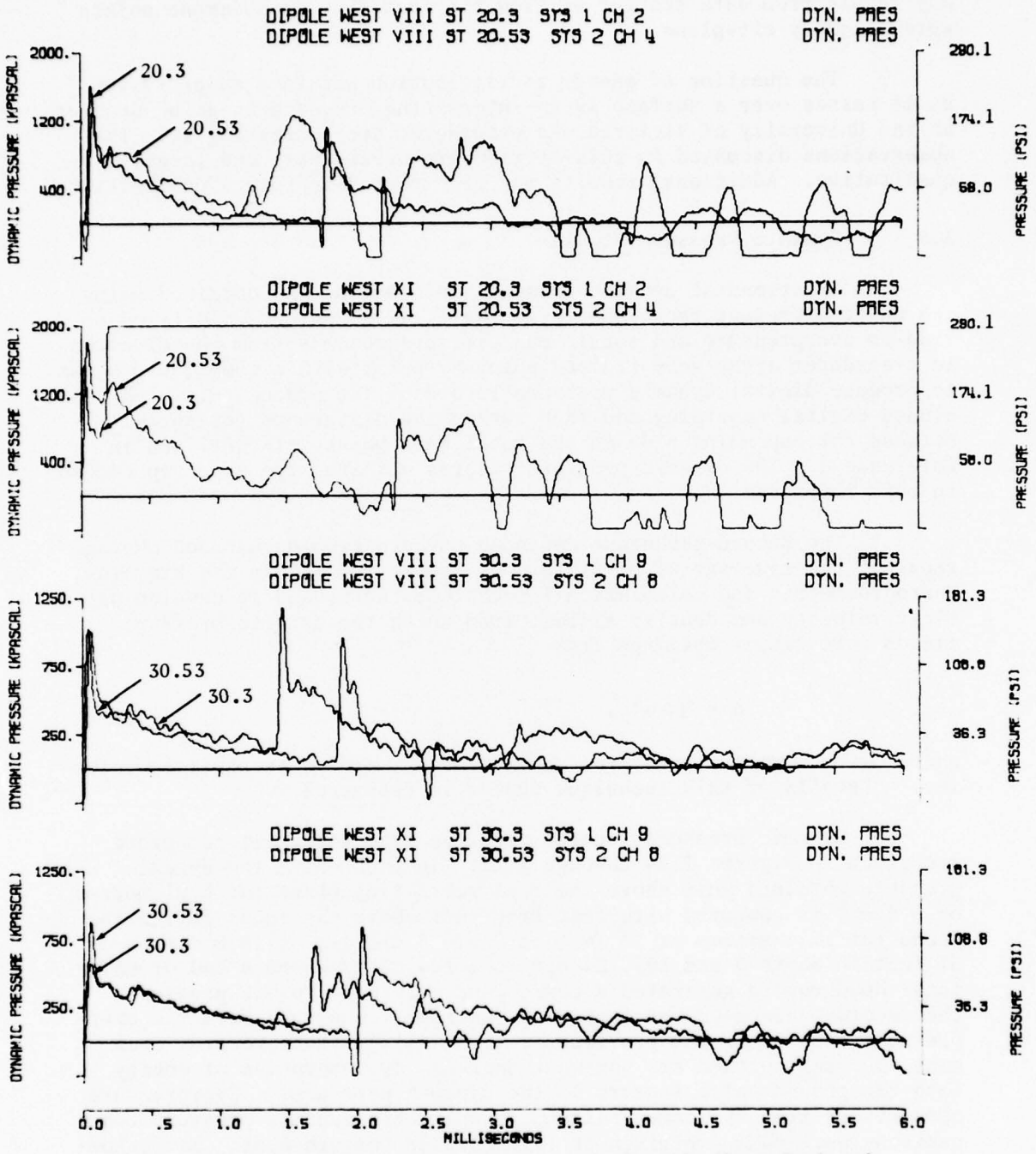

Figure 3.24. Comparison of Dynamic Pressure Records Above Real and Ideal Surfaces; Close-In Stations, Shots 8 and 11

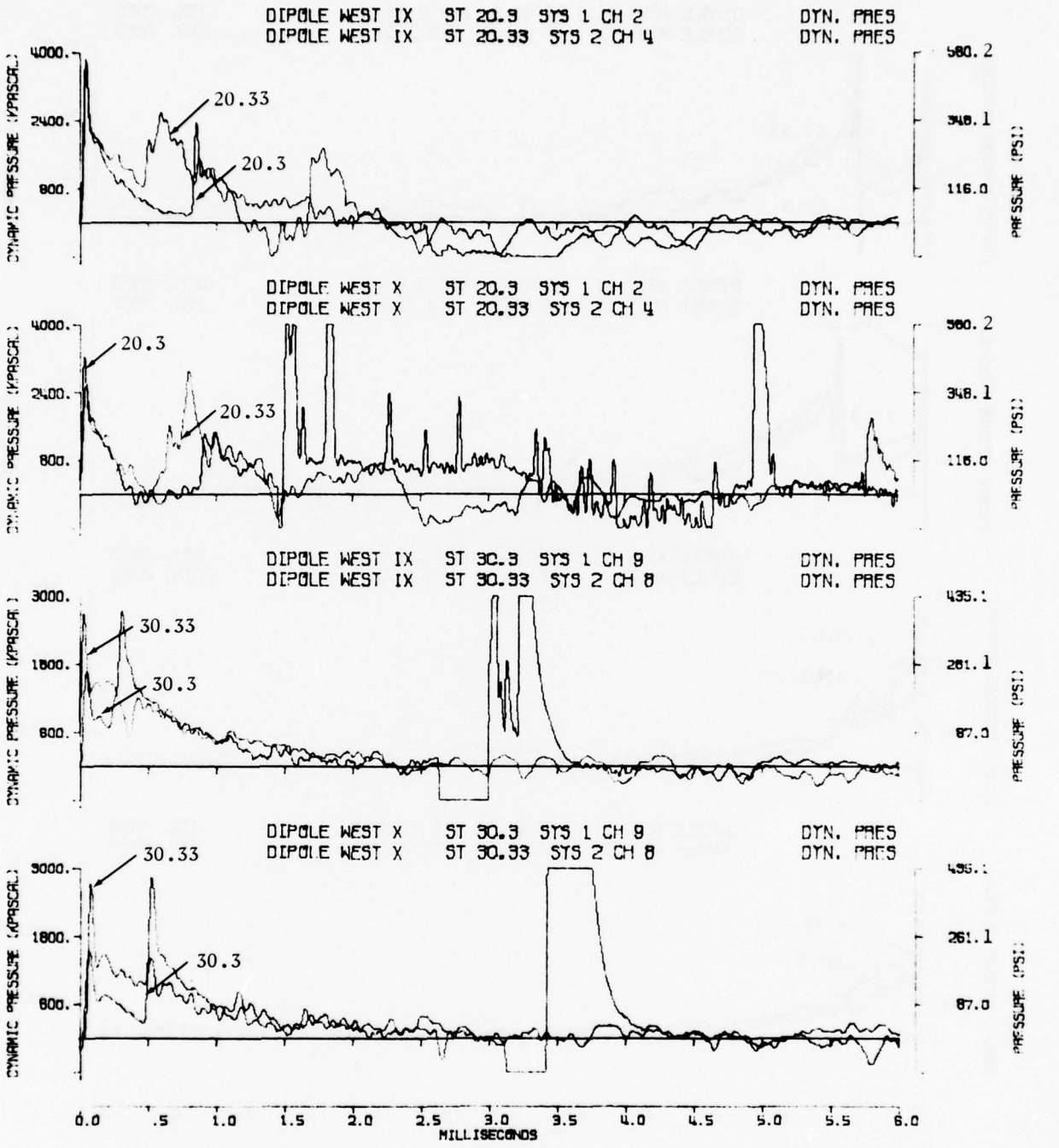

Figure 3.25. Comparison of Dynamic Pressure Records Above Real and Ideal Surfaces; Close-In Stations, Shots 9 and 10

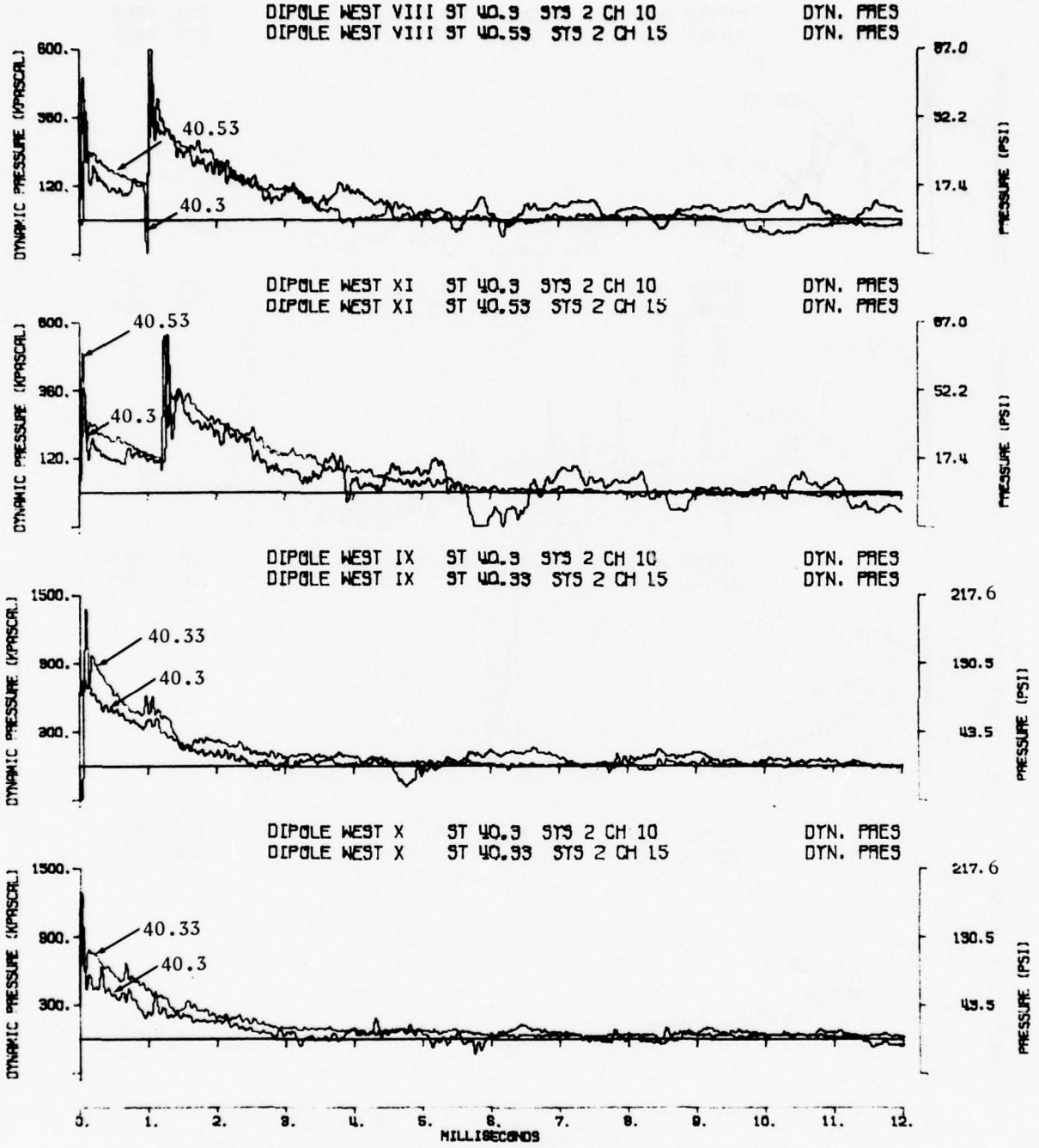

Figure 3.26. Comparison of Dynamic Pressure Records Above Real and Ideal Surfaces; 13.2-Metre (40-Foot) Stations

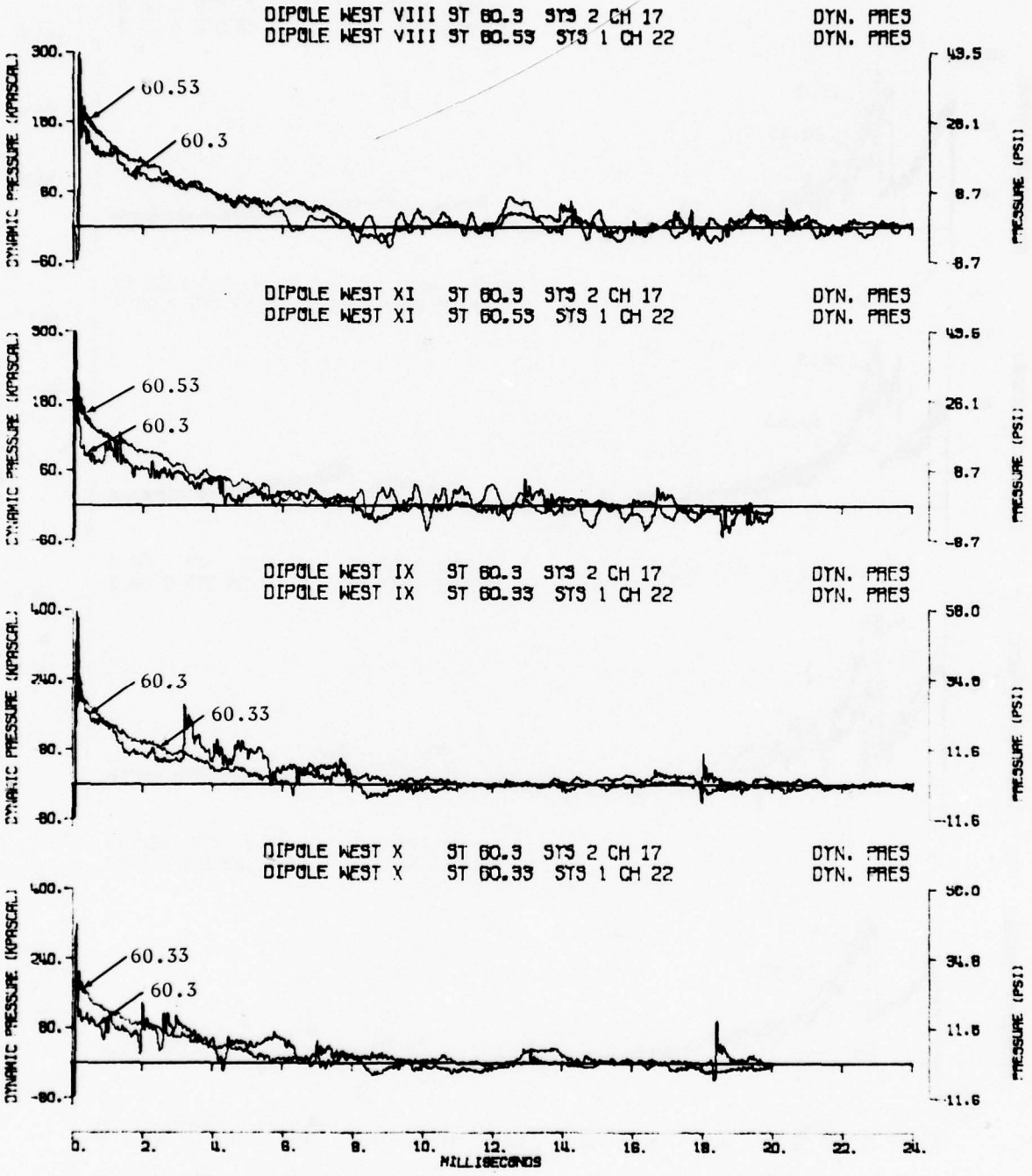

Figure 3.27. Comparison of Dynamic Pressure Records Above Real and Ideal Surfaces; 18.3-Metre (60-Foot) Stations

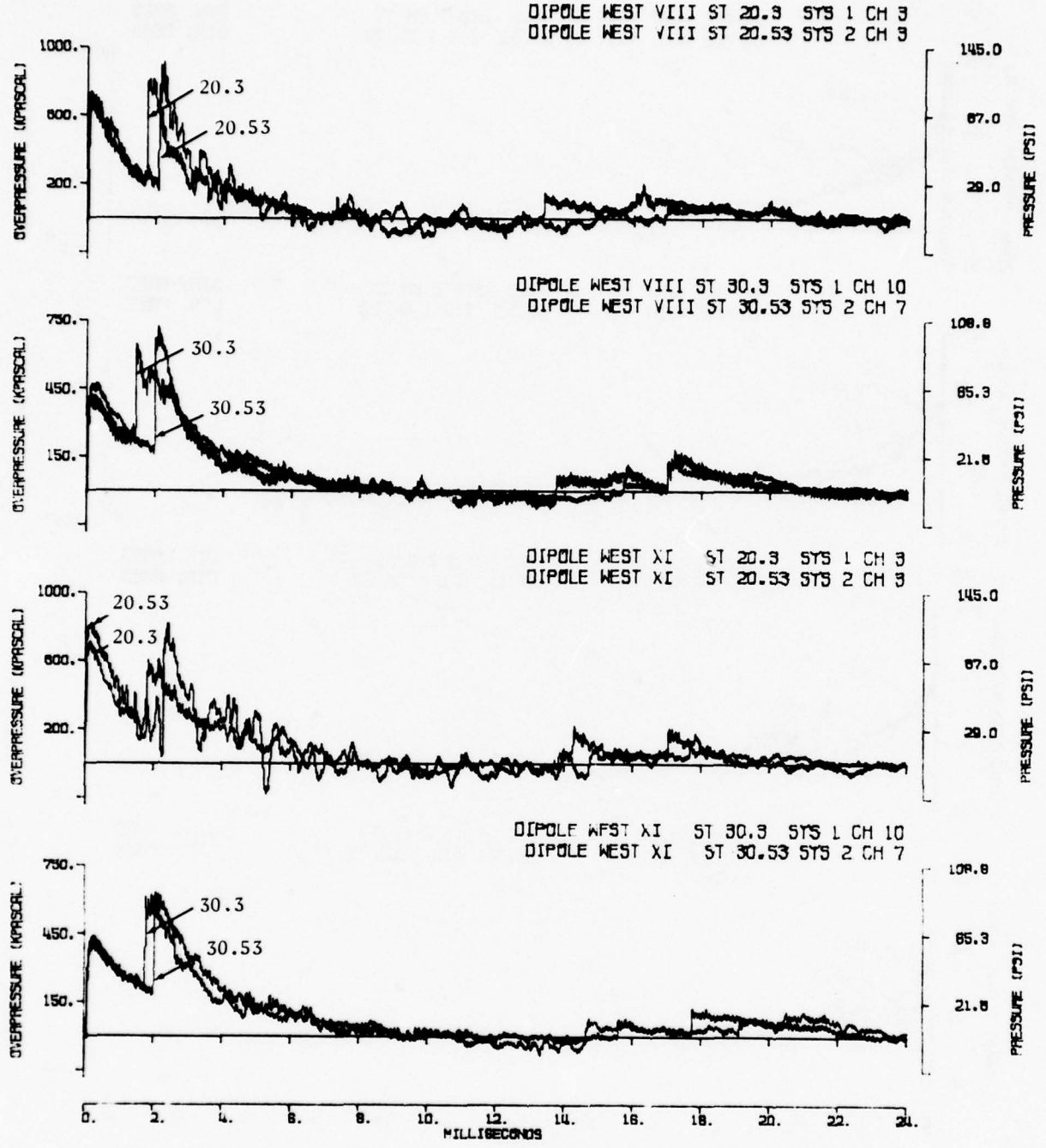

Figure 3.28. Comparison of Overpressure Records Above Real and Ideal Surfaces; Close-In Stations, Shots 8 and 11

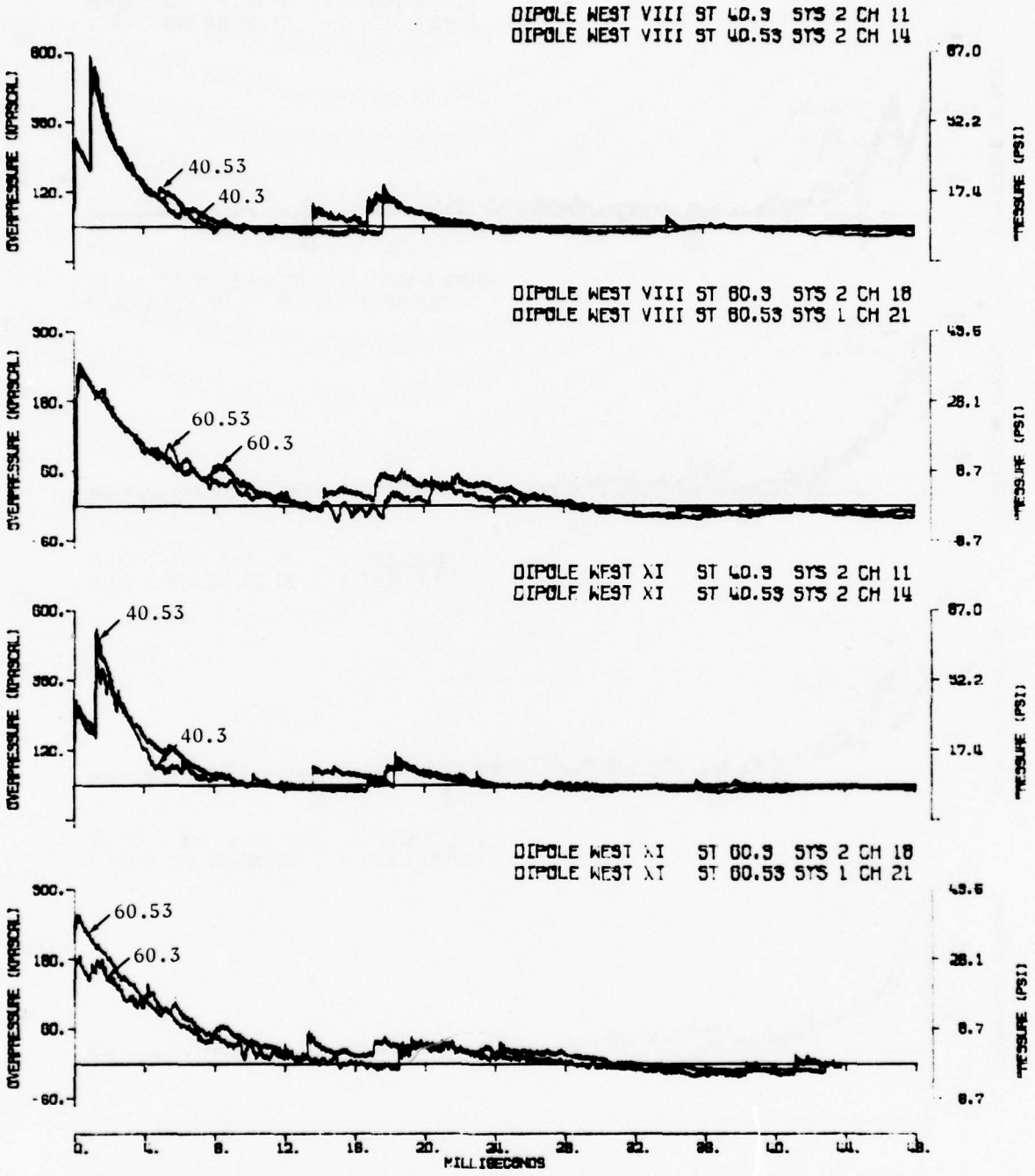

Figure 3.29. Comparison of Overpressure Records Above Real and Ideal Surfaces; More Remote Stations, Shots 8 and 11

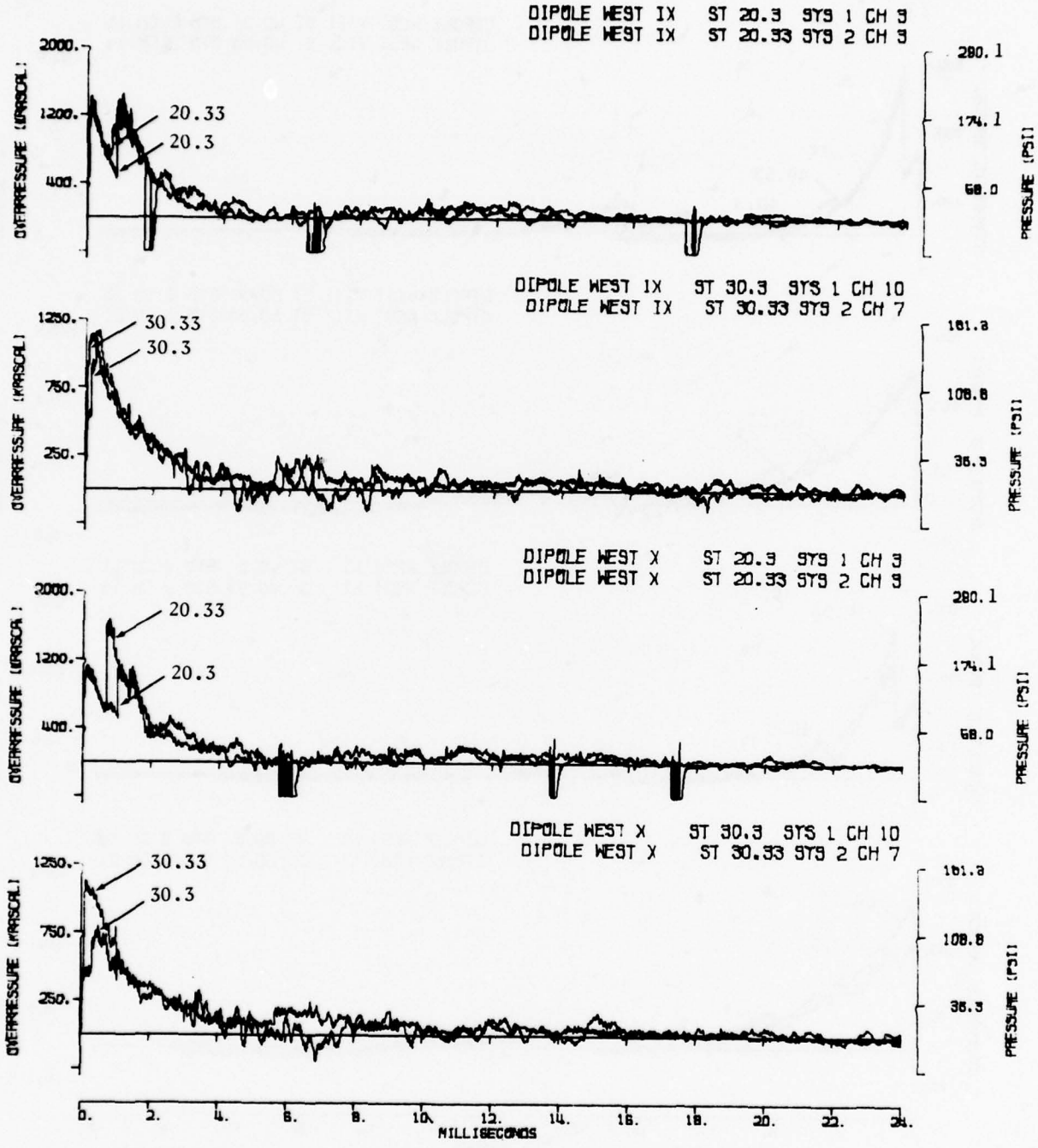

Figure 3.30. Comparison of Overpressure Records Above Real and Ideal Surfaces; Close-In Stations, Shots 9 and 10

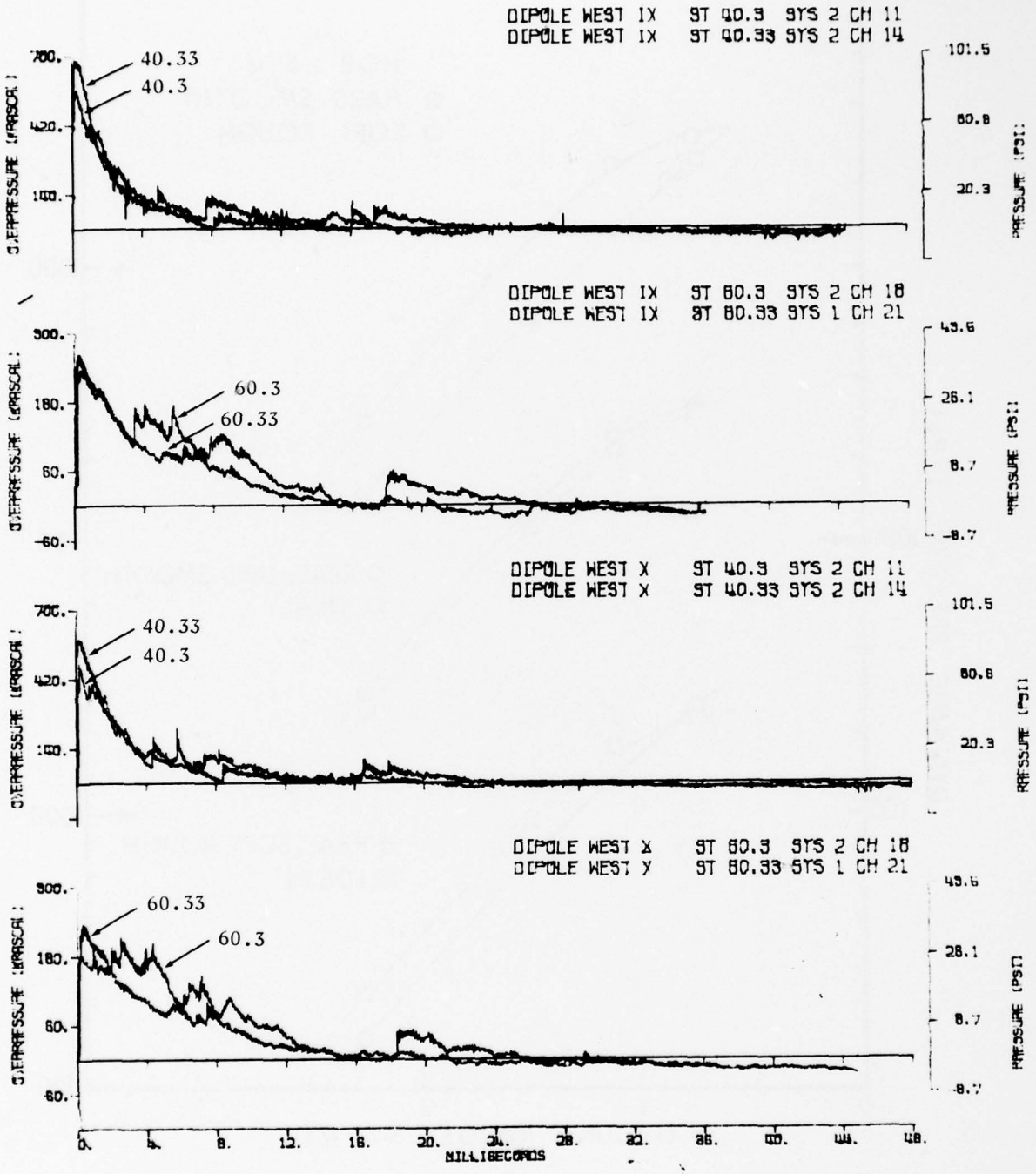

Figure 3.31. Comparison of Overpressure Records Above Real and Ideal Surfaces; More Remote Stations, Shots 9 and 10

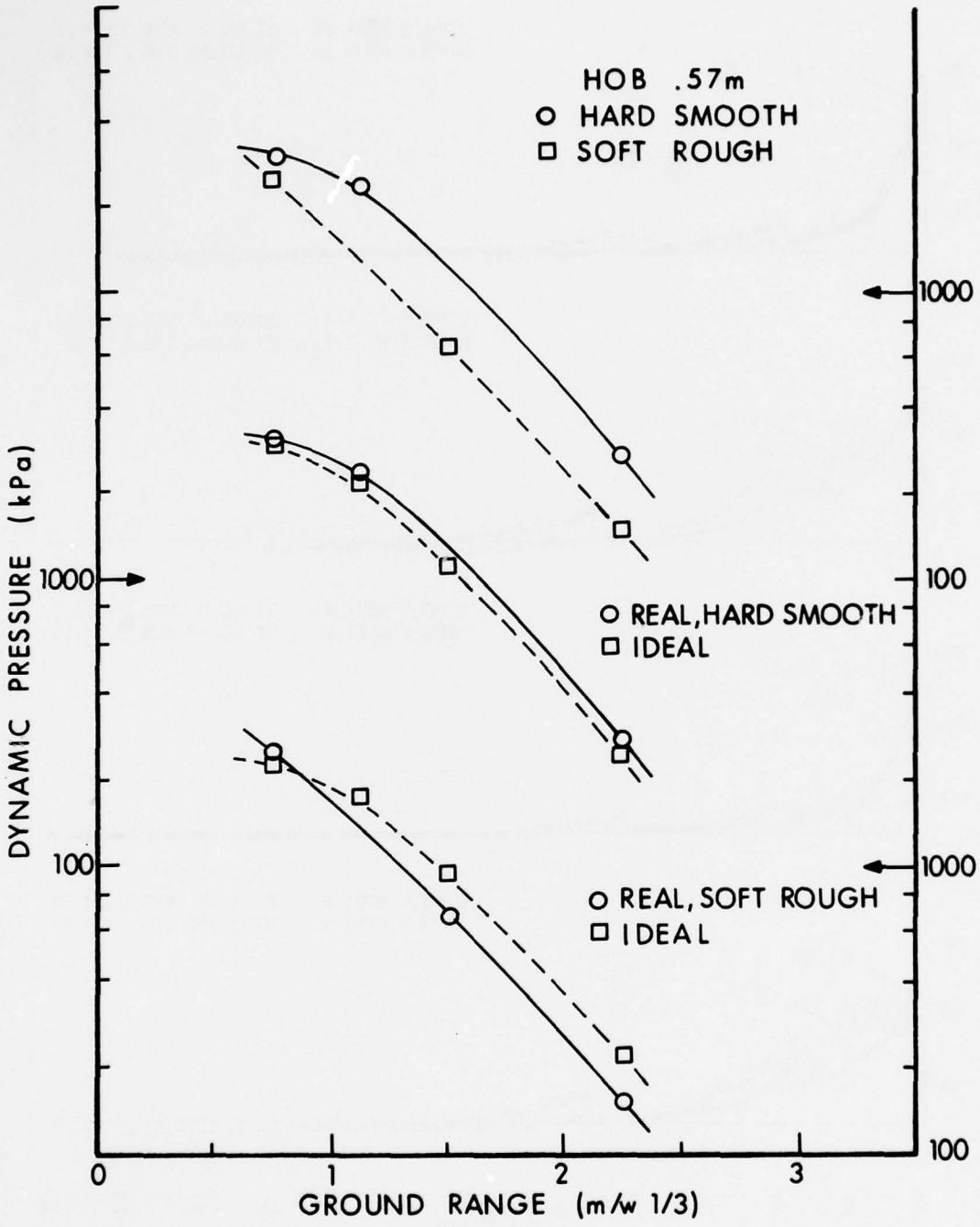

Figure 3.32. Comparison of Maximum Dynamic Pressures from Real and Ideal Surfaces; Shots 9 and 10

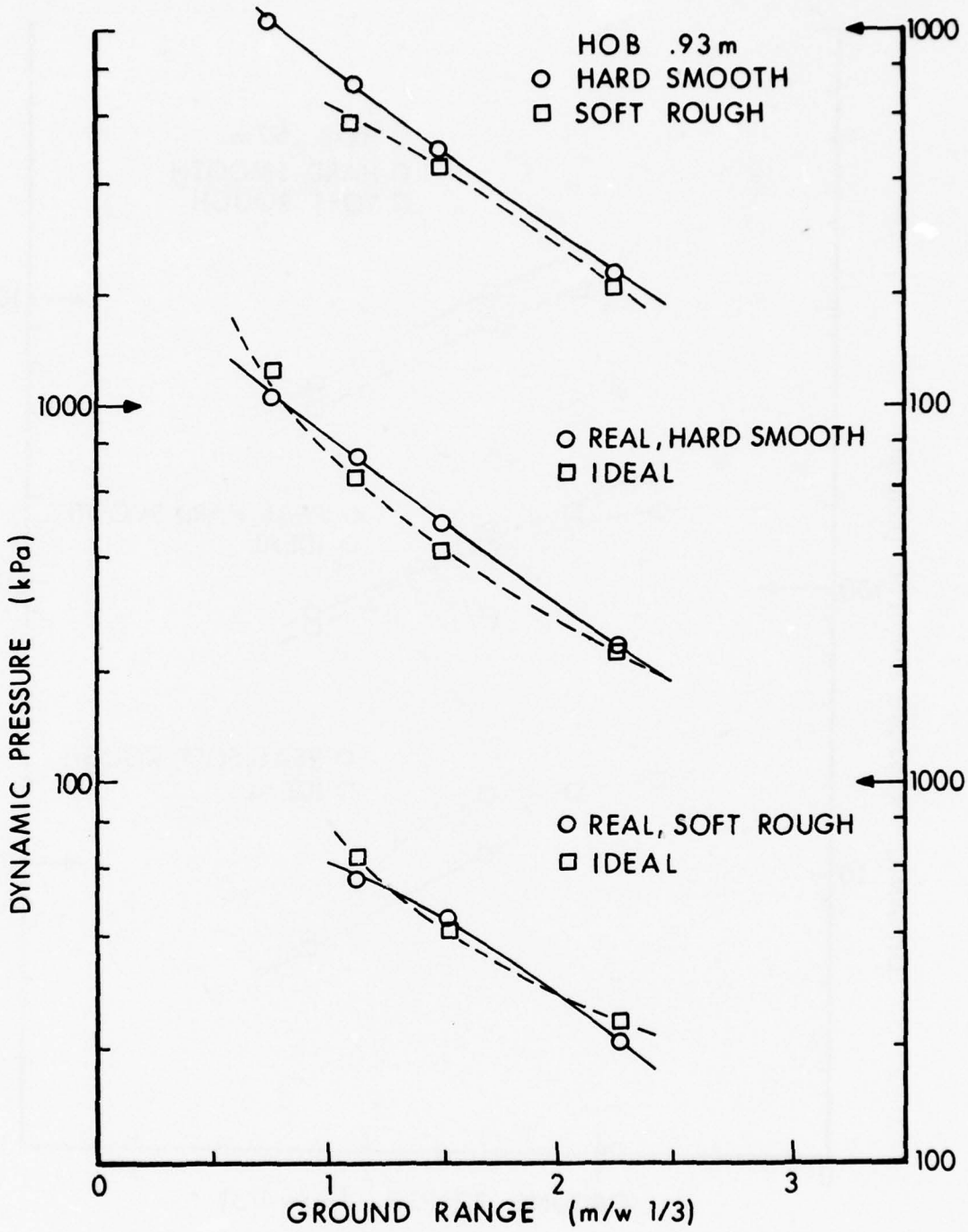

Figure 3.33. Comparison of Maximum Dynamic Pressures from Real and Ideal Surfaces; Shots 8 and 11

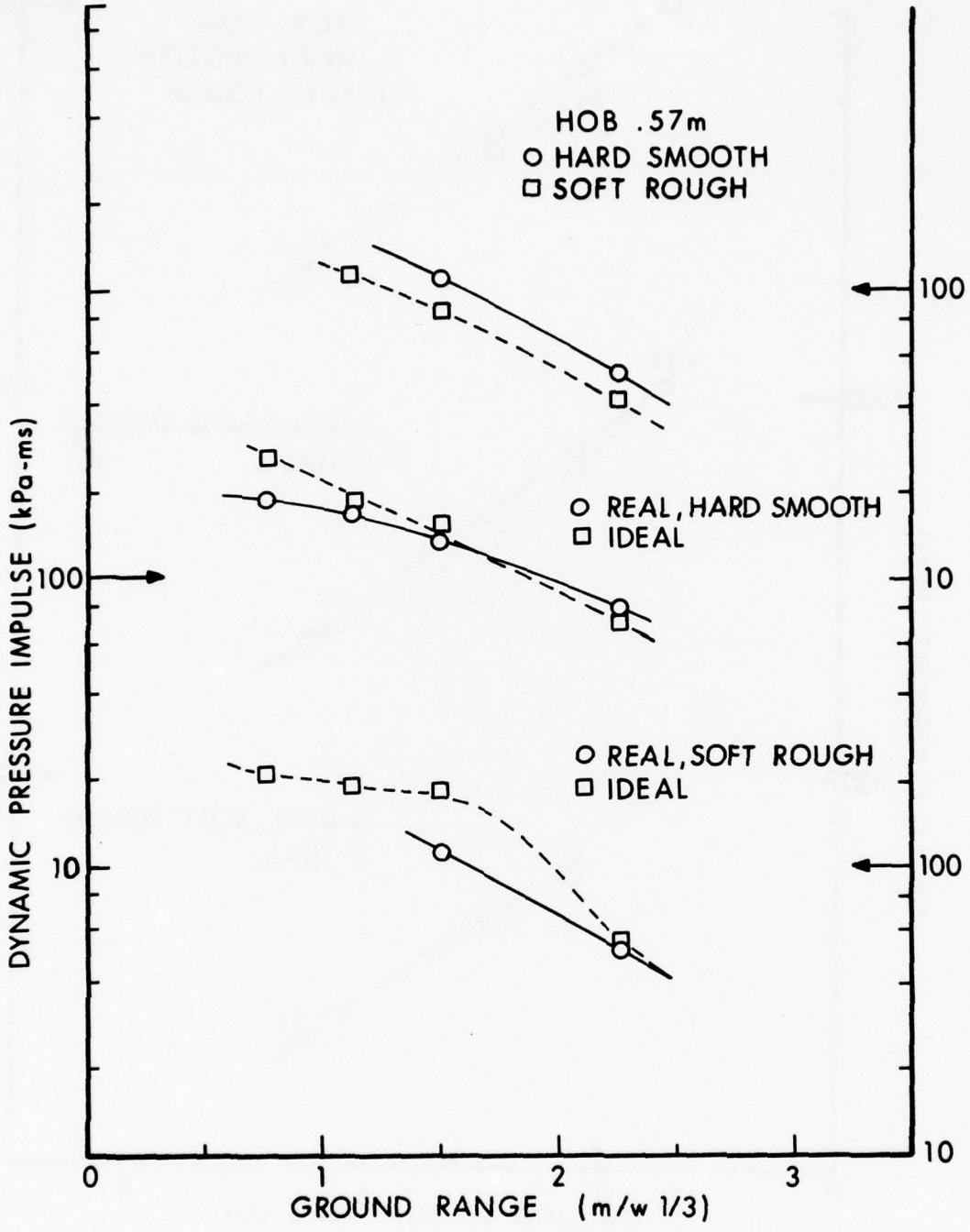

Figure 3.34. Comparison of Maximum Dynamic Pressure Impulses from Real and Ideal Surfaces; Shots 9 and 10

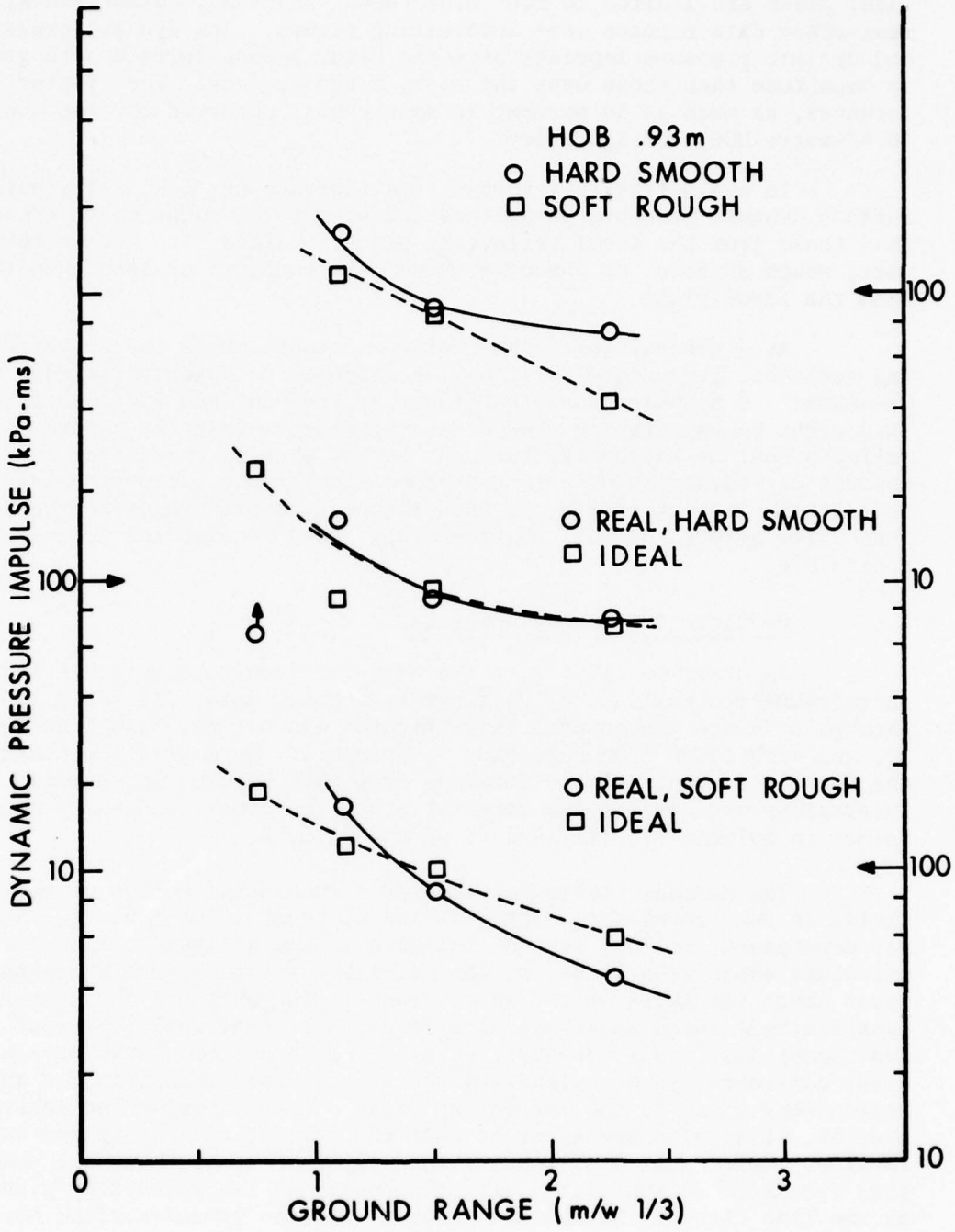

Figure 3.35. Comparison of Maximum Dynamic Pressure Impulses from Real and Ideal Surfaces; Shots 8 and 11

ideal plane are limited to four measurement stations, comparison with real-plane data exposes some interesting trends. The dynamic pressures and dynamic pressure impulses over the hard, smooth surface were greater in magnitude than those over the soft, rough surface. The greater differences, as much as 80 percent in some cases, occurred for the smaller (0.57-metre HOB) configuration.

In evaluating real versus ideal surface effects, the smooth-surface dynamic pressure parameters are seen to be equal to or greater than those from the ideal reflecting plane. Values obtained at the soft, rough surface, on the other hand, are equal to or less than those from the ideal plane.

As a general rule, the closer a detonation is to the reflecting surfaces, the greater will be the differences observed between overpressures and dynamic pressure effects at the real and ideal surfaces. This might be expected in view of the hypothesis that the harder surface reflects most of the energy incident on it, whereas the softer surface absorbs or redistributes a larger proportion of the incident energy. In a stronger shock region, as when the charges are closer to the surfaces, the effects of this phenomenology would be expected to be more noticeable.

3.6 Particle Trajectory Analysis

In order to illustrate the kinds of results obtainable from photogrammetric analysis of particle trajectory data, Figures 3.36 through 3.45 are presented. These figures are all for DIPOLE WEST Shot 10, and were taken from Reference 8, Volume I. More detail concerning the Shot 10 analysis may be obtained from that volume, and similar illustrations and descriptive material about the other events are contained in Volumes II, III, and IV of Reference 8.

The particle trajectory analysis considered motion of the particles in two dimensions: vertical and horizontal (or radial). Angular dependence, if any, was not included in the analysis. In order to calculate shock velocities, it was necessary to make certain assumptions about the shape of the shock fronts. The shape of the primary (unreflected) shock waves was considered to be spherical (circular in two dimensions) about the burst point. The Mach-stem shocks were at first considered to be cylindrical (linear in two dimensions) in the region very close to the reflecting plane. In performing the analysis, however, it soon became apparent that the cylindrical assumption was invalid. More consistent results were obtained by assuming the Mach-stem shocks to be spherical, with the center at the reflecting plane on the line through the charge centers. For the ground-surface Mach stem, the center of the sphere corresponds to the Ground Zero point.

It is clear that the assumption of spherical Mach stems is at best a first-order approximation, and that large deviations from the spherical shape will occur as the Mach stem grows from the surface.

(Text continued on page 83.)

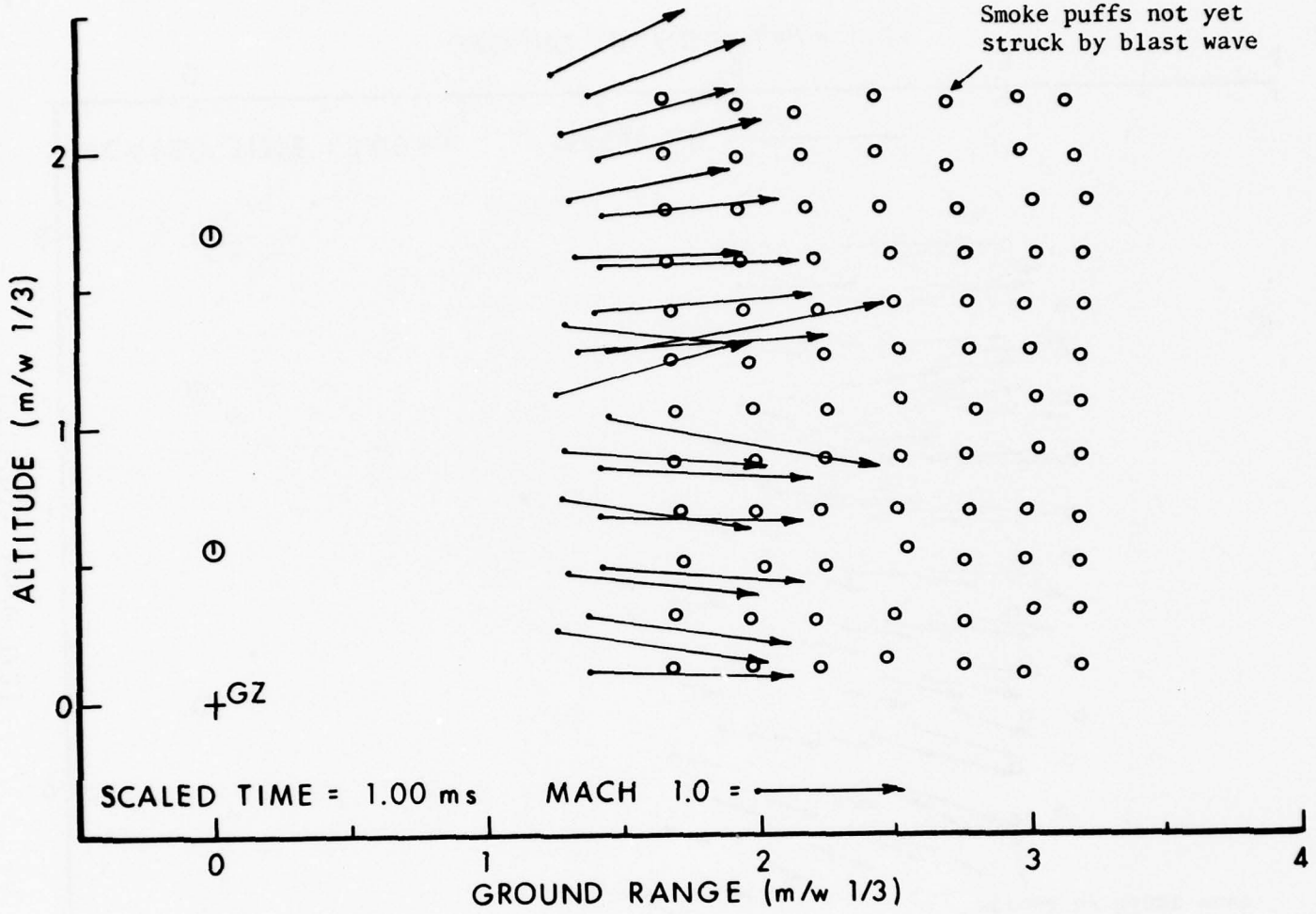

Figure 3.36. Velocity Field from Particle Trajectory Analysis at a Scaled Time of 1 Millisecond; Shot 10

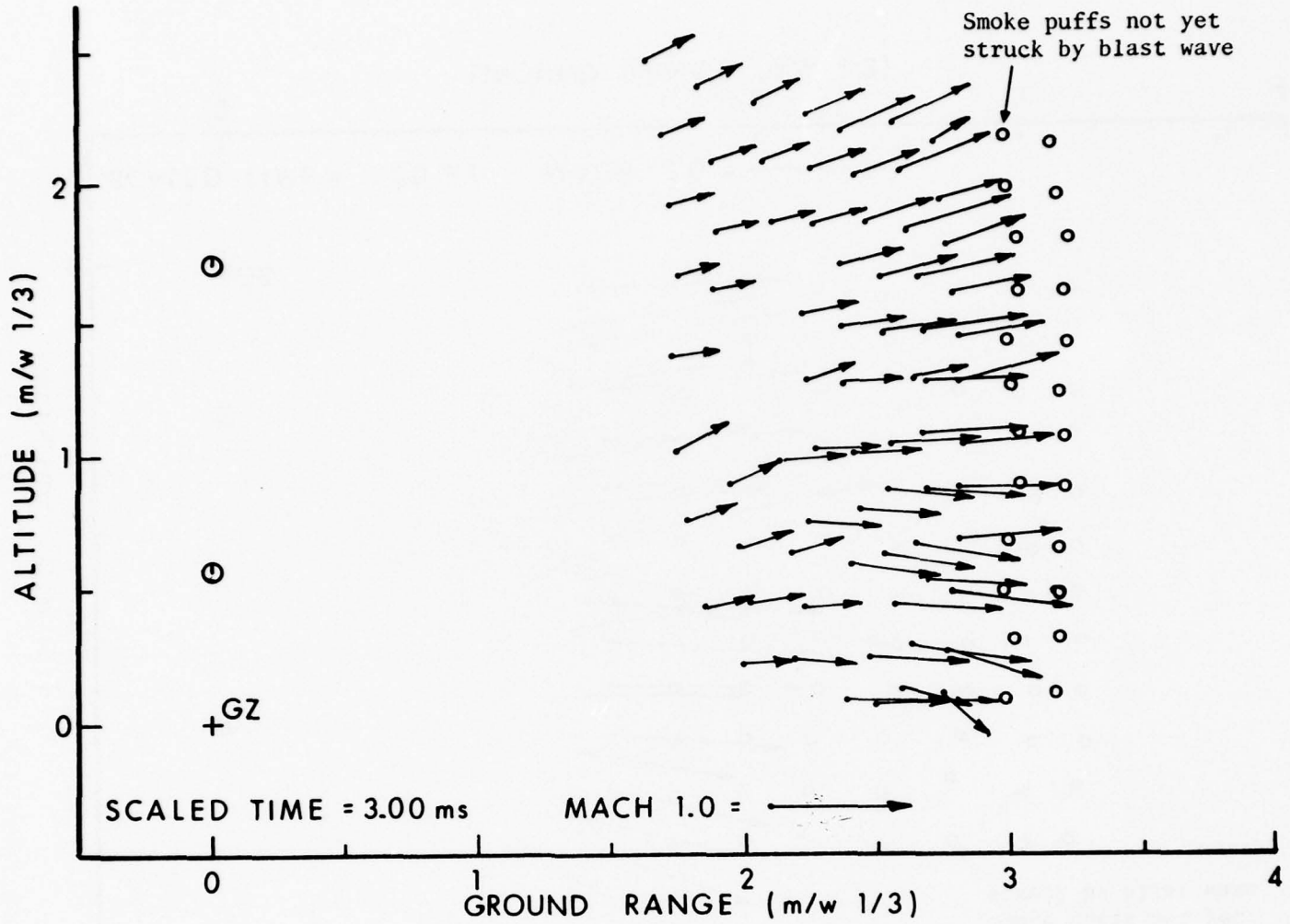

Figure 3.37. Velocity Field from Particle Trajectory Analysis at a Scaled Time of 3 Milliseconds; Shot 10

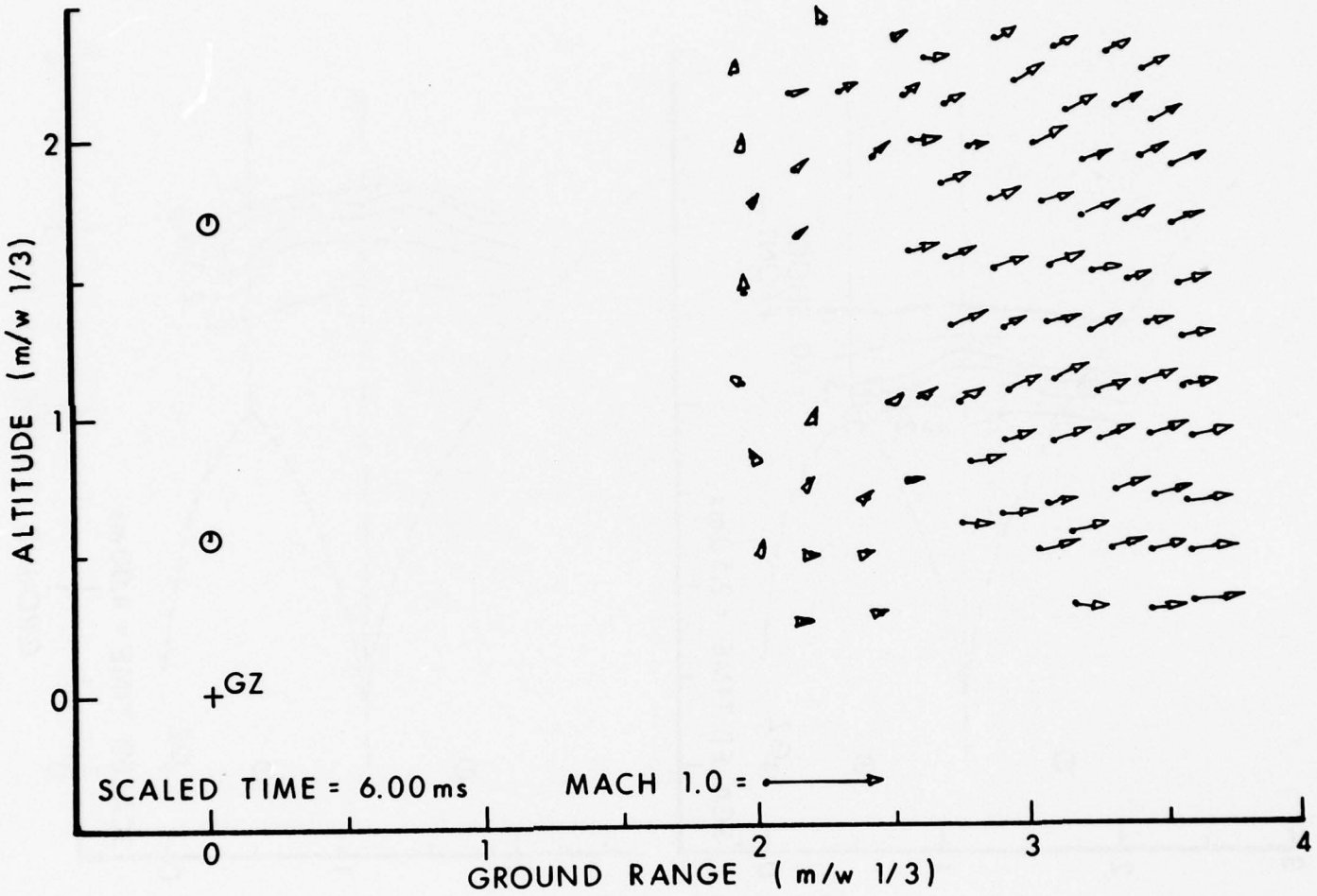

Figure 3.38. Velocity Field from Particle Trajectory Analysis at a Scaled Time of 6 Milliseconds; Shot 10

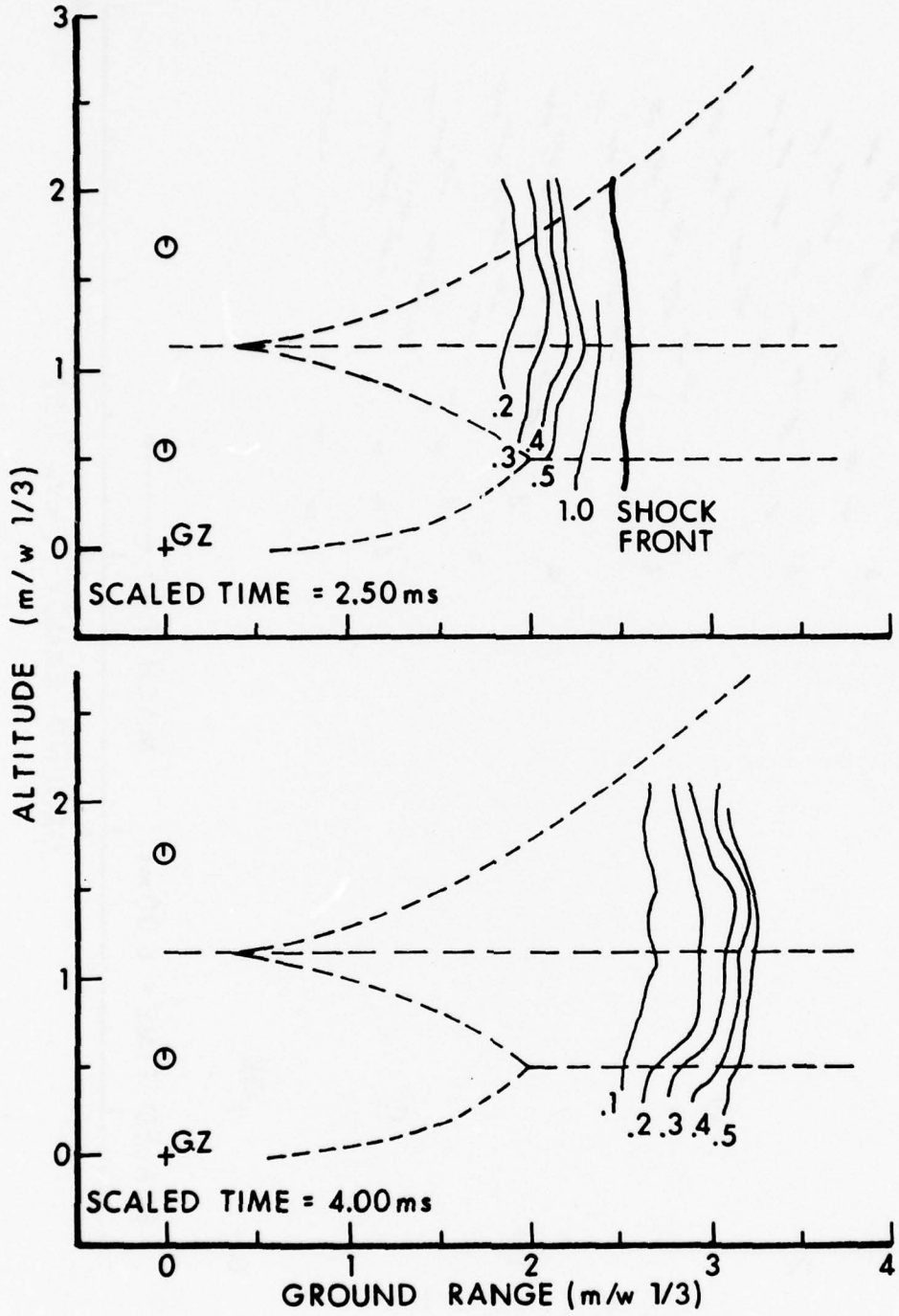

Figure 3.39. Equal Dynamic Pressure Contours at Scaled Times of 2.5 and 4.0 Milliseconds; Shot 10

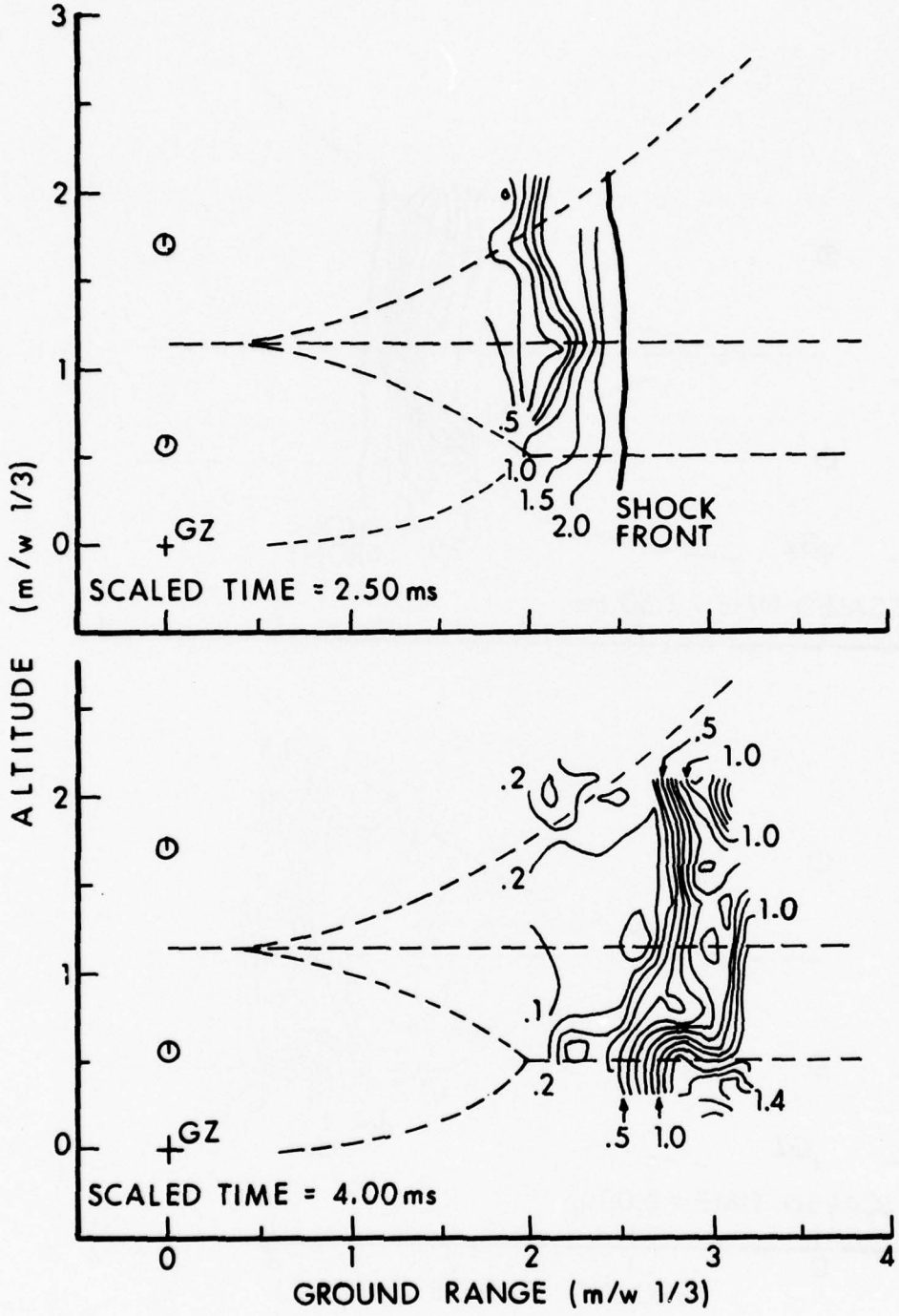

Figure 3.40. Equal Side-On Overpressure Contours at Scaled Times of 2.5 and 4.0 Milliseconds; Shot 10

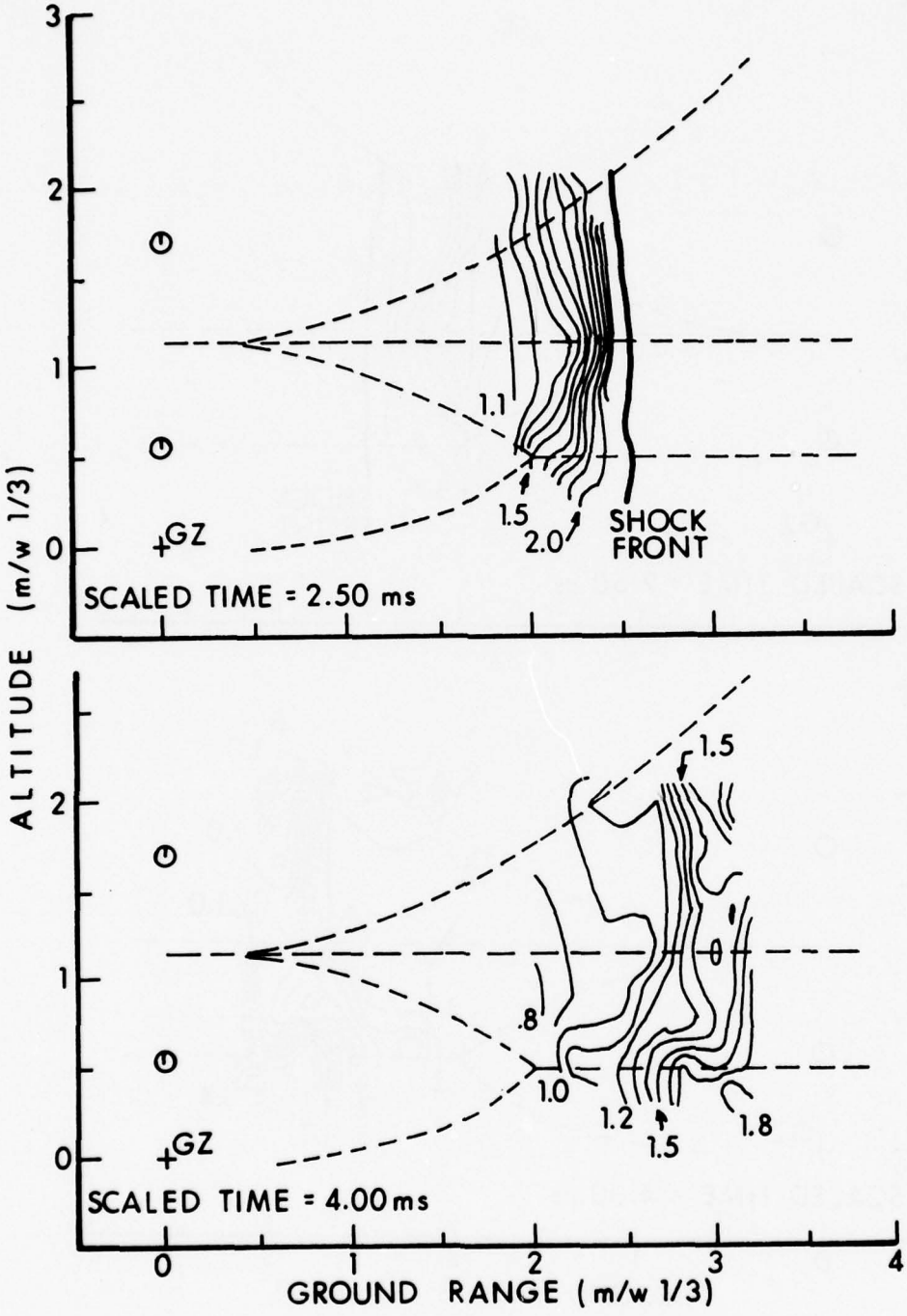

Figure 3.41. Equal Density Contours at Scaled Times of 2.5 and 4.0 Milliseconds; Shot 10

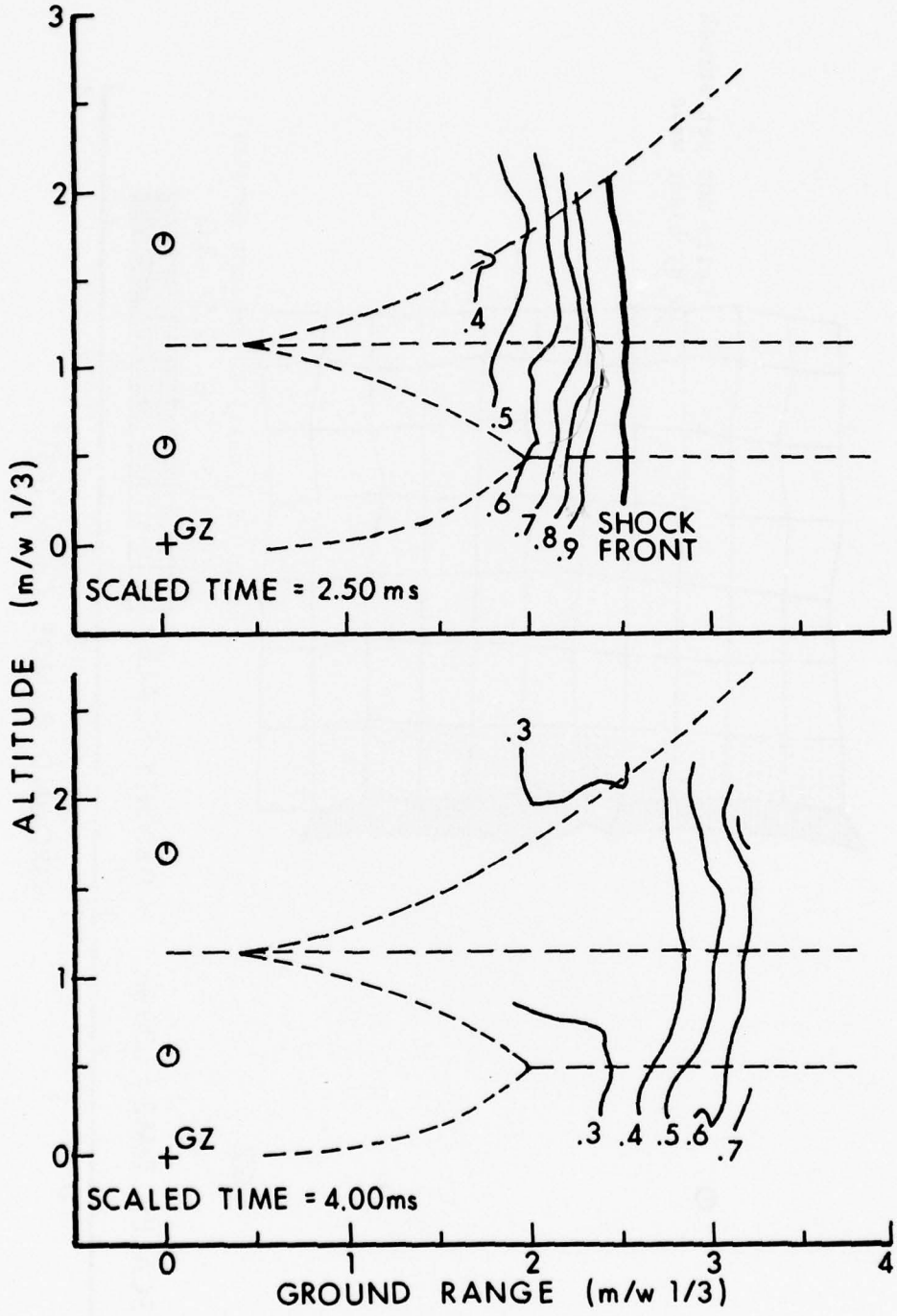

Figure 3.42. Equal Particle Velocity Contours at Scaled Times of 2.5 and 4.0 Milliseconds; Shot 10

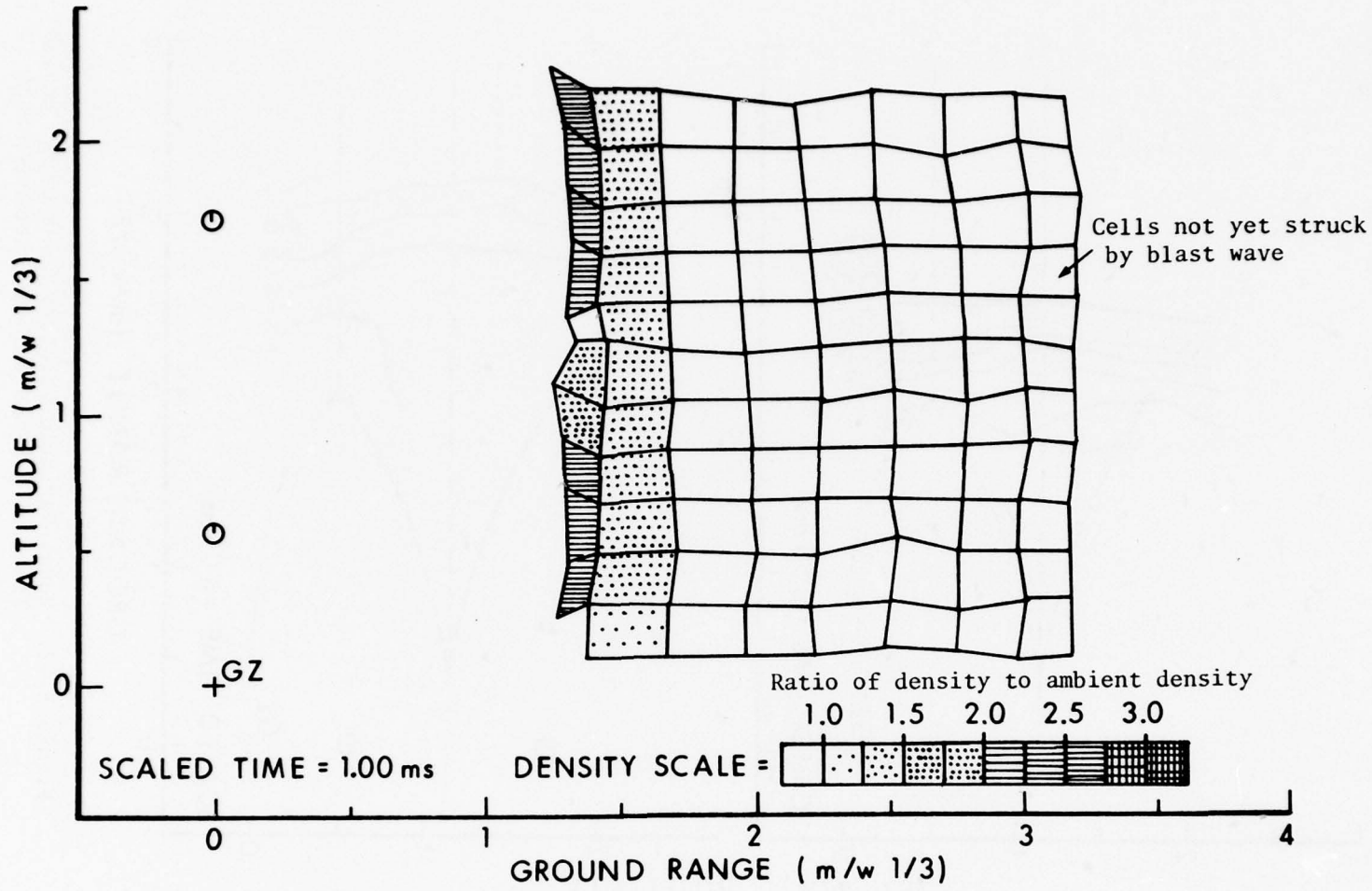

Figure 3.43. Density Field at Scaled Time 1 Millisecond After Detonation; Shot 10

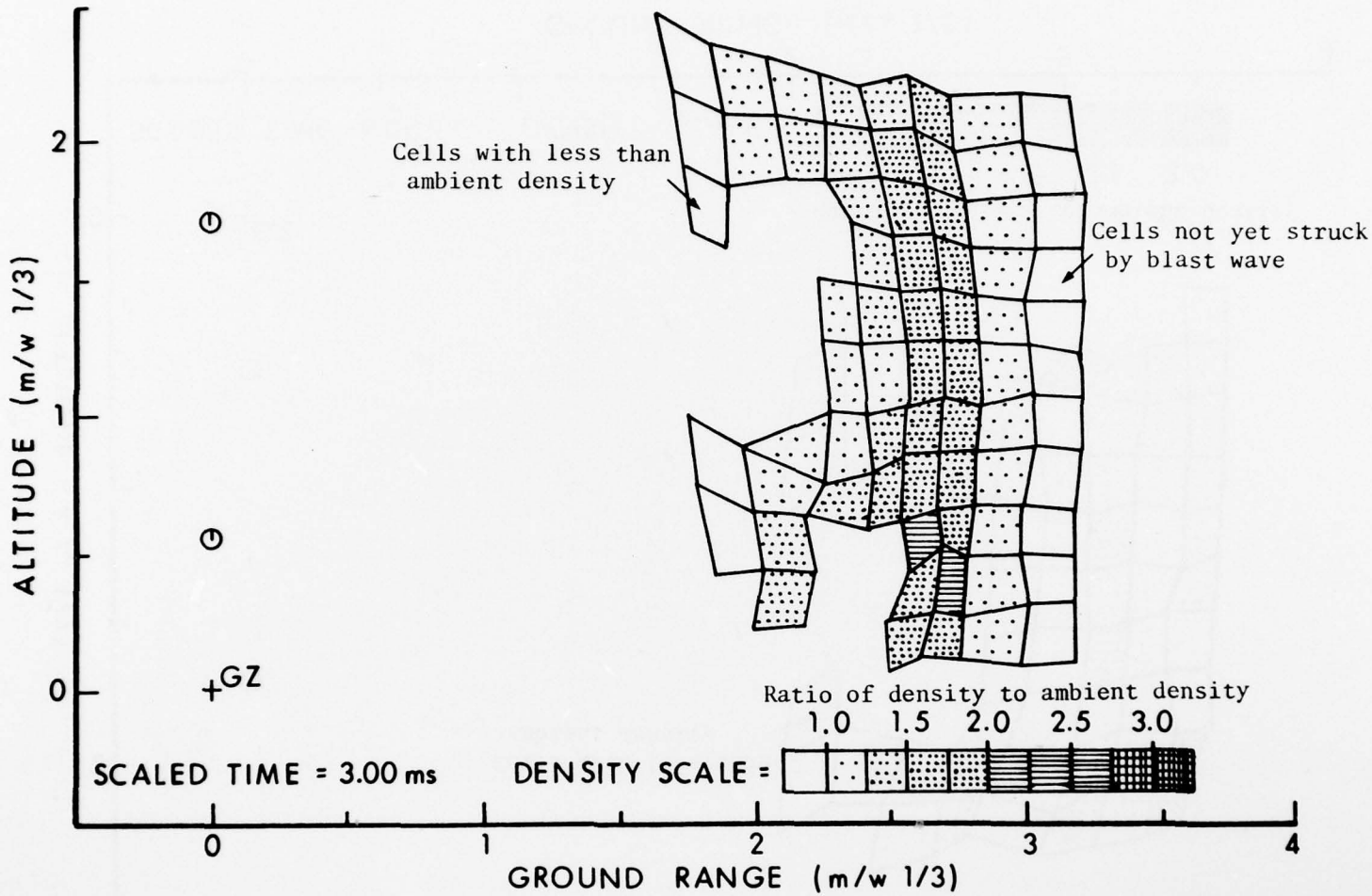

Figure 3.44. Density Field at Scaled Time 3 Milliseconds After Detonation; Shot 10

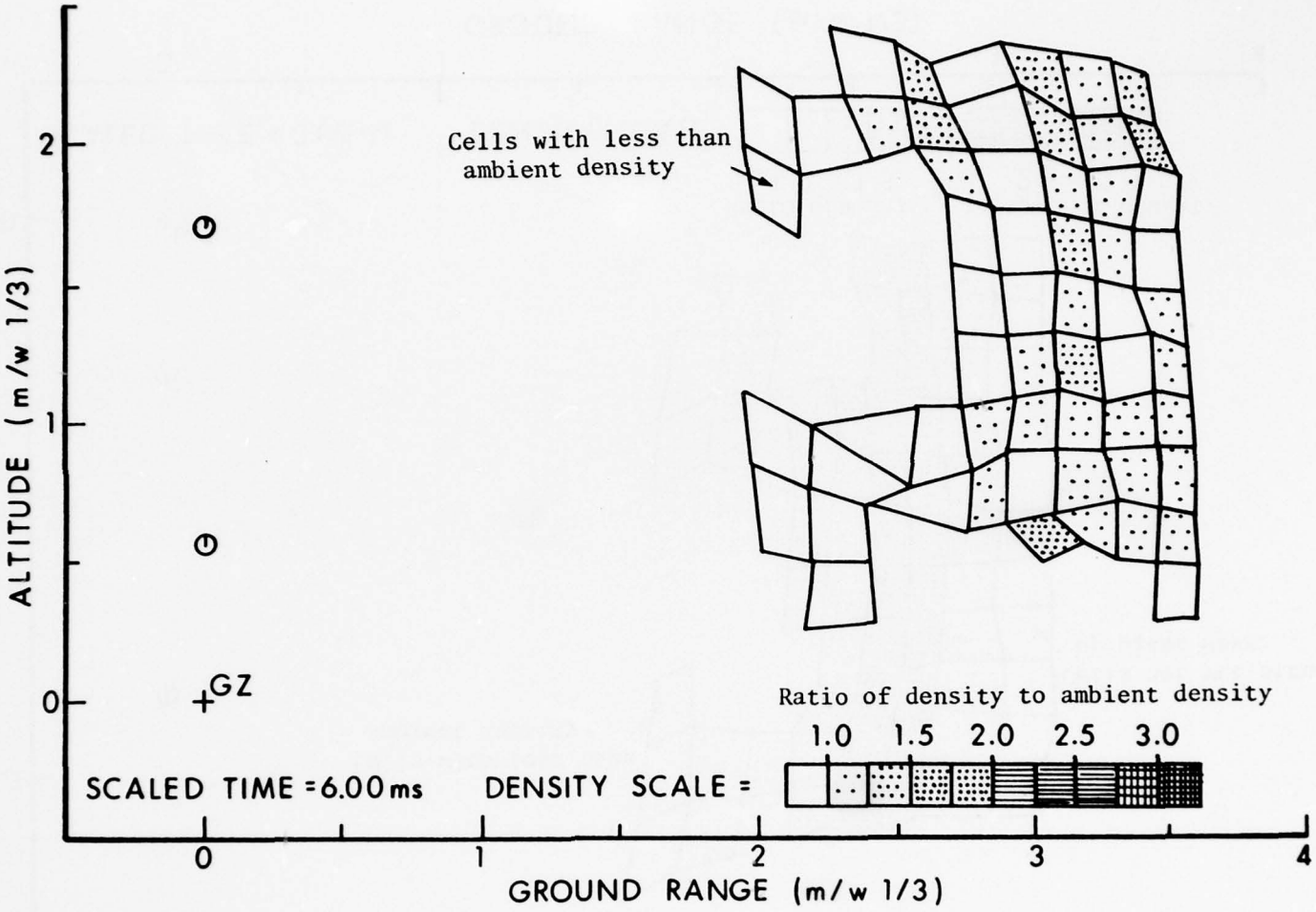

Figure 3.45. Density Field at Scaled Time 6 Milliseconds After Detonation; Shot 10

Additional study of this point, including measurements made with miniature gages in the region very close to the reflecting surface, is planned for the future.

The first group of illustrations from the photogrammetric particle trajectory analysis of Shot 10, Figures 3.36 through 3.38, shows velocity fields at scaled times of 1, 3, and 6 milliseconds after detonation. Scaling in all cases is to a one-kilogram charge weight and a standard atmosphere of dry air at 15°C at sea level. The second group, Figures 3.39 through 3.42, presents contours of equal dynamic pressures, side-on overpressures, densities, and particle velocities, respectively, associated with the blast waves at 2.5 and 4.0 milliseconds (scaled). Finally, the third group of illustrations, Figures 3.43 through 3.45, are density fields at scaled times after detonation of 1, 3, and 6 milliseconds.

The hydrostatic overpressures and dynamic pressures obtained from photogrammetric analysis of the particle trajectories can be used to compute total head pressures, after application of a compressibility correction. The technique is described in the Appendix of Reference 8, Volume III. It is essentially the inverse of the technique used to calculate dynamic pressures from the overpressure and total head gage records, discussed earlier in this section and described in Reference 6. When this is done, overpressure and total head pressure records obtained from analysis of the photographic data can be directly compared with those obtained from the electronic pressure gages. Corresponding impulse records can also be compared.

Examples of the comparisons at the 18.3-metre (60-foot) range for Shots 9 and 10 are given in Figures 3.46 through 3.49. In general, pressure and impulse curves obtained by the two totally different techniques are in excellent agreement. The good agreement is particularly gratifying in the case of the total pressure curves; this is apparently the first time that such a comparison has been possible. It is felt that this comparison validates both of the measurement techniques, as well as the analytic technique by which the photographic data were reduced. Similar comparisons for Shots 8 and 11 appear in Volumes III and IV of Reference 8.

3.7 Verification of Analytic Models

Because one of the major objectives of Phase II of the DIPOLE WEST series was verification of multiple-burst computer models, the hydrodynamic finite difference code HULL (Reference 10) was utilized by the Air Force Weapons Laboratory to obtain predictions for the airblast parameters. The results of these predictions, scaled to the one-kilogram charge at sea-level condition, are compared to corresponding experimental results, obtained from the electronic pressure transducer array, in Figures 3.50 through 3.55. Peak values of overpressure and overpressure-impulse from ground-level records for the two configurations

(Text continued on page 92.)

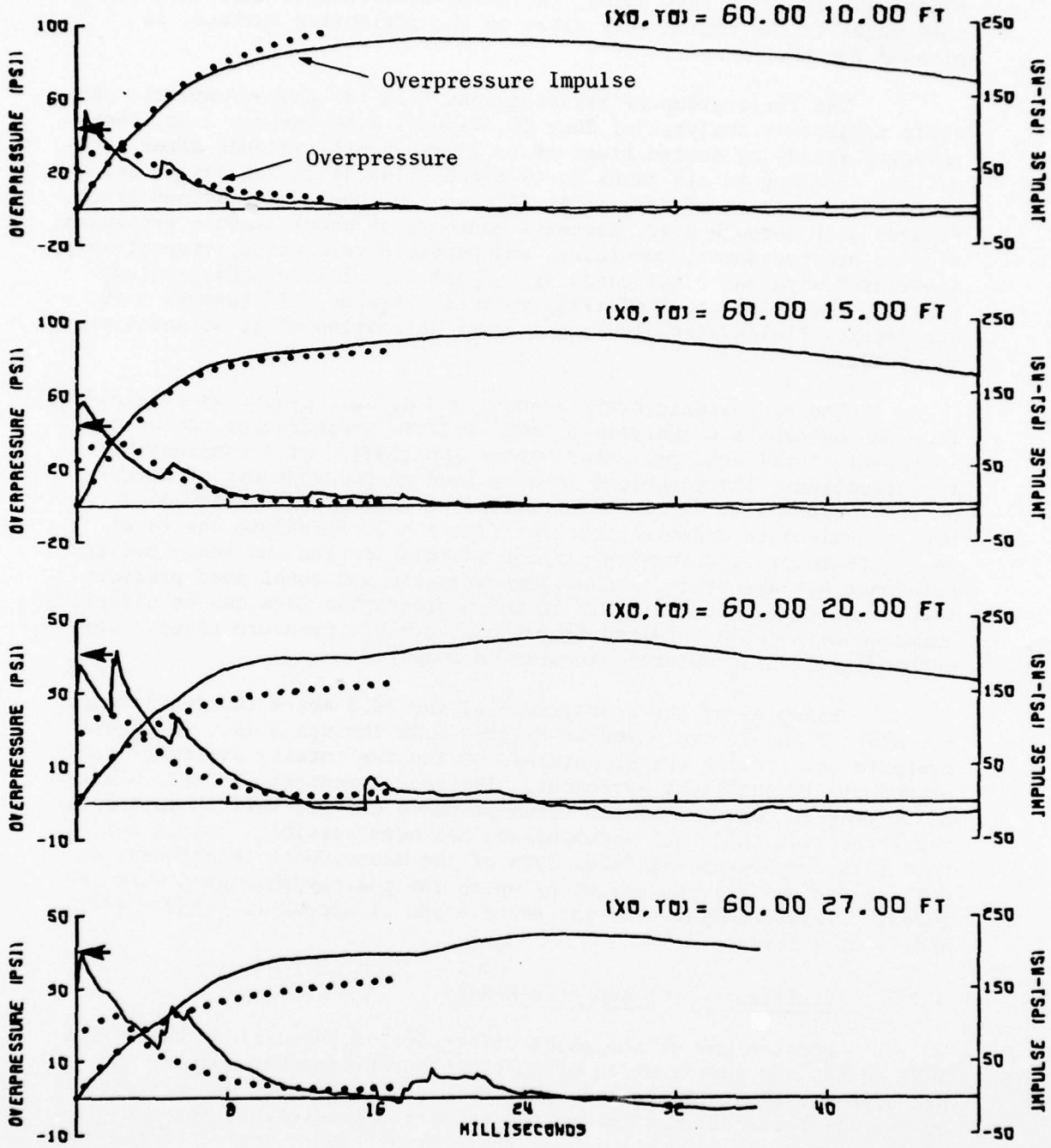

Figure 3.46(a). Comparison of Overpressures Obtained from Photogrammetric Analysis with Electronic Gage Results; Lower Stations, Shot 9

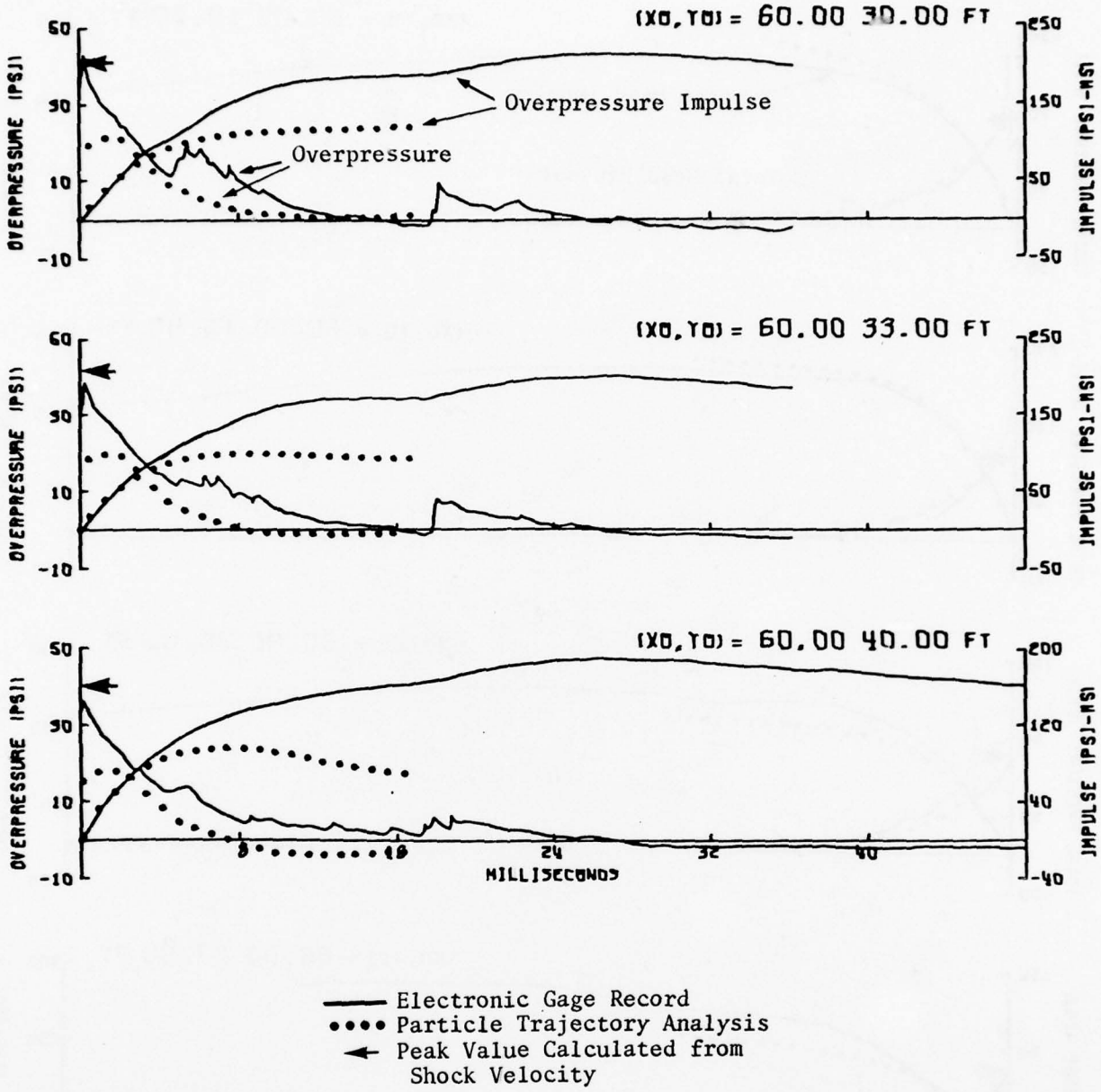

Figure 3.46(b). Comparison of Overpressures Obtained from Photogrammetric Analysis with Electronic Gage Results; Upper Stations, Shot 9

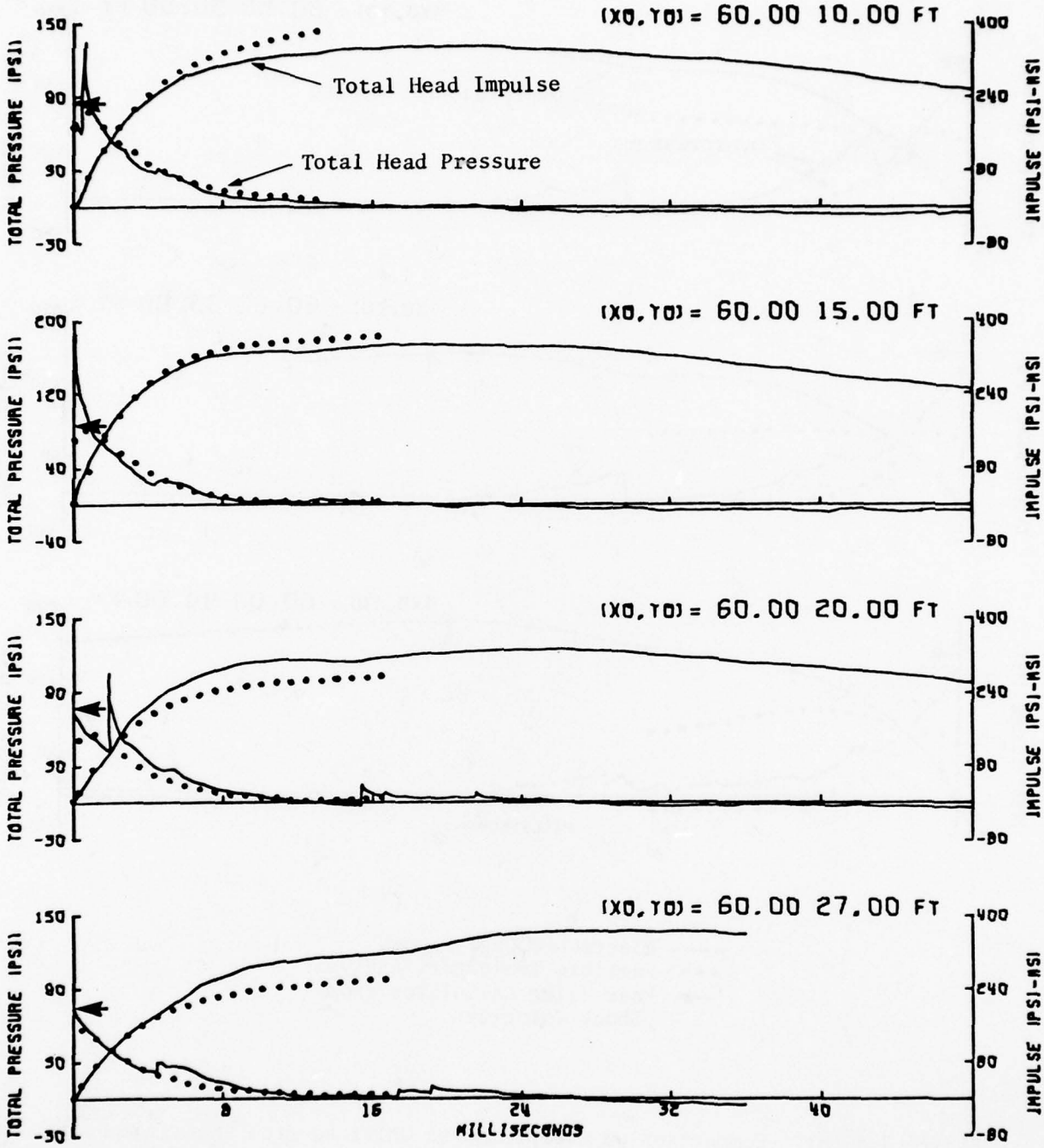

Figure 3.47(a). Comparison of Total Head Pressures Obtained from Photogrammetric Analysis with Electronic Gage Results; Lower Stations, Shot 9

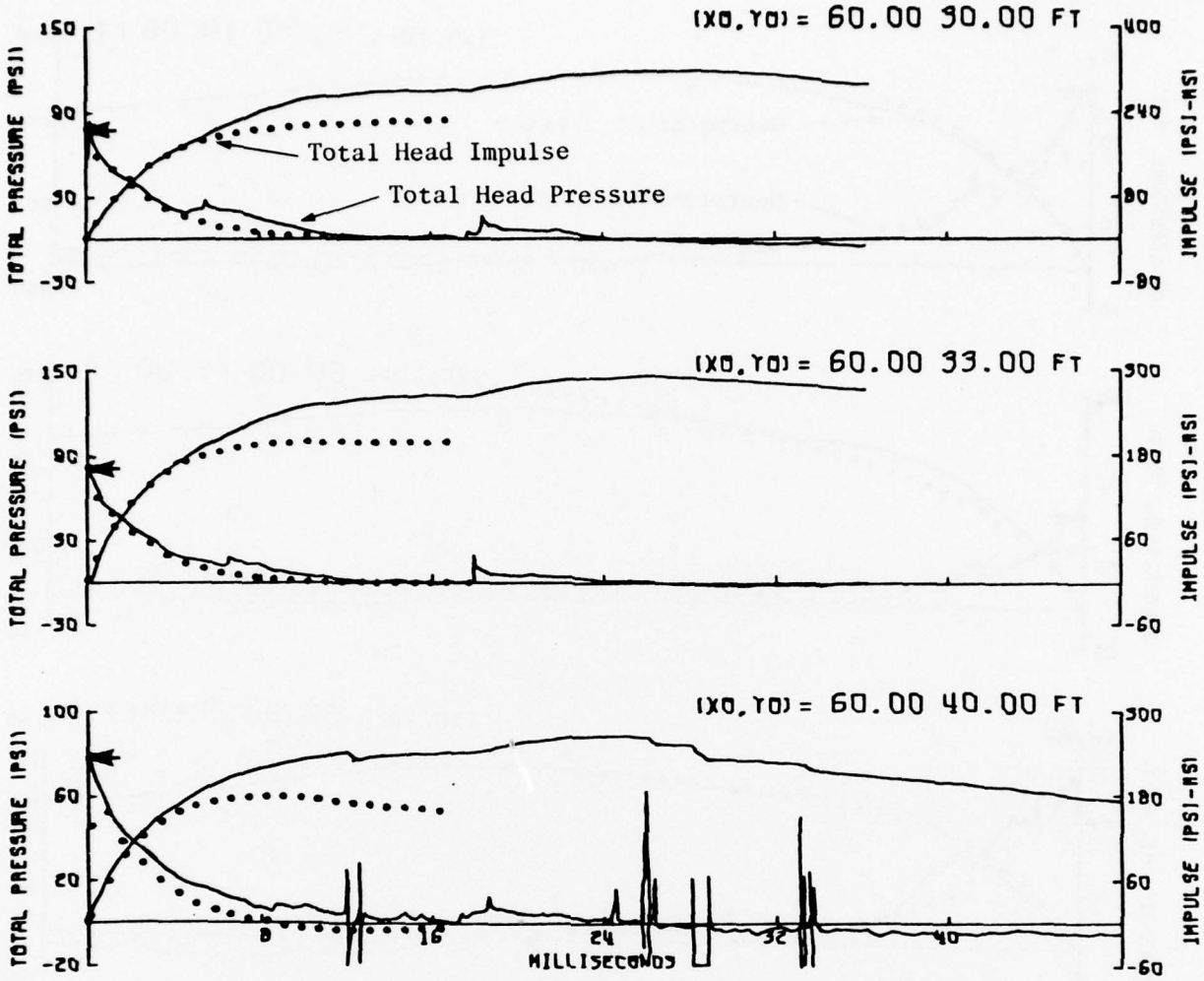

Figure 3.47(b). Comparison of Total Head Pressures Obtained from Photogrammetric Analysis with Electronic Gage Results; Upper Stations, Shot 9

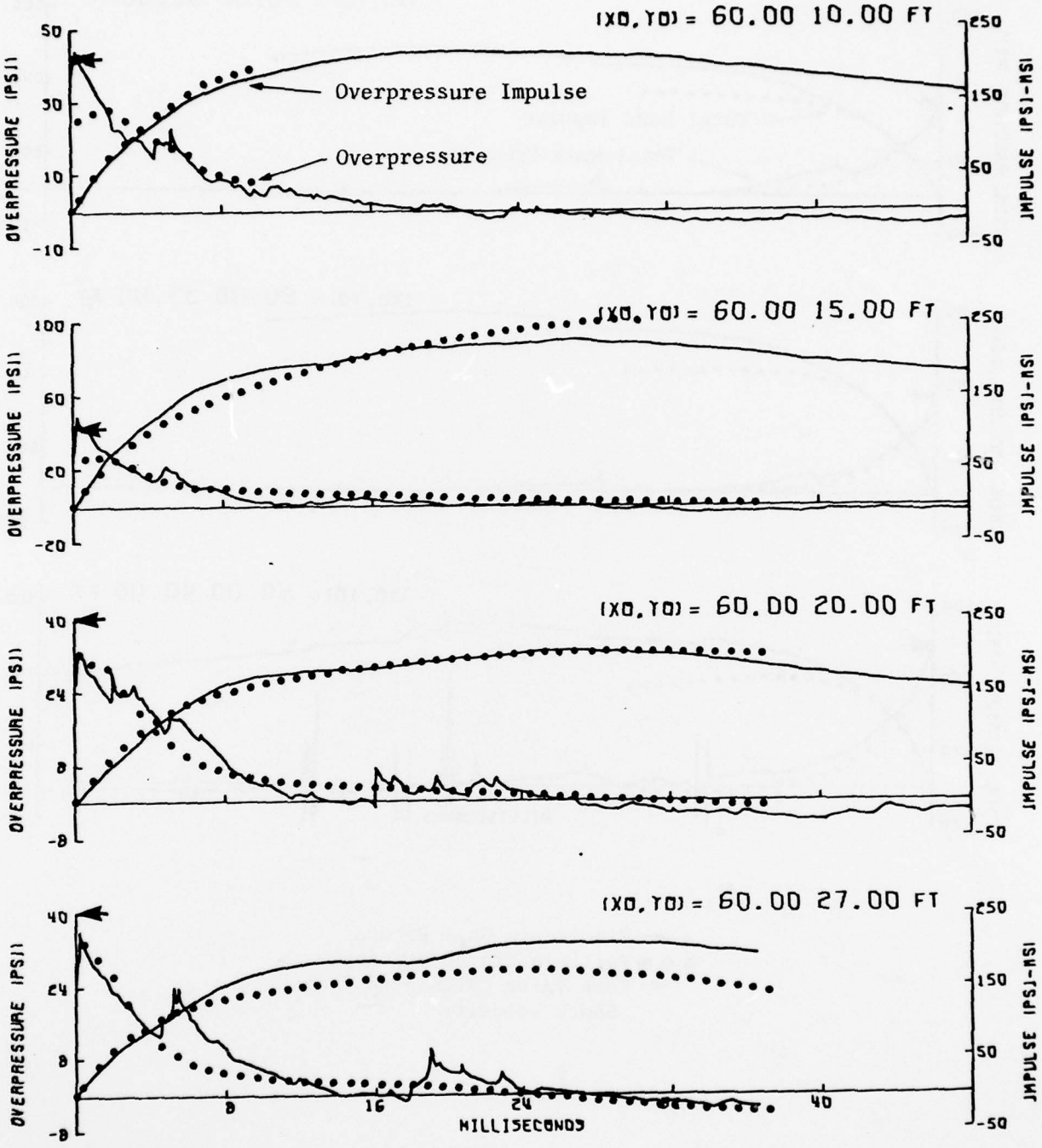

Figure 3.48(a). Comparison of Overpressures Obtained from Photogrammetric Analysis with Electronic Gage Results; Lower Stations, Shot 10

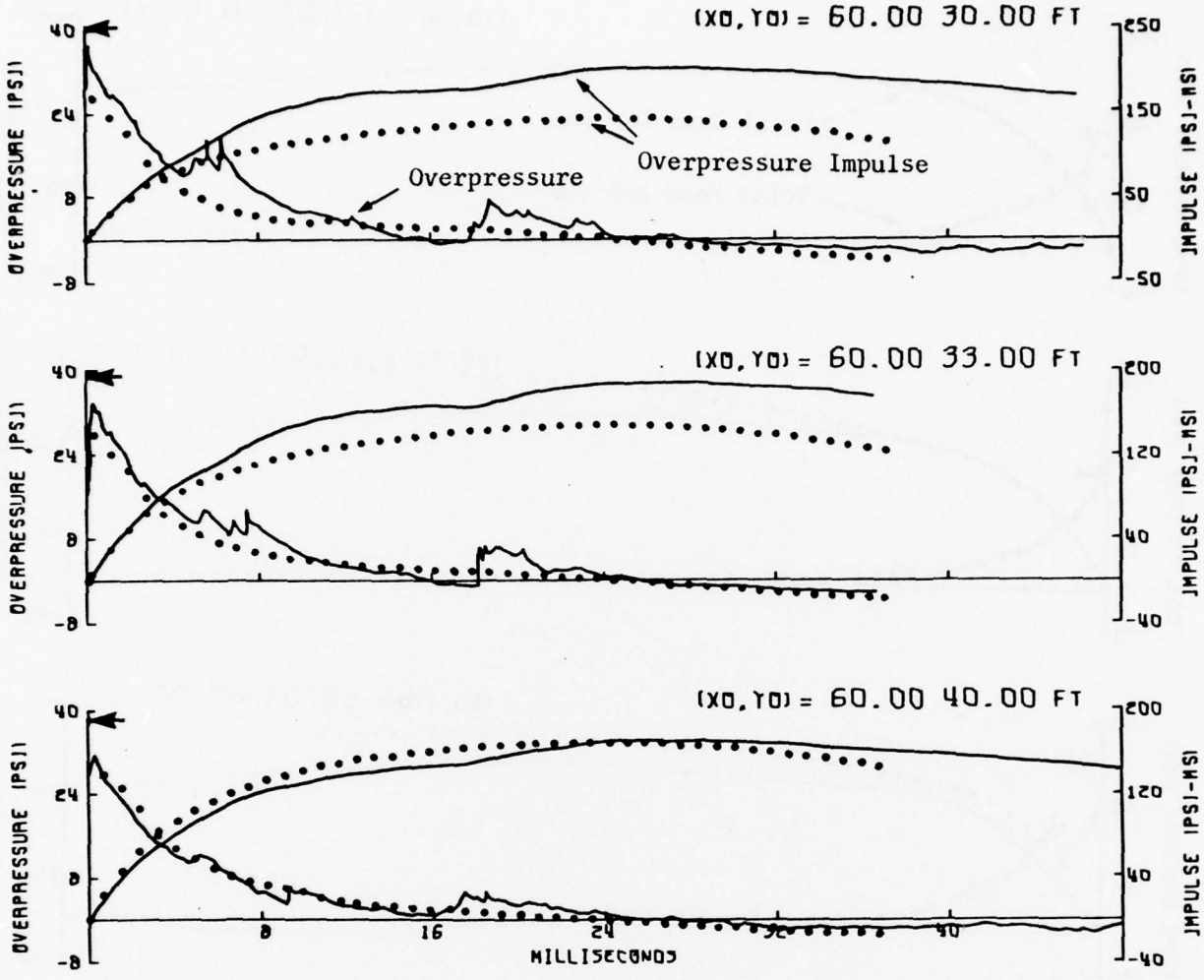

Electronic Gage Record
●●● Particle Trajectory Analysis
← Peak Value Calculated from Shock Velocity

Figure 3.48(b). Comparison of Overpressures Obtained from Photogrammetric Analysis with Electronic Gage Results; Upper Stations, Shot 10

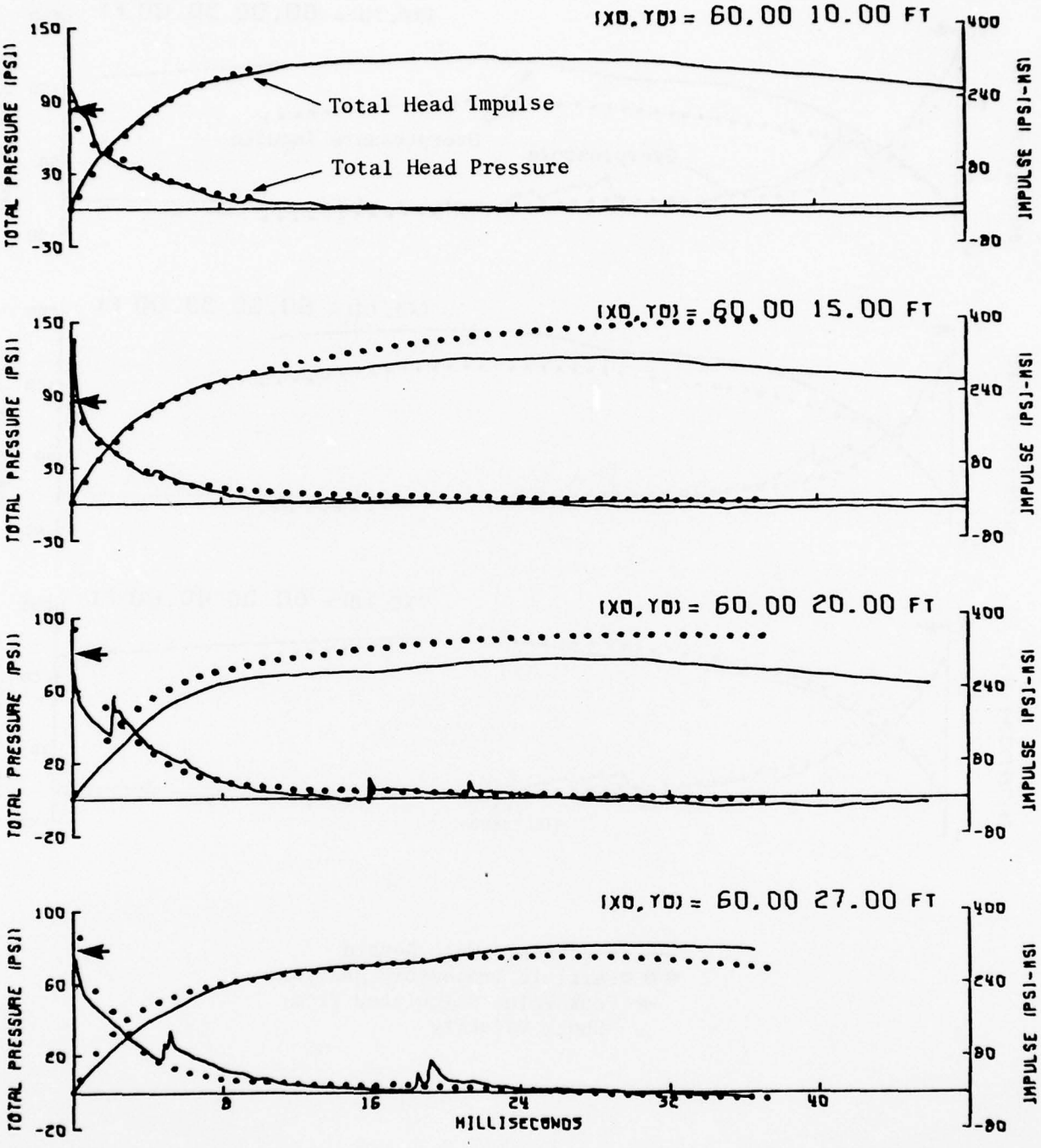

Figure 3.49(a). Comparison of Total Head Pressures Obtained from Photogrammetric Analysis with Electronic Gage Results; Lower Stations, Shot 10

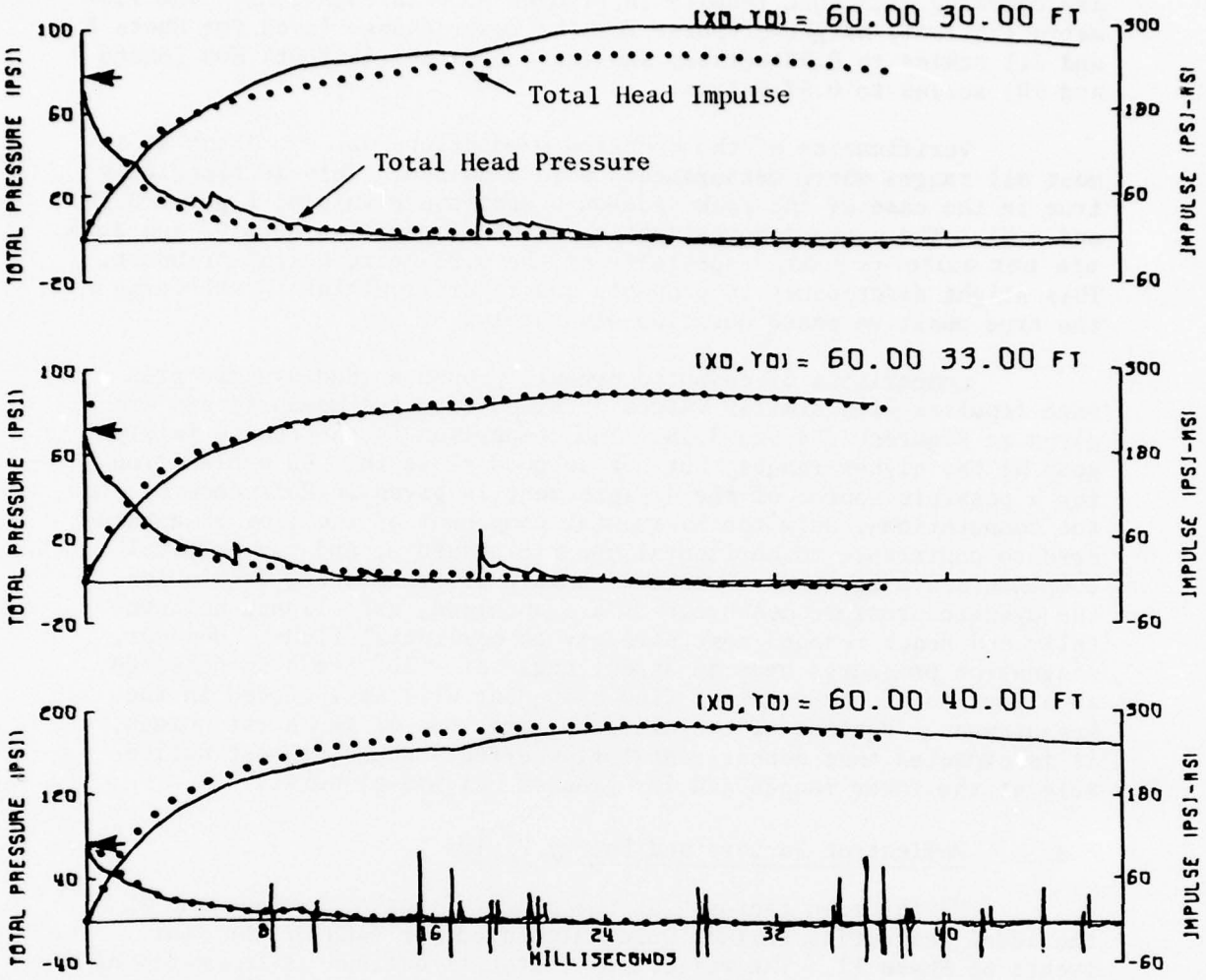

—— Electronic Gage Record
●●● Particle Trajectory Analysis
← Peak Value Calculated from Shock Velocity

Figure 3.49(b). Comparison of Total Head Pressures Obtained from Photogrammetric Analysis with Electronic Gage Results; Upper Stations, Shot 10

are compared with HULL results in Figures 3.50 through 3.53. The 7.6-metre (25-foot) height-of-burst for the lower charge (used for Shots 8 and 11) scales to 0.93 metres, and the 4.6-metre (15-foot) HOB (Shots 9 and 10) scales to 0.57 metres.

Verification of the computed predictions was excellent at almost all ranges where measurements were obtained. This is especially true in the case of the peak side-on overpressure values, Figures 3.50 and 3.51. The overpressure-impulse correlations, Figures 3.52 and 3.53, are not quite as good, especially at the 0.93-metre height-of-burst. This slight discrepancy is probably due to difficulties in selecting the true positive phase duration accurately.

Comparisons of computed dynamic pressures and dynamic pressure impulses with similar values obtained from the measurements are given in Figures 3.54 and 3.55. The comparison is seen to be fairly good at the higher ranges, but not so good close-in. An explanation for a possible source of the disagreement is given in Reference 6. In the computations, only the horizontal component of the flow is considered to contribute to horizontal dynamic pressure, and any vertical components are ignored. The total head pressure probes, from which the dynamic pressure measurements are obtained, are aligned horizontally and hence respond most strongly to horizontal flows. However, stagnation pressures over an aspect angle of $\pm 30^{\circ}$ are also detected, so a portion of any vertical flow component will be included in the measurement. Because of the elevated locations of the burst points, it is expected that nonhorizontal flow effects would be most noticeable at the lower ranges and for greater heights-of-burst.

3.8 Reflection Factors and Energy Fields

"Reflection factors" at the real reflecting surface and at the ideal reflecting surface were calculated for each of the four events of Phase II. The reflection factor is defined as the ratio of peak overpressure of the incident shock wave, P_I , to peak overpressure of the reflected wave, P_R . It thus serves as a measure of the enhancement of the pulse as it is reflected at a surface.

Values of P_I used in determination of the reflection factors were taken from the "free air" overpressure curve. This curve has been compiled over a number of years at BRL using data from a number of test events. The free air curve gives peak overpressure to be expected at a specified distance from a 454-kilogram (1000-pound) TNT detonation in the absence of any surface interactions. The charge-weight differences are accounted for by scaling, and the difference between TNT and pentolite is neglected.

Note that, as pointed out in Section 3.3, the double-charge system of Shots 8 and 11 acts like a 490-kilogram (1080-pound) charge

(Text continues on page 99.)

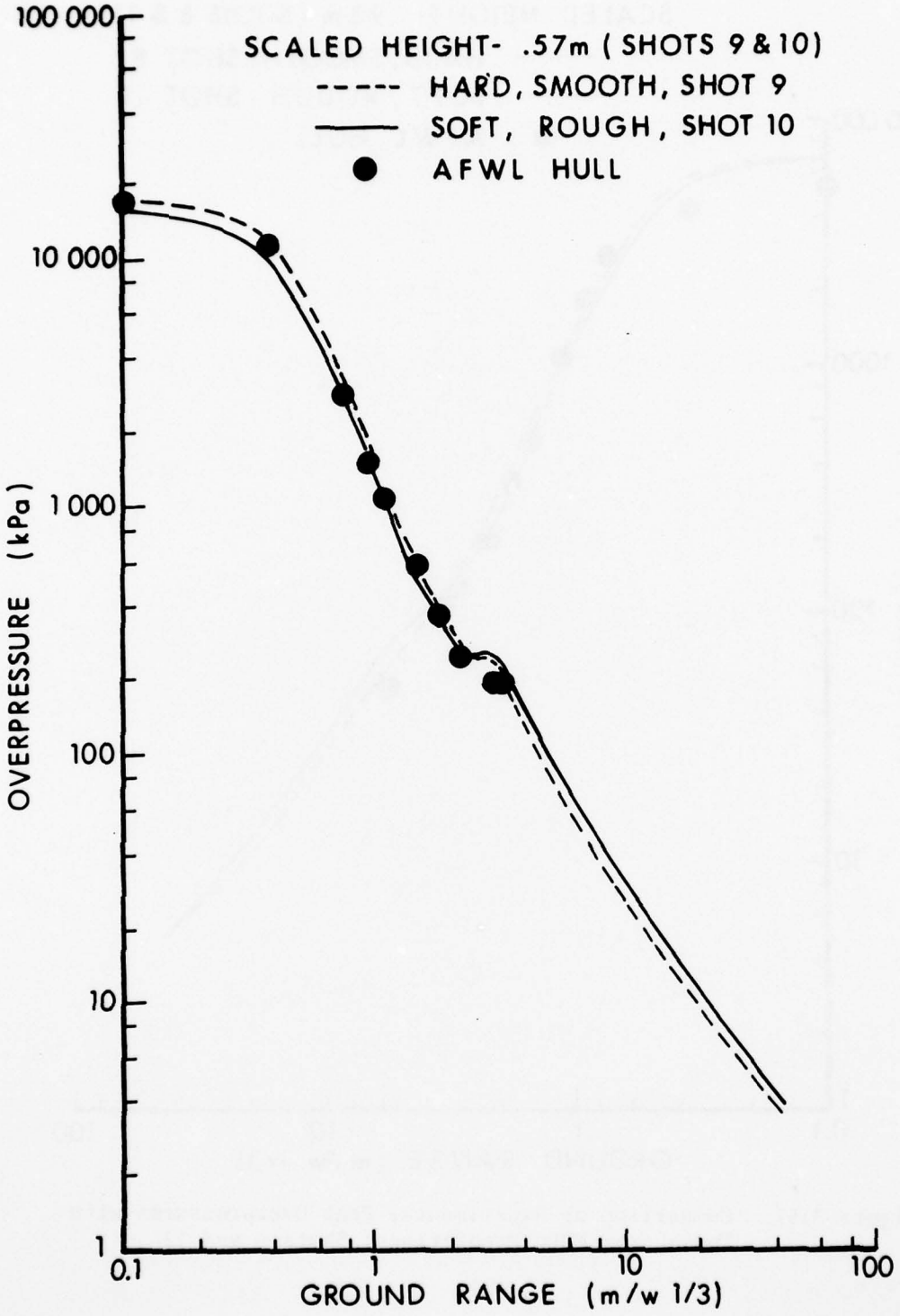

Figure 3.50. Comparison of Experimental Peak Overpressures with Those from HULL Predictions; Shots 9 and 10

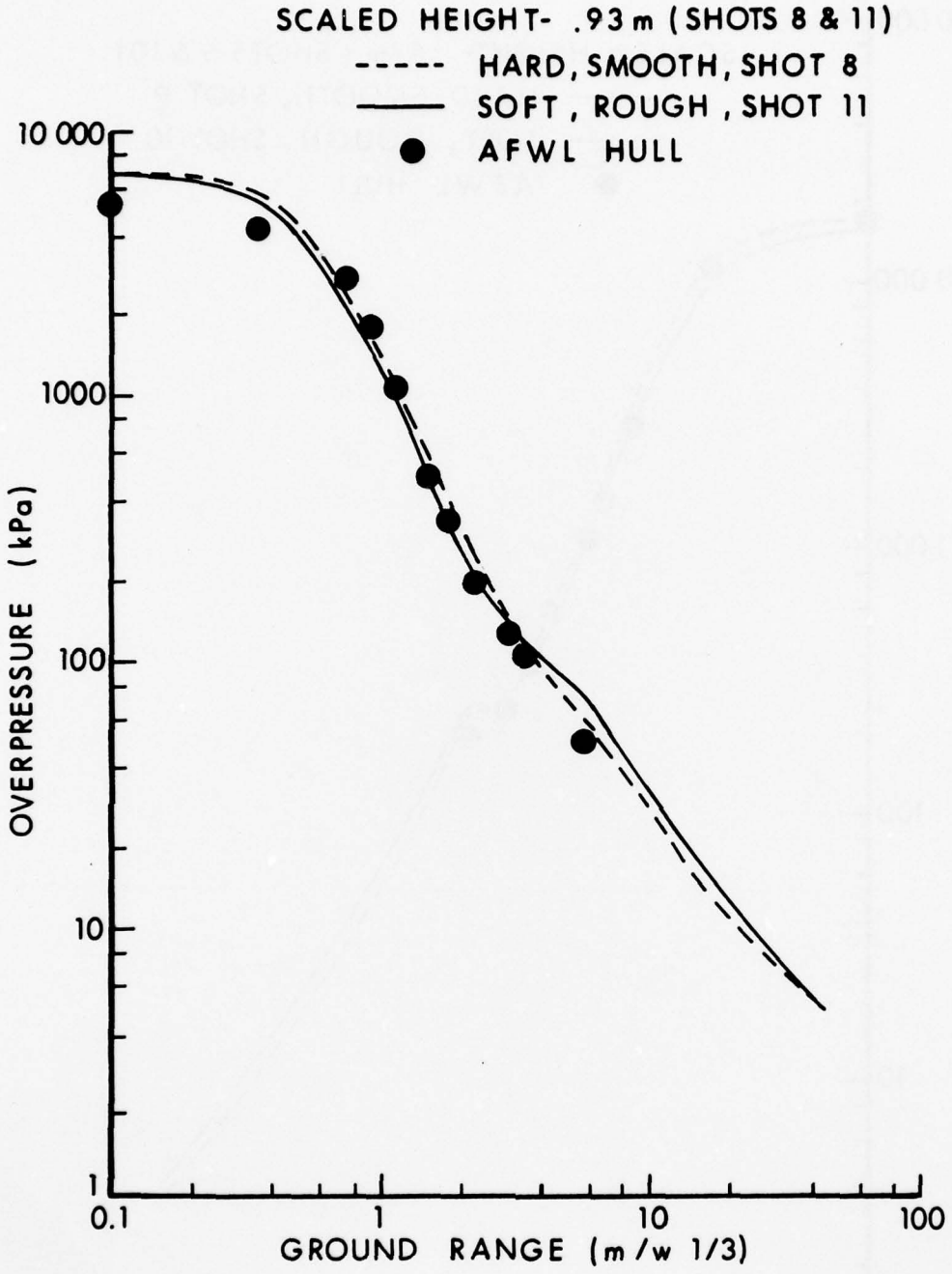

Figure 3.51. Comparison of Experimental Peak Overpressures with Those from HULL Predictions; Shots 8 and 11

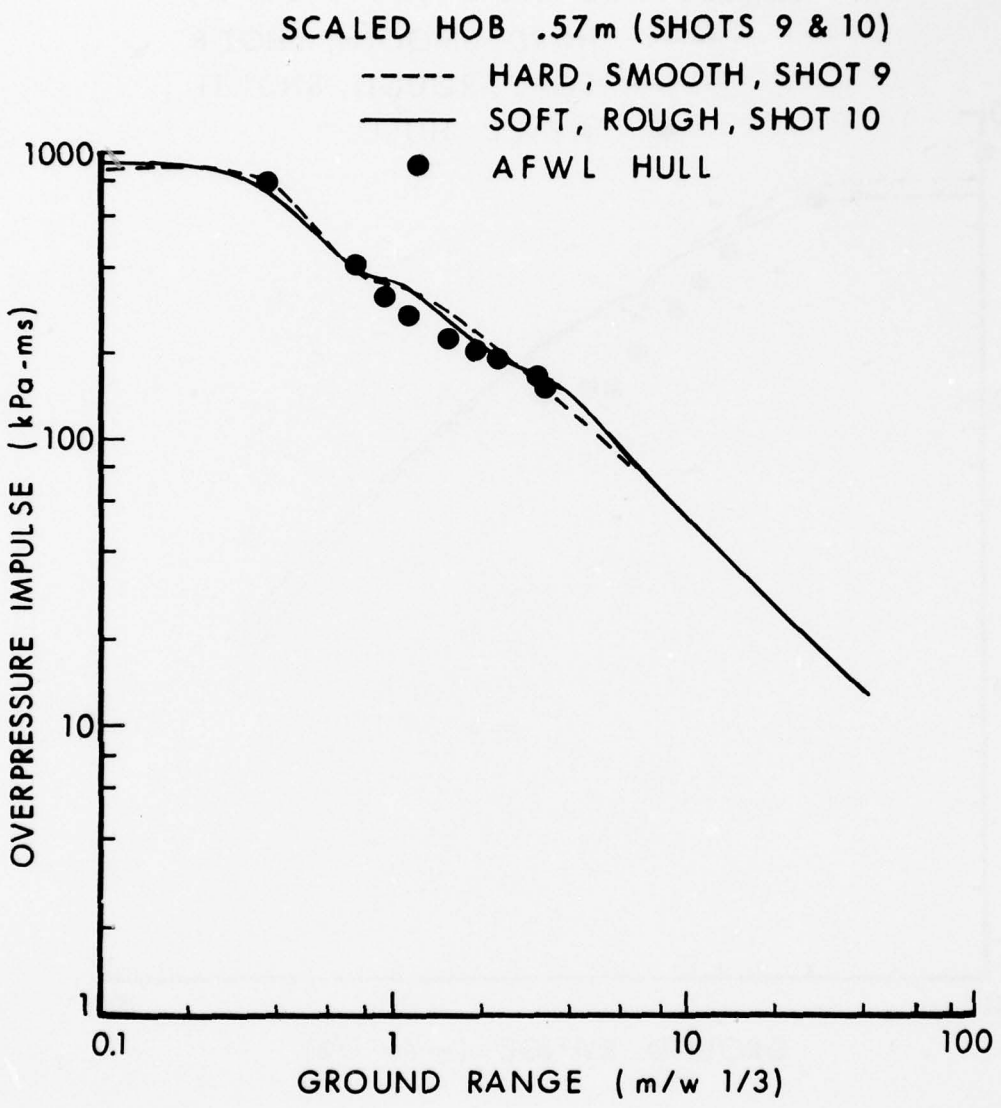

Figure 3.52. Comparison of Experimental Peak Overpressure-Impulses with Those from HULL Predictions; Shots 9 and 10

AD-A068 462 GENERAL ELECTRIC CO ALBUQUERQUE N MEX TEMPO F/G 19/4
HIGH EXPLOSIVE MULTIBURST AIRBLAST PHENOMENA (SIMULTANEOUS AND --ETC(U)
FEB 79 R E REISLER, L W KENNEDY, J H KEEFER DNA001-77-C-0305
UNCLASSIFIED ARBRL-TR-02142 NL

2 OF 2
AD
A068462

END
DATE
FILMED
6 -79
DDC

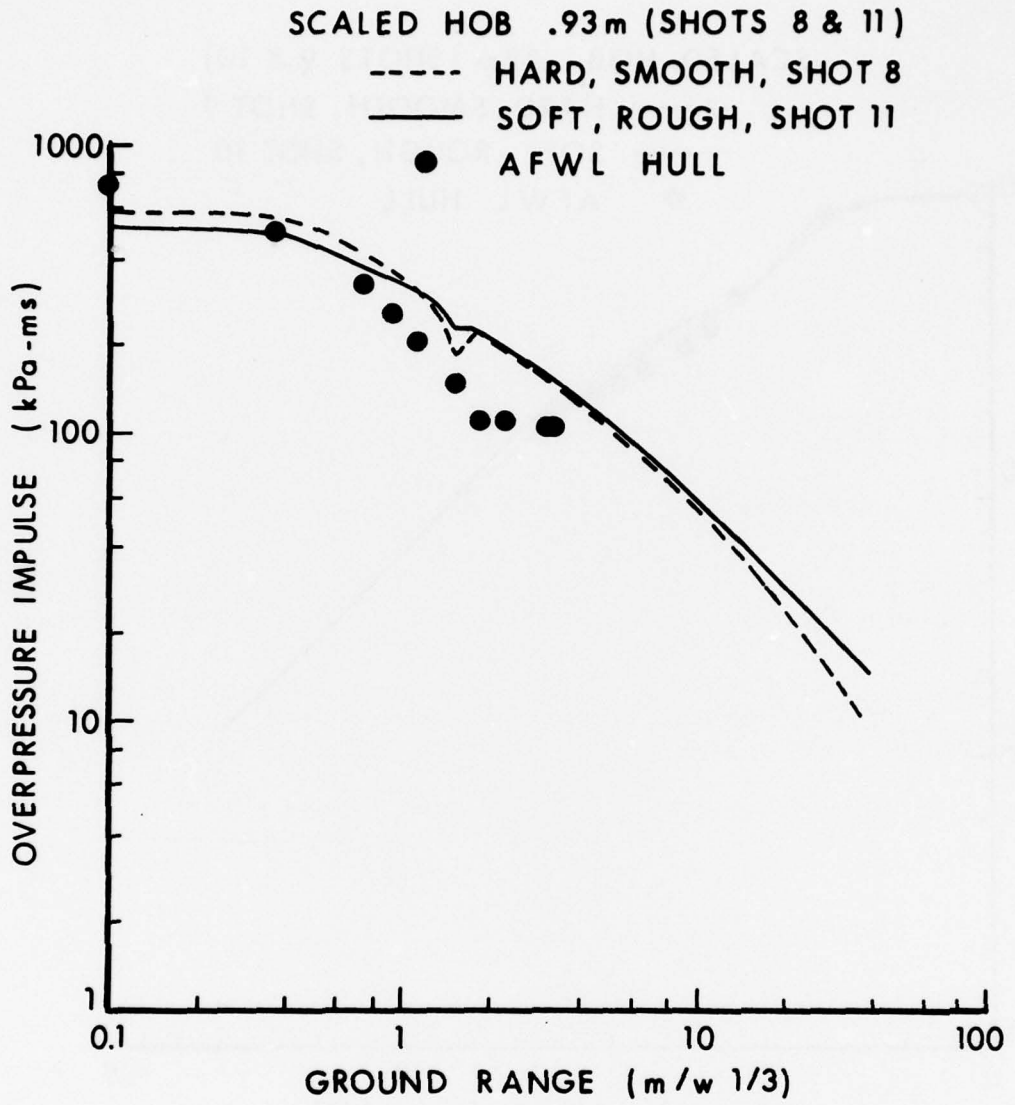

Figure 3.53. Comparison of Experimental Peak Overpressure-Impulses with Those from HULL Predictions; Shots 8 and 11

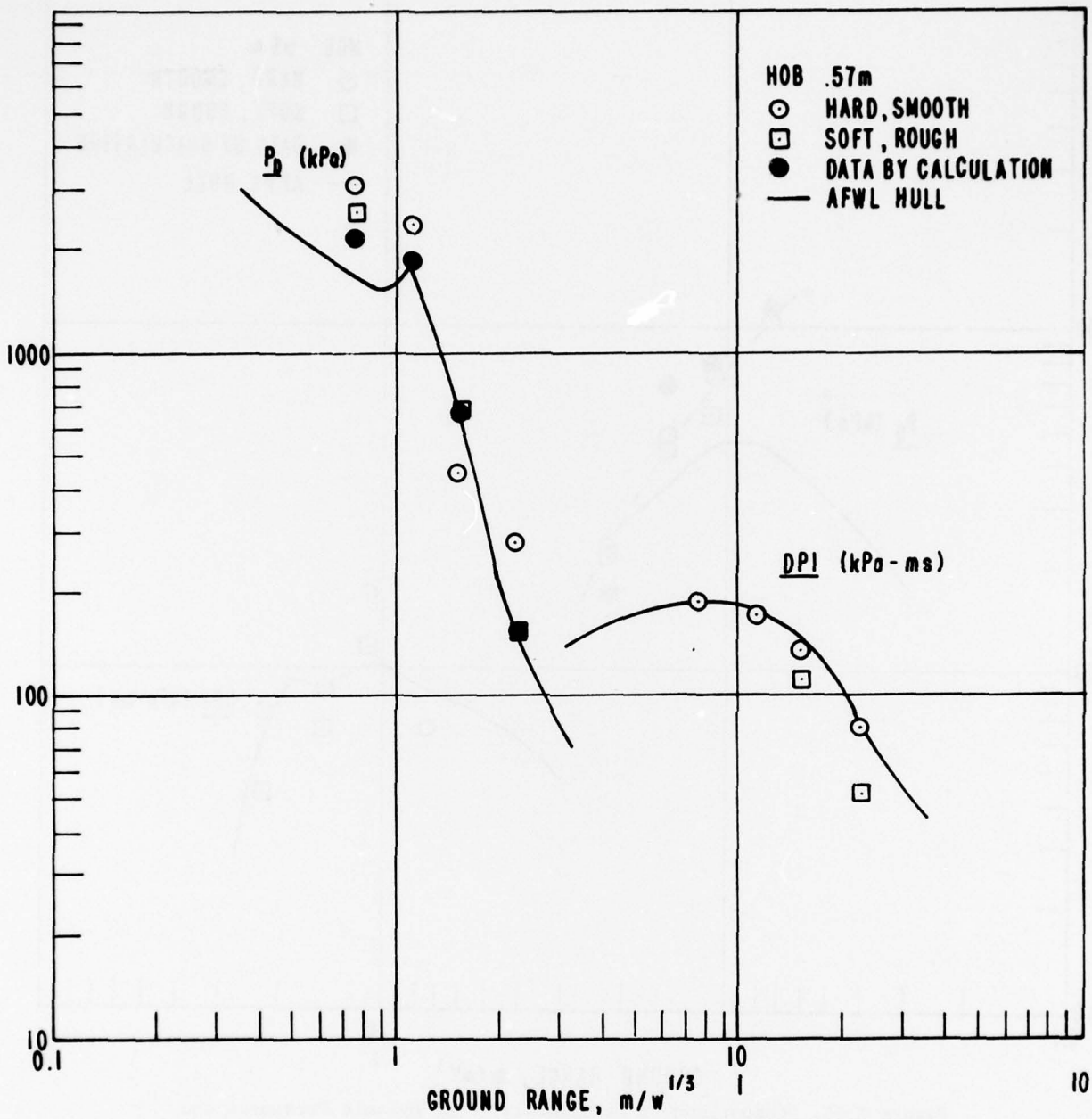

Figure 3.54. Comparison of Experimental Peak Dynamic Pressures and Dynamic Pressure Impulses with Those from HULL Predictions; Shots 9 and 10

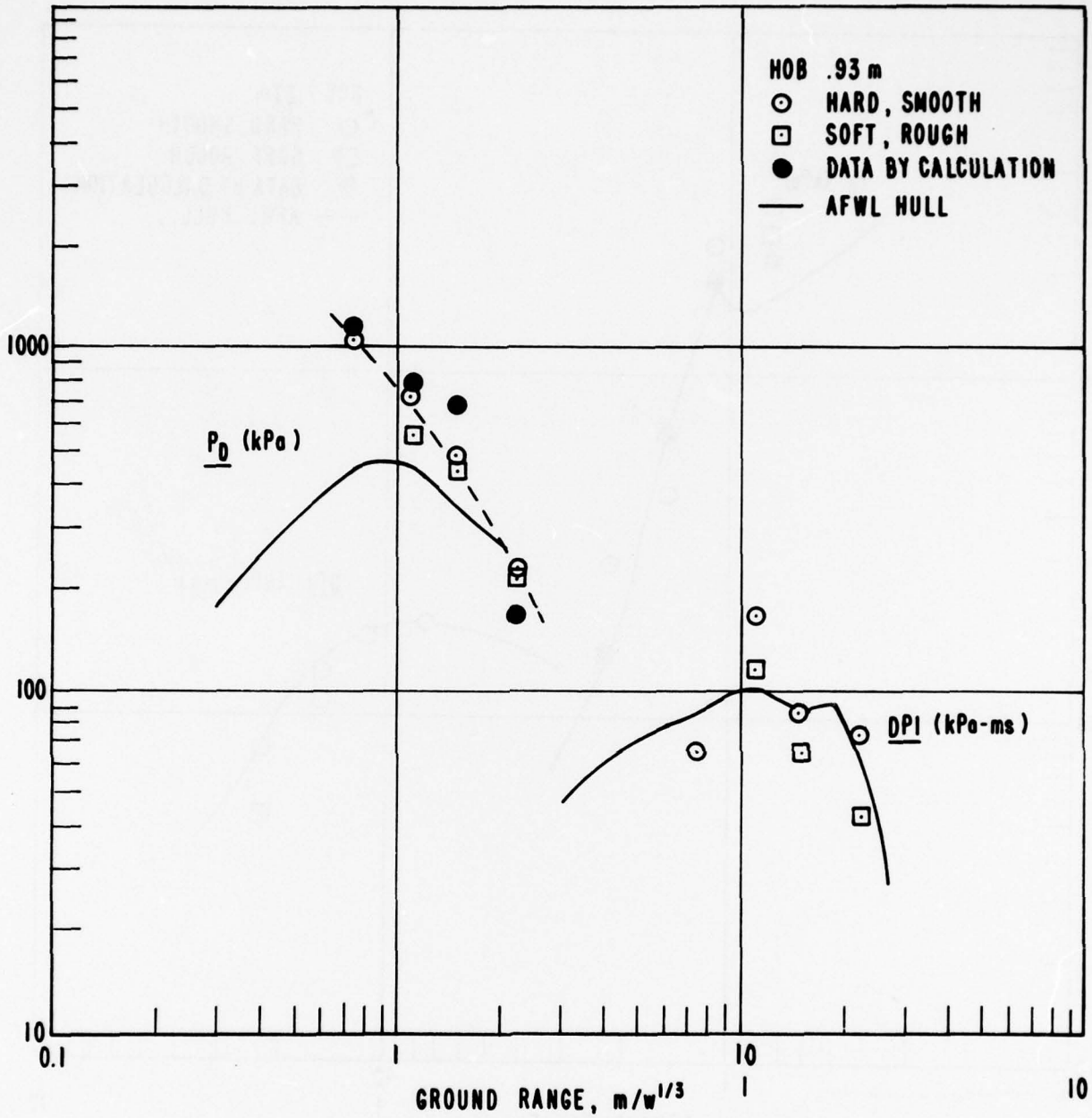

Figure 3.55. Comparison of Experimental Peak Dynamic Pressures and Dynamic Pressure Impulses with Those from HULL Predictions; Shots 8 and 11

out to the 100-kilopascal (15-psi) level, and like a 980-kilogram (2160-pound) charge thereafter. For Shots 9 and 10, the transition occurs at about 200 kilopascals (30 psi).

Values of P_R were taken from the electronic transducer measurements at the ground surface and as near as possible to the ideal reflecting surface. Values of P_I and P_R, and the resulting reflection factors, are tabulated in Table 3.1.

Reflection factors from the table have been plotted as functions of ground range in Figure 3.56. No clear trends are evident from the plots beyond the fact that the ideal-surface reflection factors seem to be lower than those from the real surface at the 6.1-metre (20-foot) range, and higher or about the same as those from the real surface at other ranges.

A source of error in the values of P_R obtained at the ideal reflecting surface, and hence also in the reflection factors, arises because of the operational difficulty of securing the charges at the exact heights specified. Because of this, the ideal reflecting plane did not occur at exactly the planned height, where the transducers were located. Because for off-plane measurements the incident and reflected pulses are separated in time rather than being superimposed at their maximum values, rapid attenuation of measured pulse amplitude is expected as the measurement location moves away from the plane. No attempt has been made to correct the ideal-surface values of P_R for this error.

Energy fields, that is, the available energy per unit volume at any point in the blast wave fields, can be computed from the information previously obtained from photogrammetric analysis of the photographic data. This has been undertaken for Shot 11, and the results appear in Reference 13.

The available energy per unit volume at a point in the blast wave is computed from known data using the equation:

$$E = \frac{1}{\gamma - 1} (P - P_a) + \frac{1}{2} \rho u^2$$

where γ is the ratio of specific heats, P is hydrostatic pressure in the gas element at the point, and P_a is the ambient pressure in

---

13. *J. M. Dewey and D. J. McMillin, "Energy Density Calculations: DIPOLE WEST Shot 11," University of Victoria, Victoria, B. C., Canada, to be published by USA Ballistic Research Laboratory, Aberdeen Proving Ground, Maryland 21005, 1978.*

Table 3.1. Reflection Factors at Real and Ideal Reflecting Surfaces

Shot	Ground Range (m)	Ground Range (ft)	Slant Range (m)	Slant Range (ft)	Ideal Surface P_R (kPa)	Ideal Surface P_I (kPa)	Ideal Surface P_R/P_I	Real Surface P_R (kPa)	Real Surface P_I (kPa)	Real Surface P_R/P_I
8	6.10	20	9.69	31.8	1600	538	2.97	2220	538	4.13
	9.14	30	11.84	38.9	1062	352	3.02	1089	352	3.09
	12.19	40	14.33	47.0	517	228	2.27	483	228	2.12
	18.29	60	19.78	64.9	276	117	2.36	217	117	1.86
11	6.10	20	9.65	31.7	1724	552	3.12	2137	510	4.19
	9.14	30	11.81	38.7	979	359	2.73	1034	341	3.03
	12.19	40	14.30	46.9	503	231	2.18	414	221	1.87
	18.29	60	19.76	64.8	276	117	2.36	207	114	1.82
9	6.10	20	7.65	25.1	3034	883	3.44	3613	896	4.03
	9.14	30	10.24	33.6	1172	472	2.48	1062	472	2.25
	12.19	40	13.04	42.8	752	296	2.54	545	296	1.84
	18.29	60	18.86	61.9	276	131	2.11	245	131	1.87
10	6.10	20	7.65	25.1	2344	931	2.52	3461	924	3.75
	9.14	30	10.24	33.6	1145	472	2.43	1020	472	2.16
	12.19	40	13.03	42.8	662	296	2.24	465	296	1.57
	18.29	60	18.86	61.9	248	131	1.89	234	131	1.79

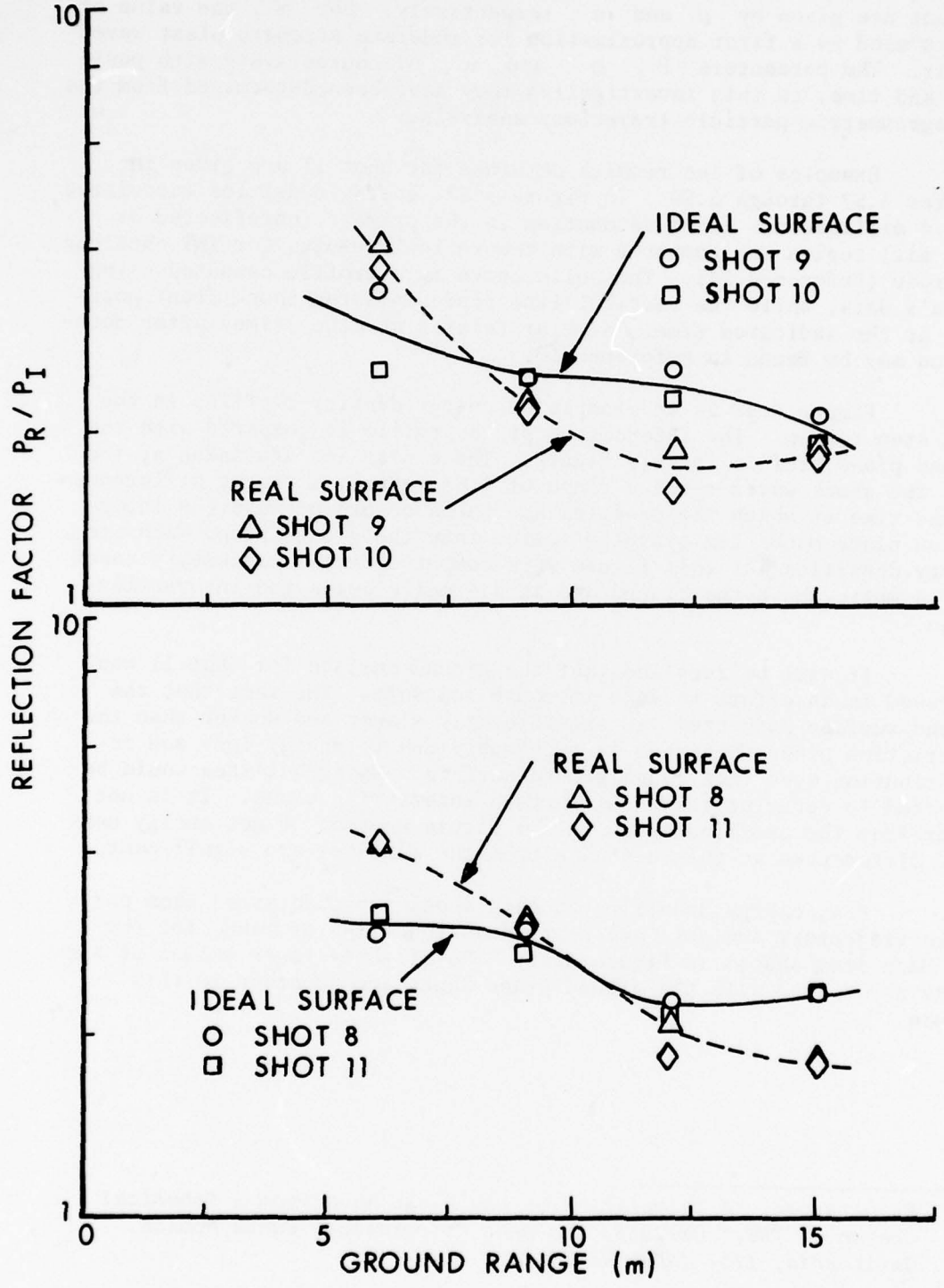

Figure 3.56. Reflection Factors as Functions of Ground Range for All Events of Phase II

the gas before arrival of the blast. Density and velocity of the gas element are given by ρ and u, respectively. For γ, the value of 1.4 is used as a first approximation for moderate strength blast waves in air. The parameters P, ρ, and u, of course, vary with position and time; in this investigation they have been determined from the photogrammetric particle trajectory analysis.

Examples of the results obtained for Shot 11 are given in Figures 3.57 through 3.59. In Figure 3.57, energy densities calculated at 1.4 milliseconds after detonation in the primary (unreflected or free air) region are compared with theoretical results for TNT obtained by Brode (Reference 14). The solid curve is a profile computed using Brode's data, while the vertical line represents the shock front position at the indicated time. Similar results at other times after detonation may be found in Reference 13.

Figure 3.58 is an example of energy density profiles in the Mach stem region. The interaction plane profile is compared with the ground plane profile in this figure. These profiles are taken at the time the shock waves reach a range of 4.83 metres; a slight difference in the time at which the profiles are taken occurs because the interaction plane Mach stem traveled faster than the ground plane Mach stem. Energy densities for this figure were computed from measurements taken at 0.4 metre above the ground and at 0.4 metre below the interaction plane.

It will be recalled that the ground surface for Shot 11 was furrowed in an effort to make it rough and soft. The fact that the ground surface Mach stem was significantly slower and weaker than the interaction plane Mach stem is presumably due to energy loss and redistribution over this rough ground surface. No such losses would be expected to occur at the ideal surface interaction plane. It is not clear from the profiles shown in the figure whether or not energy density differences at this distance from the surfaces are significant.

Peak energy densities at each shock front obtained from particle trajectory analysis are plotted as functions of range for the two Mach stem shocks in Figure 3.59. The slightly lower values of the peaks associated with the ground plane shock are apparent in this figure.

---

14. *H. L. Brode, "A Calculation of the Blast Wave from a Spherical Charge of TNT," RM-1965, The RAND Corporation, Santa Monica, California, 1957 (AD # 144302).*

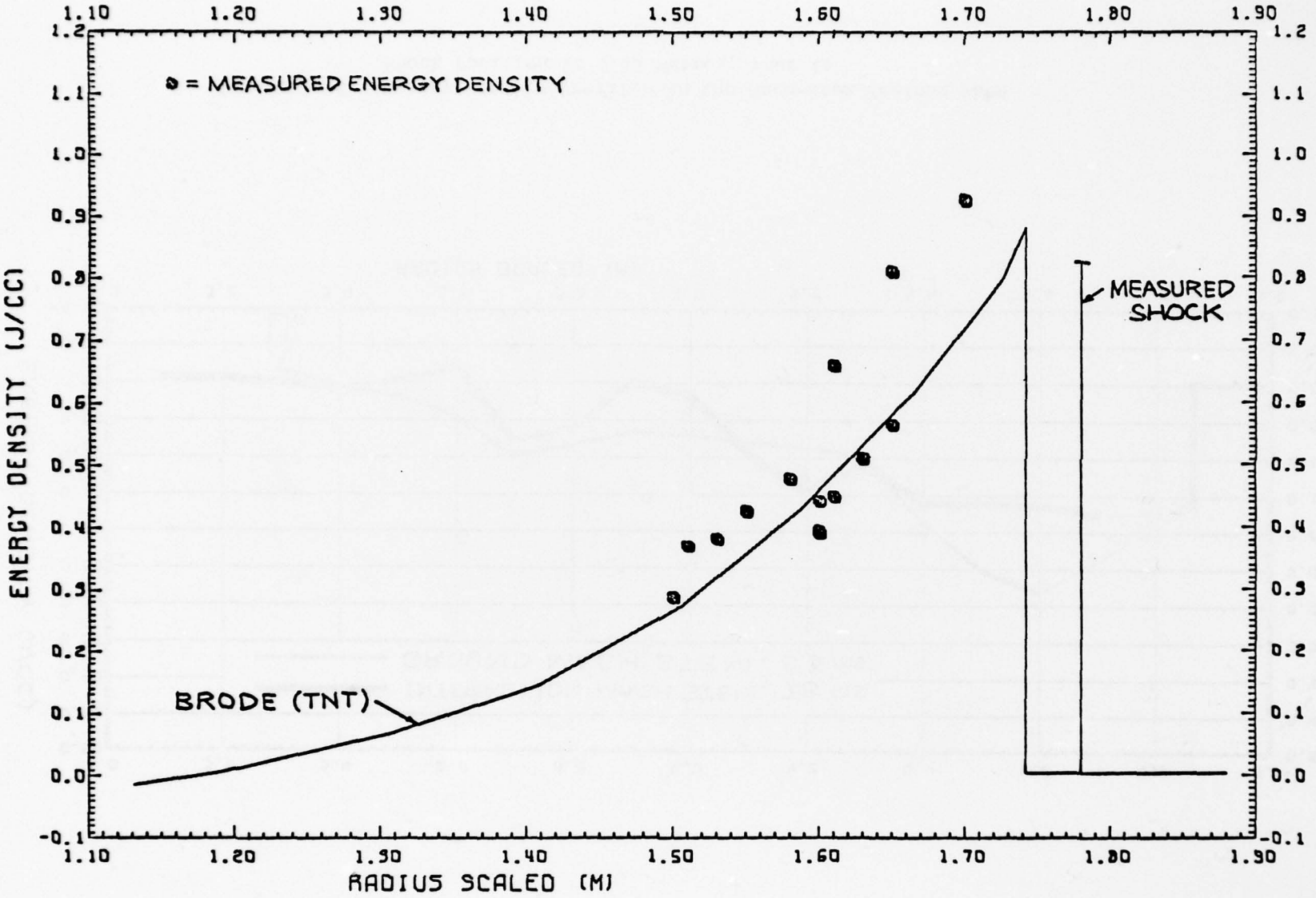

Figure 3.57. Energy Density in the Primary Wave of Shot 11 at 1.4 Milliseconds, Compared to Brode Profile

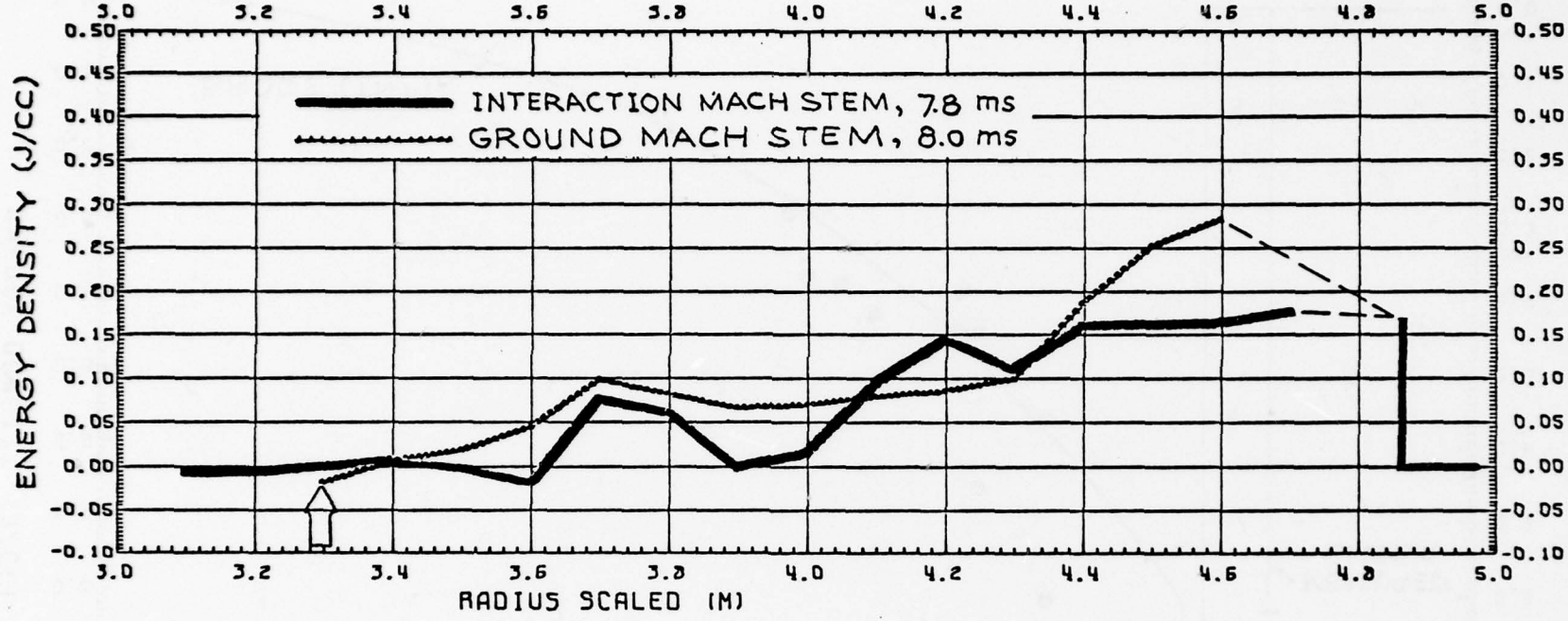

Figure 3.58. Energy Density Profiles in the Mach-Stem Regions when Shock Position is 4.83 Metres; Shot 11

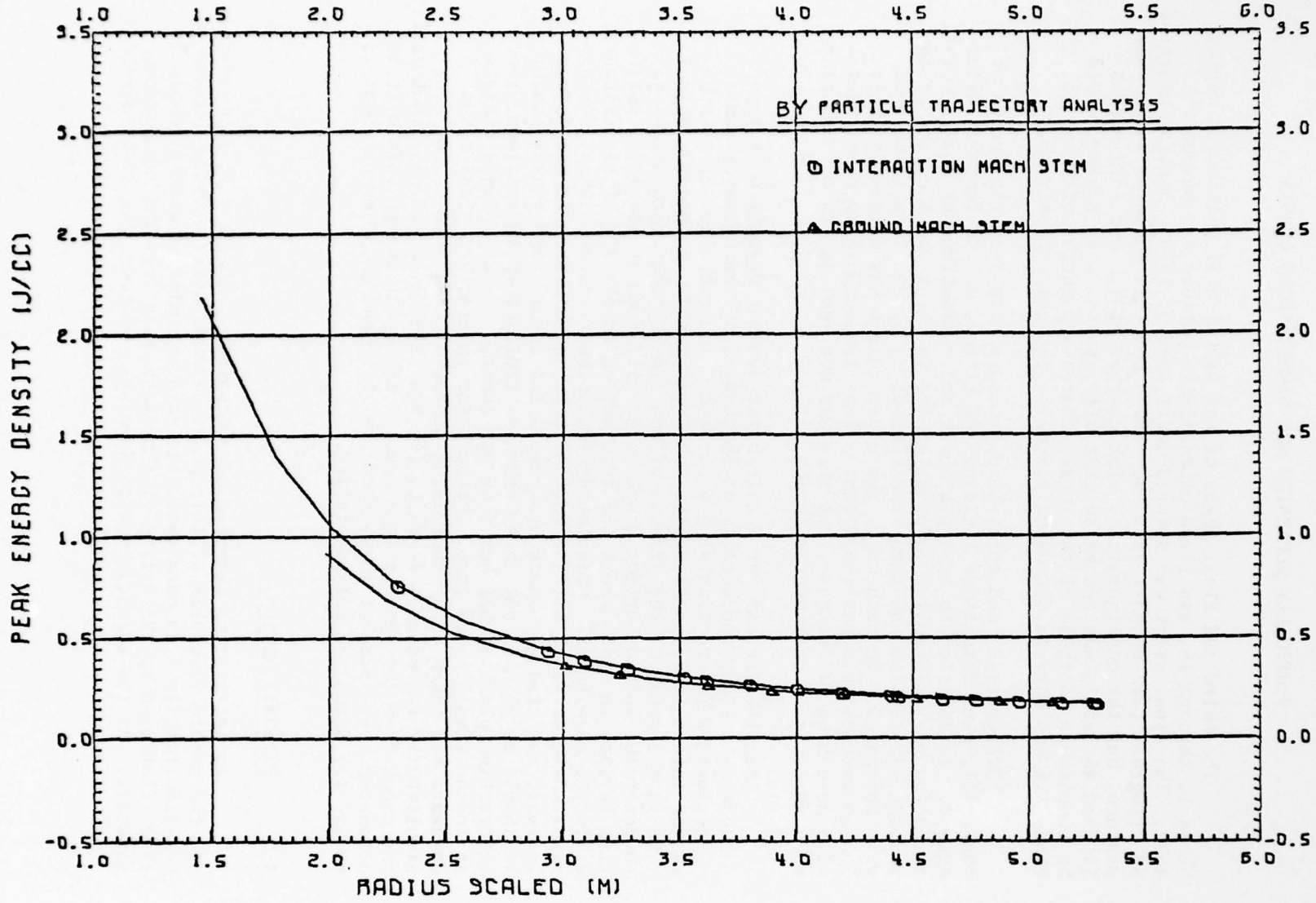

Figure 3.59. Energy Density at the Mach Stem Shock Fronts Obtained from Particle Trajectory Analysis

CHAPTER 4

VERTICALLY SEPARATED NON-SIMULTANEOUS BURSTS

The third and final phase of the DIPOLE WEST multiburst series, Shots 12 through 16, was fired primarily in October and November of 1974. The final event was delayed until June of 1975. Smaller charges, 98 kilograms (216 pounds) each, were used for this phase as an economy measure, but the configuration, with charges at 4.5 and 13.7 metres (15 and 45 feet), was chosen so that all results, when scaled, would be comparable to those of the larger charge-separation of Phase II. Phase III was carried out using pentolite charges exclusively.

Overpressure and total-head pressure data from the events of Phase III, plus details of fielding and firing, may be found in Reference 4. In addition to a single burst and a simultaneous double burst, fired to provide baseline information and to check the accuracy of the scaling, shots with non-simultaneities of 3, 5, and 10 milliseconds were detonated. In each case, the upper charge was detonated first. Subsequent analysis has shown that a 7-millisecond delay event would also have been of interest, but this was not realized in time to plan such an event as part of the series.

As with the earlier double-burst events, objective of this phase was to study the details of shock-wave system behavior under conditions of interaction with a surface. Incorporation of this behavior into calculational models was anticipated. A specific objective in the study of the effects of non-simultaneous detonations was to determine whether or not a Mach stem will form at the ideal reflecting surface in cases where the interacting shocks are of significantly different magnitudes. Calculated results had indicated that, for non-simultaneities of 10 milliseconds or more, a Mach stem is not formed. Instead, the stronger shock overpowers and engulfs the weaker shock. It should be pointed out that, for non-simultaneous detonations, the interaction plane is neither flat nor located midway between charges as in the simultaneous case. Rather, the interaction plane moves downward and takes on an increasing degree of curvature as the non-simultaneity increases. In fact, for the 10-millisecond non-simultaneity, the shock from the upper charge engulfs the lower charge before it is detonated. In spite of this, the 10-millisecond delay event, Shot 13, apparently detonated satisfactorily.

4.1 Fireball Motion

An interesting sequence of photographs, Figure 4.1, demonstrates how the double fireballs of this phase behaved under varying degrees of non-simultaneity. In each case, the adjacent edge of each fireball is first flattened by the action of the shock wave from the neighboring fireball. As the torusing motion develops, however, the lower fireball

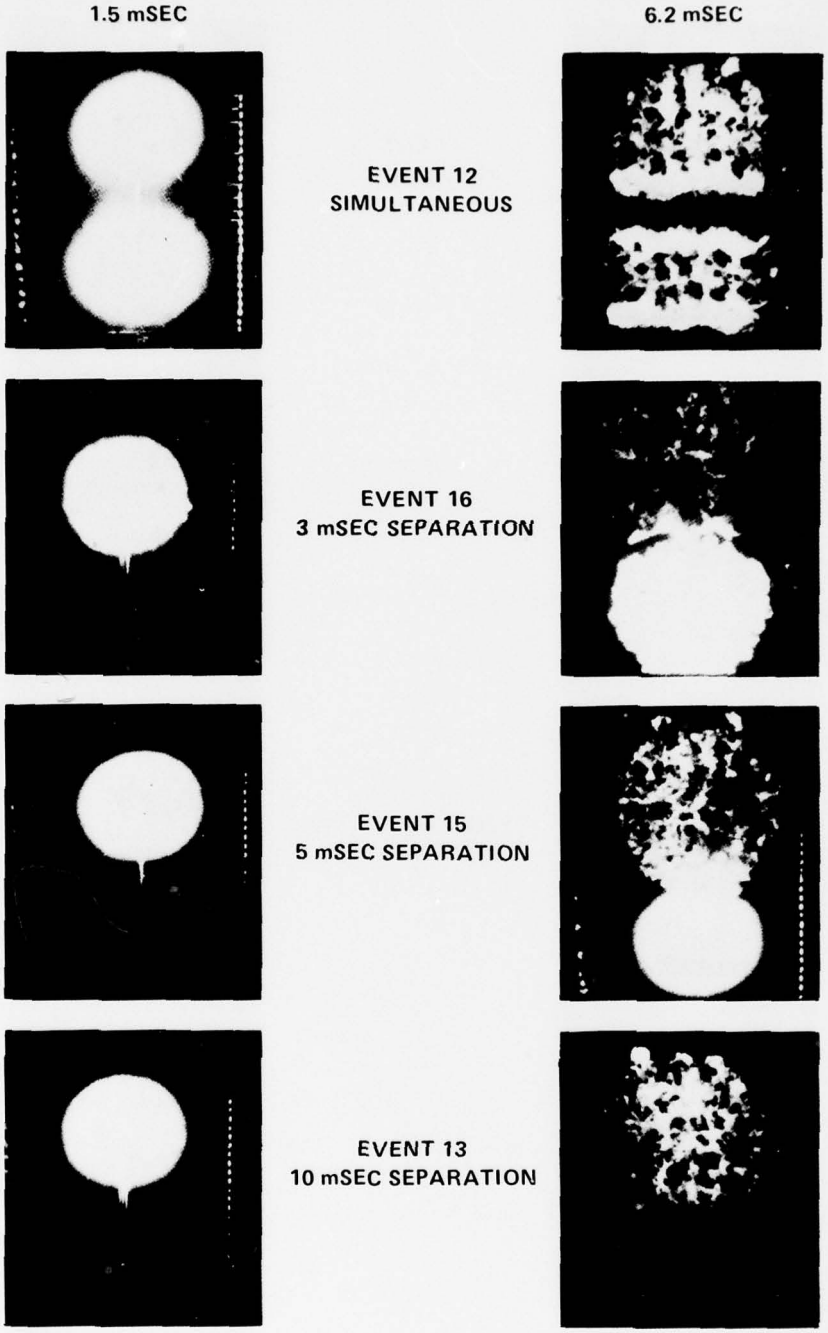

Figure 4.1(a). Fireballs of Non-Simultaneous Events at 1.5 and 6.2 Milliseconds After Detonation

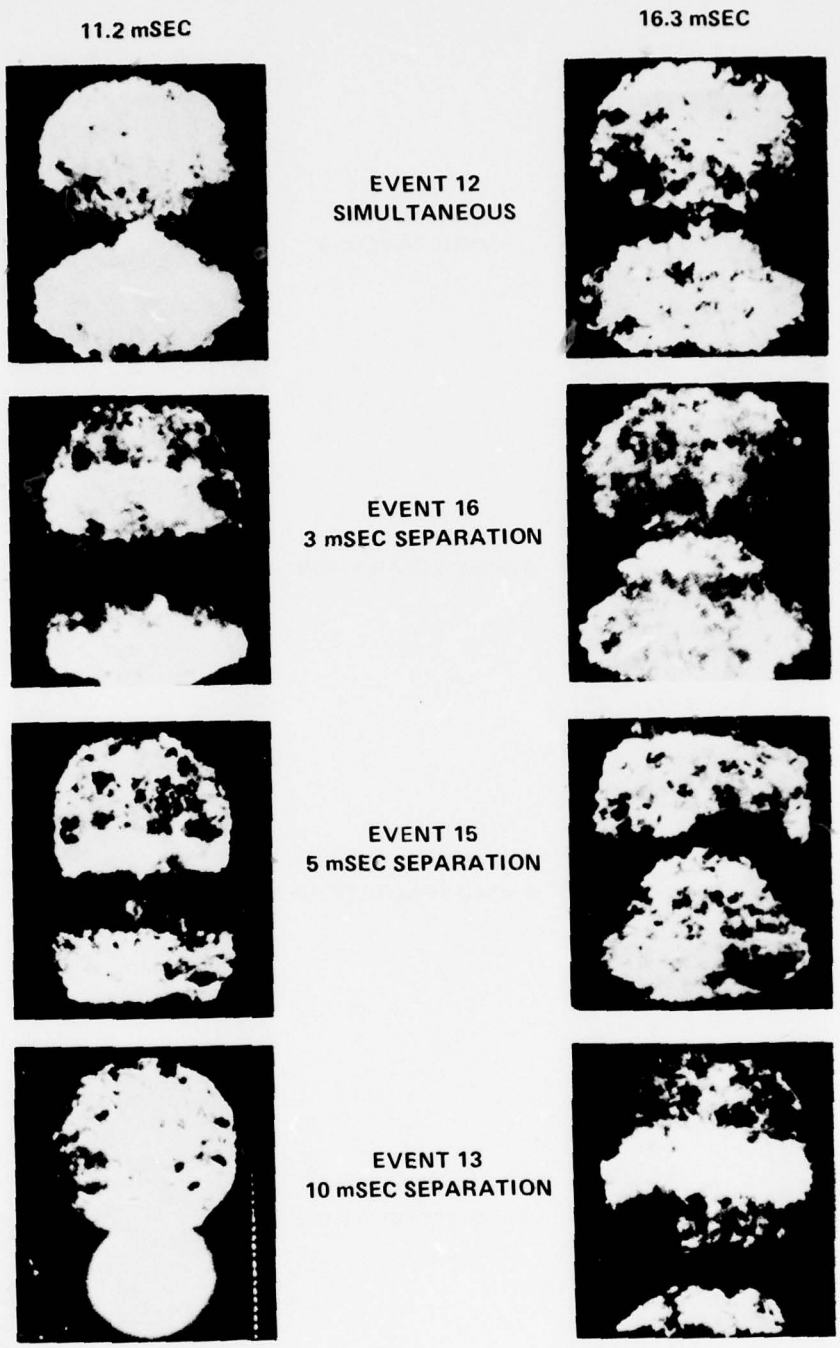

Figure 4.1(b). Fireballs of Non-Simultaneous Events at 11.2 and 16.3 Milliseconds After Detonation

is drawn upward into the fireball above it. This is probably because the upper torus is more fully developed, either, in the non-simultaneous case, because of greater maturity or, in the simultaneous case, because the lower torus development has been retarded by opposing forces from the two reflected shocks (the ground reflection and the ideal-plane reflection). Finally, although it is not clear from the photographic sequences, the lower fireball is drawn completely up into the upper fireball and a single fireball/torus is formed.

4.2 Shock Interaction and Mach Stem Formation

The interaction of shock waves and the subsequent formation of Mach stems in the case of non-simultaneous detonations are illustrated in Figures 4.2 and 4.3. Figure 4.2 is from Shot 16, the 3-millisecond delay event. Although somewhat distorted by the non-simultaneity, the shock system is basically the same as for simultaneous events. Mach stem shocks are formed both above and below the ideal reflecting plane, as well as above the ground. Three separate triple-point paths are distinguishable.

The interesting and important result is demonstrated by Figure 4.3. This figure is from Shot 15, for which the non-simultaneity was 5 milliseconds. As can be observed, there is no Mach stem formed on the lower side of the ideal reflecting plane, and only two triple-point paths are evident. This behavior for Shot 15 was also displayed in Figure 1.5.

The lack of a Mach stem for a 10-millisecond non-simultaneity was first predicted by hydrodynamic calculations with HULL (Reference 10). A later calculation for a 5-millisecond non-simultaneity confirmed the result in this case also. This agreement of calculational and experimental information represents an important validation of hydrodynamic techniques in general, and of the HULL code in particular. Further details of the comparison between calculated and experimental results under conditions of non-simultaneous detonation are to be published in Reference 15.

4.3 Scaling Under Multiburst Conditions

Although the Sachs scaling techniques discussed in Section 1.4 have been widely used over a number of years, most of the experience with these techniques has been with single bursts. Effects of charge weight, height-of-burst, and environmental factors (pressure and temperature) have been investigated, and Sachs scaling has proved to

---

15. *C. E. Needham, "Numerical Simulation of Air Blast fron Non-Simultaneous Detonations," to be published by the Air Force Weapons Laboratory, Kirtland Air Force Base, New Mexico 87117.*

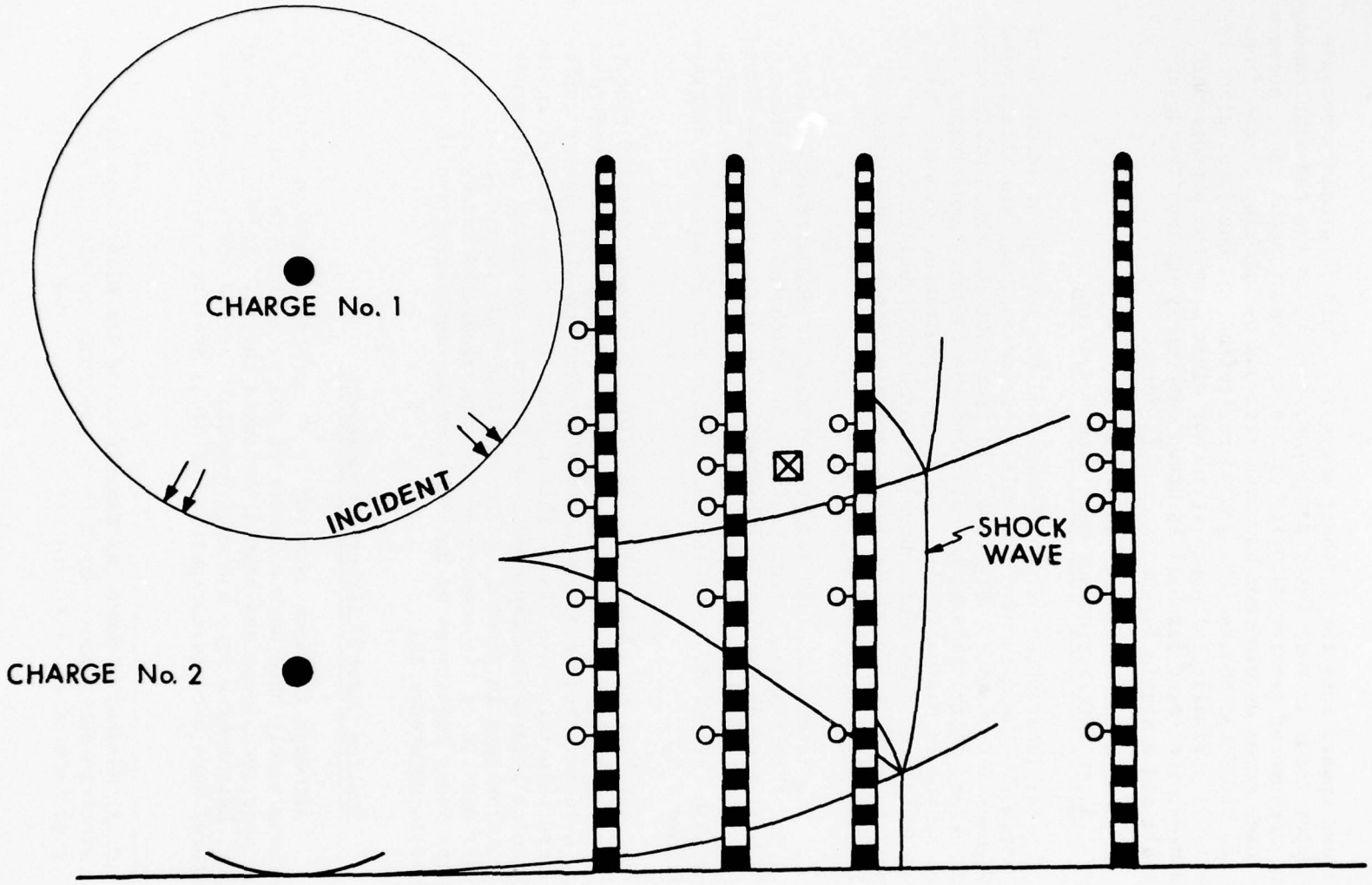

Figure 4.2. Interaction of Shock Waves and Formation of Mach Stems Under Condition of 3-Millisecond Non-Simultaneity; Shot 16

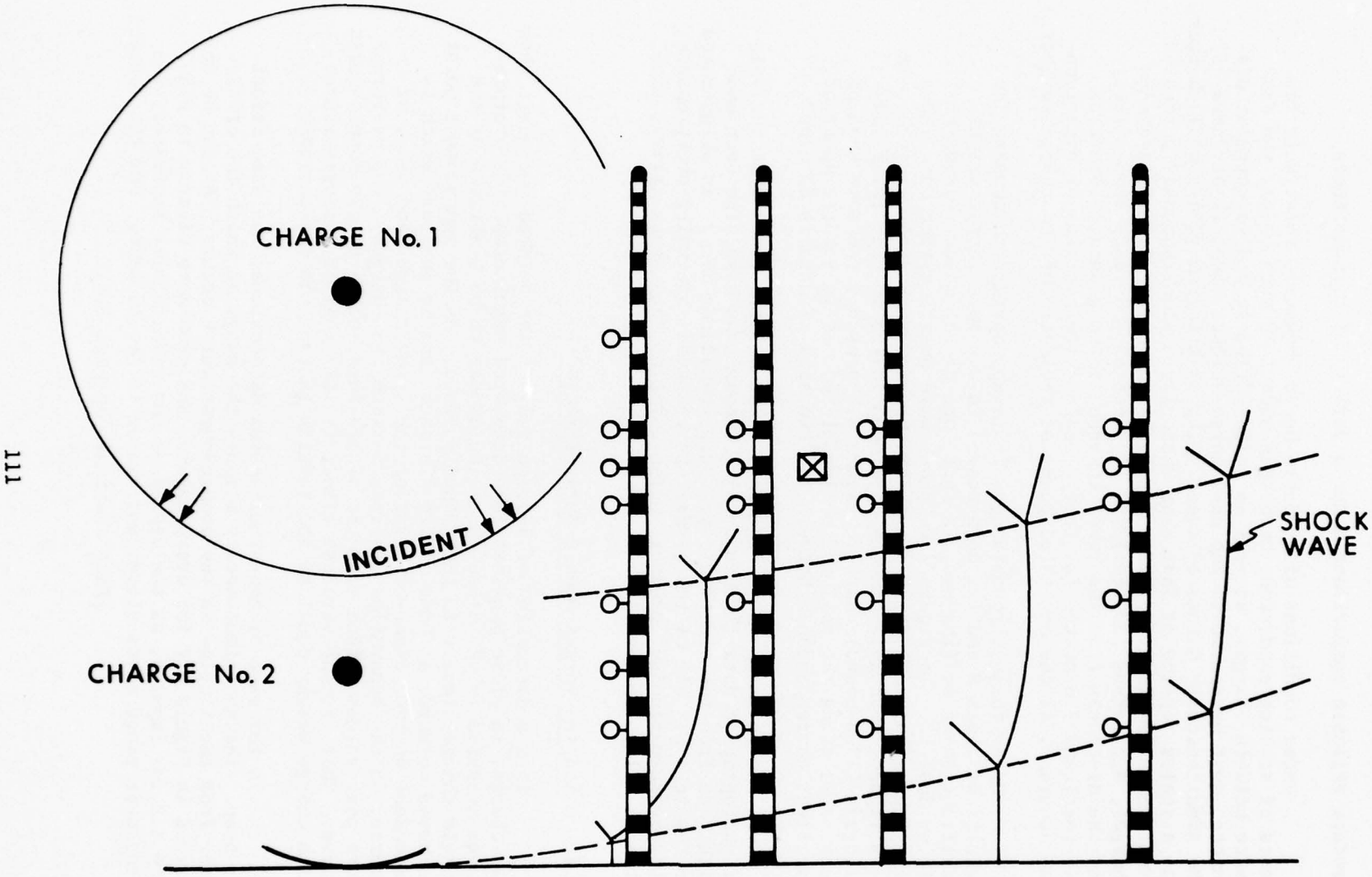

Figure 4.3. Interaction of Shock Waves and Formation of Mach Stems Under Condition of 5-Millisecond Non-Simultaneity; Shot 15

produce reliable comparisons under a variety of circumstances.

Under conditions of a double burst, however, relatively few tests of scaling conditions have been made. In such cases, the distance between charges, as well as height-of-burst and measurement distances, must be scaled to the new charge weight. Shot 12 of Phase III, the simultaneously detonated event using 98-kilogram (216-pound) charges, was a scaled replica of Shot 8 of Phase II, a simultaneously detonated event with 490-kilogram (1080-pound) charges. The distances between charges, 9.2 metres (30 feet) and 15.2 metres (50 feet) respectively, and the distances from the lower charges to the ground, 4.6 metres (15 feet) and 7.6 metres (25 feet), scale, within limits of experimental accuracy, as the one-third power of the ratio of the charge weights.

Under these circumstances, it is appropriate to compare the results of Shots 8 and 12, both scaled to the same charge weight. Verification of scaling was, in fact, one of the major reasons for firing Shot 12. In Figure 4.4, shock wave position-time data taken along the ideal reflecting plane for the two events are compared. In this figure, both sets of data have been scaled to that for a 454-kilogram (1000-pound) charge. Figure 4.5 presents the same kind of data taken along the real reflecting plane. As is readily apparent, excellent correspondence between the two sets of data is obtained.

The comparisons of Figures 4.4 and 4.5 are taken from analysis of photographic data (Reference 5). Comparisons have also been made with data from the electronic pressure transducer array, as illustrated in Figure 4.6. All of the parameters compared, including overpressure, overpressure-impulse, pressure pulse duration, and shock arrival time, show excellent agreement.

4.4 Single- versus Double-Burst Effects

In the discussion of Section 3.3, it was pointed out that, when two charges in close proximity are detonated simultaneously, overpressures measured in the close-in region appear to be generated by the single charge closest to the ground surface. As the measurement point is moved outward, at some finite distance from Ground Zero which is dependent on the height-of-burst of the lower charge (and also, of course, on the separation distance between the charges), the overpressure peak values switch from the single-burst curve to the double-burst curve. That is, the airblast effect is like that of a single source with charge weight equal to the total weight of the two charges.

In the case of non-simultaneous detonations, the same effect is seen. The non-simultaneity affects the range at which the crossover from the single- to the double-burst curve occurs. As can be observed in Figure 4.7 for overpressure, and even more clearly in Figure 4.8 for impulse, as the degree of non-simultaneity increases, the crossover range moves closer and closer to Ground Zero. For the longest

(Text continues on page 118.)

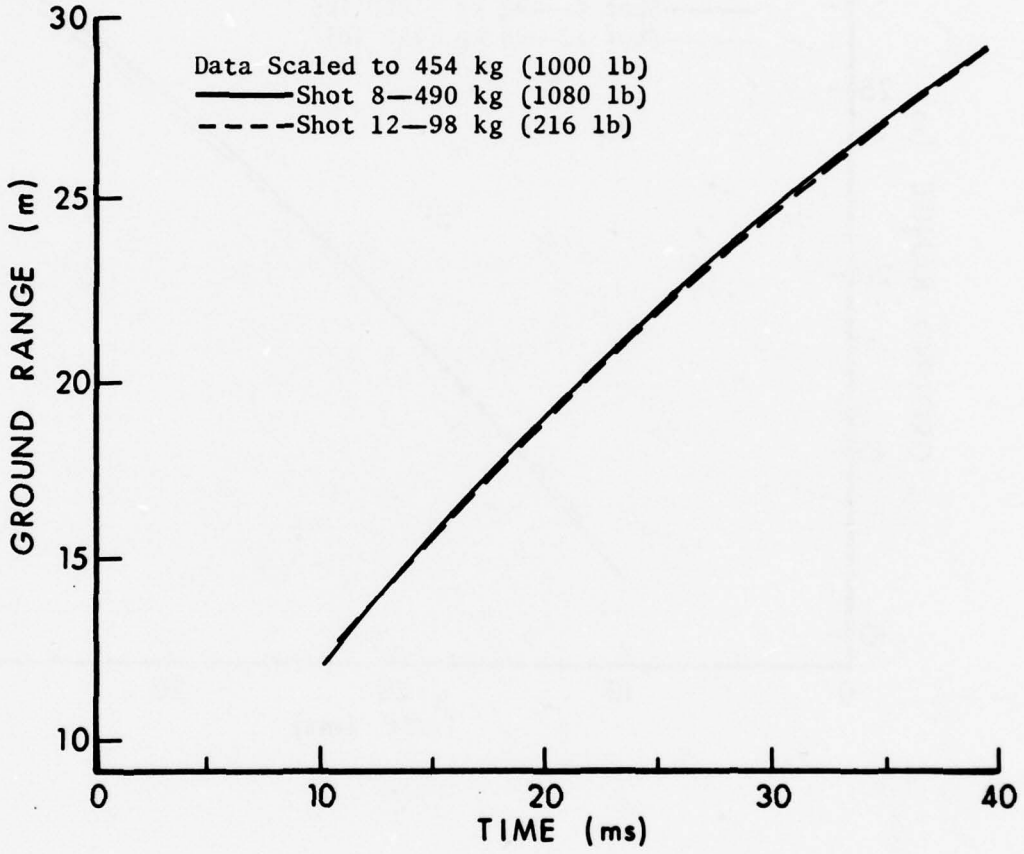

Figure 4.4. Shock Wave Position-Time Data Along the Ideal Reflecting Plane for Verification of Scaling; Shots 8 and 12

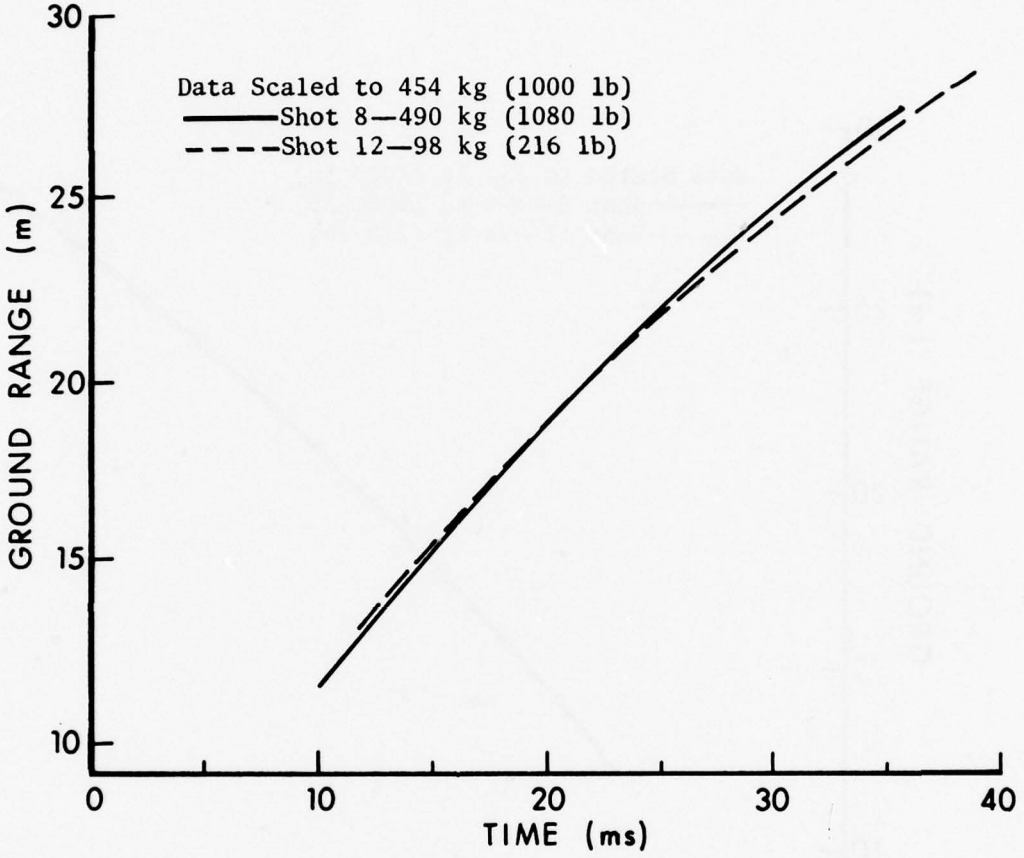

Figure 4.5. Shock Wave Position-Time Data Along the Real Reflecting Plane for Verification of Scaling; Shots 8 and 12

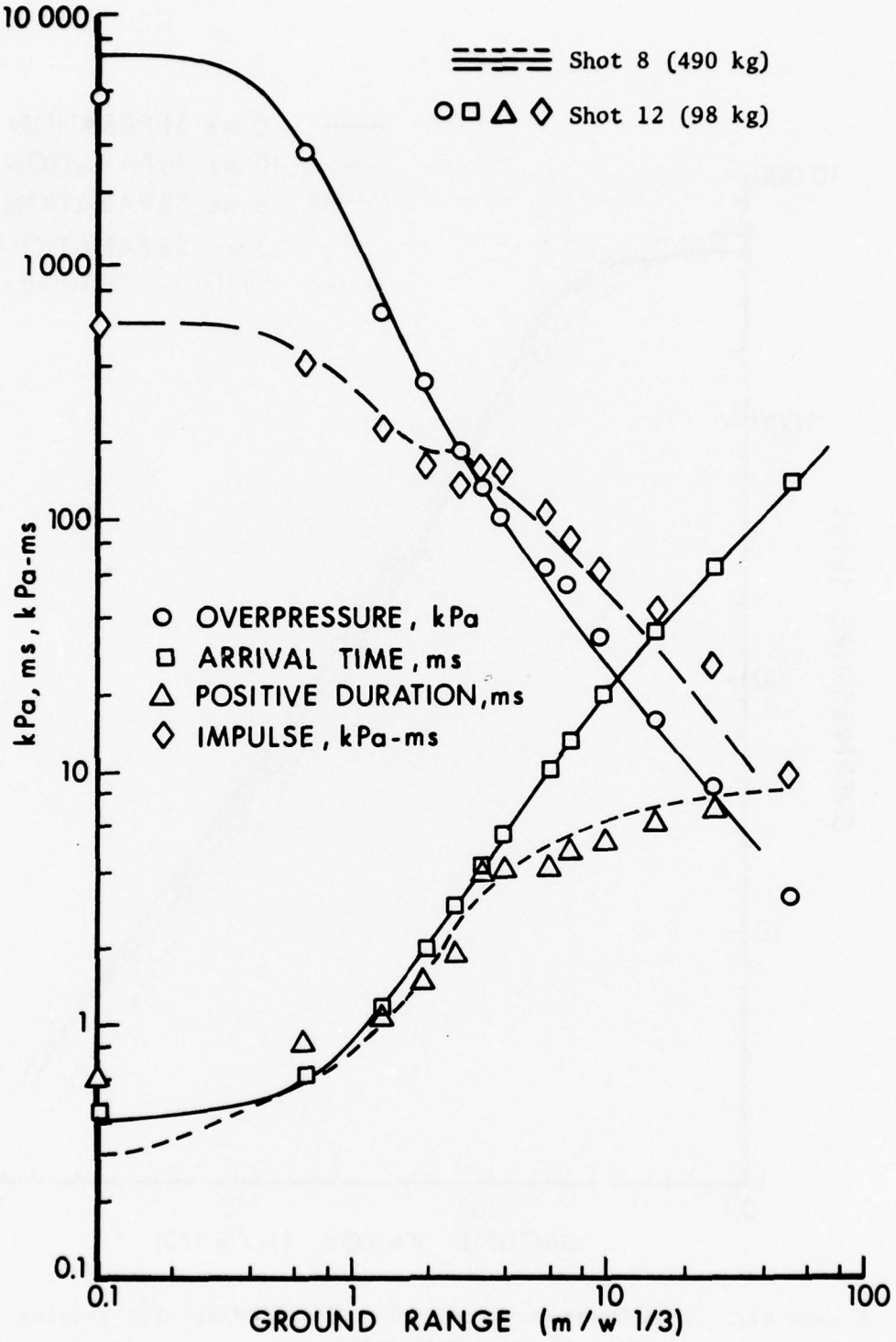

Figure 4.6. Comparison of Scaled Air Blast Parameters from Shots 8 and 12

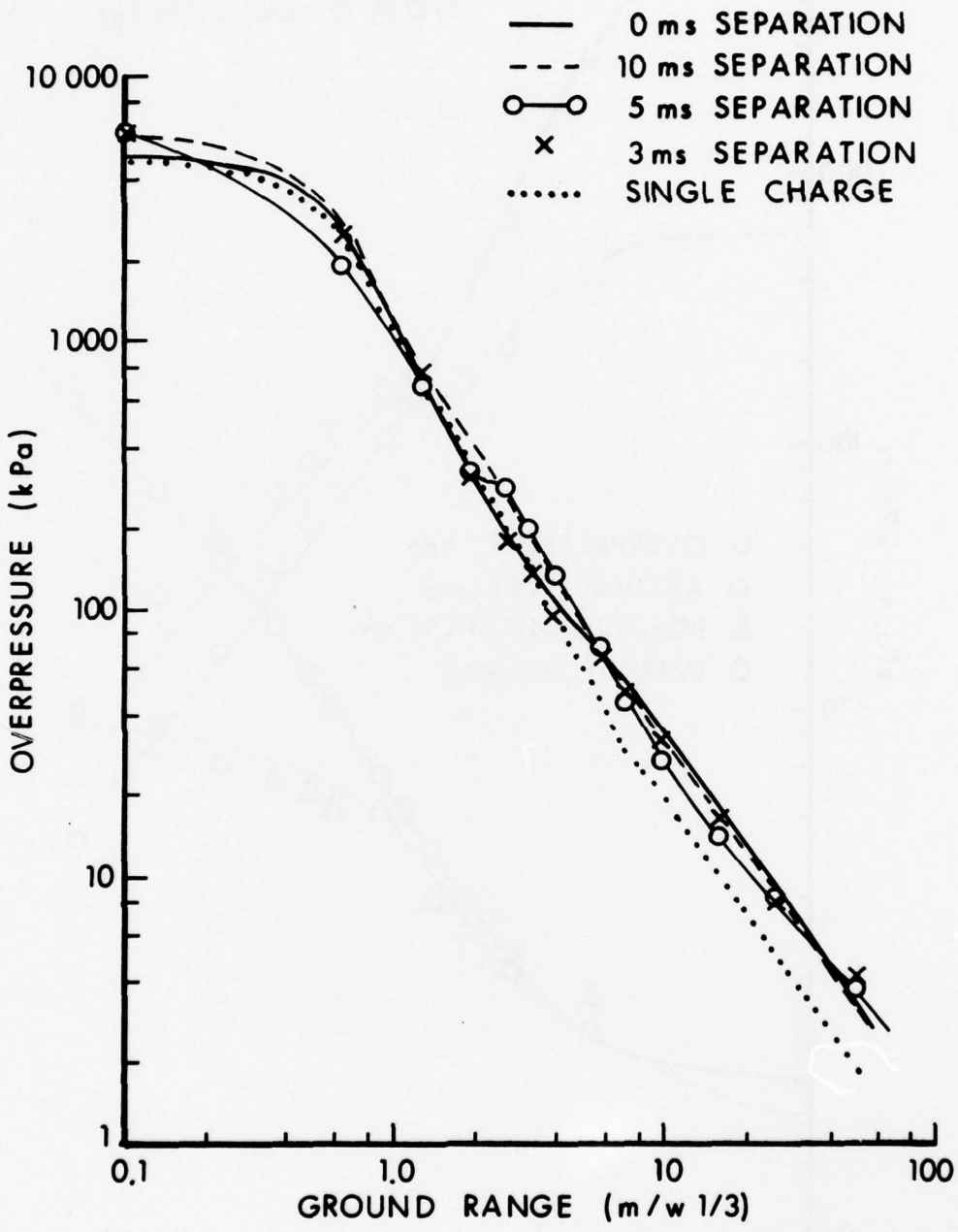

Figure 4.7. Peak Overpressures versus Ground Range for Varying Degrees of Non-Simultaneity

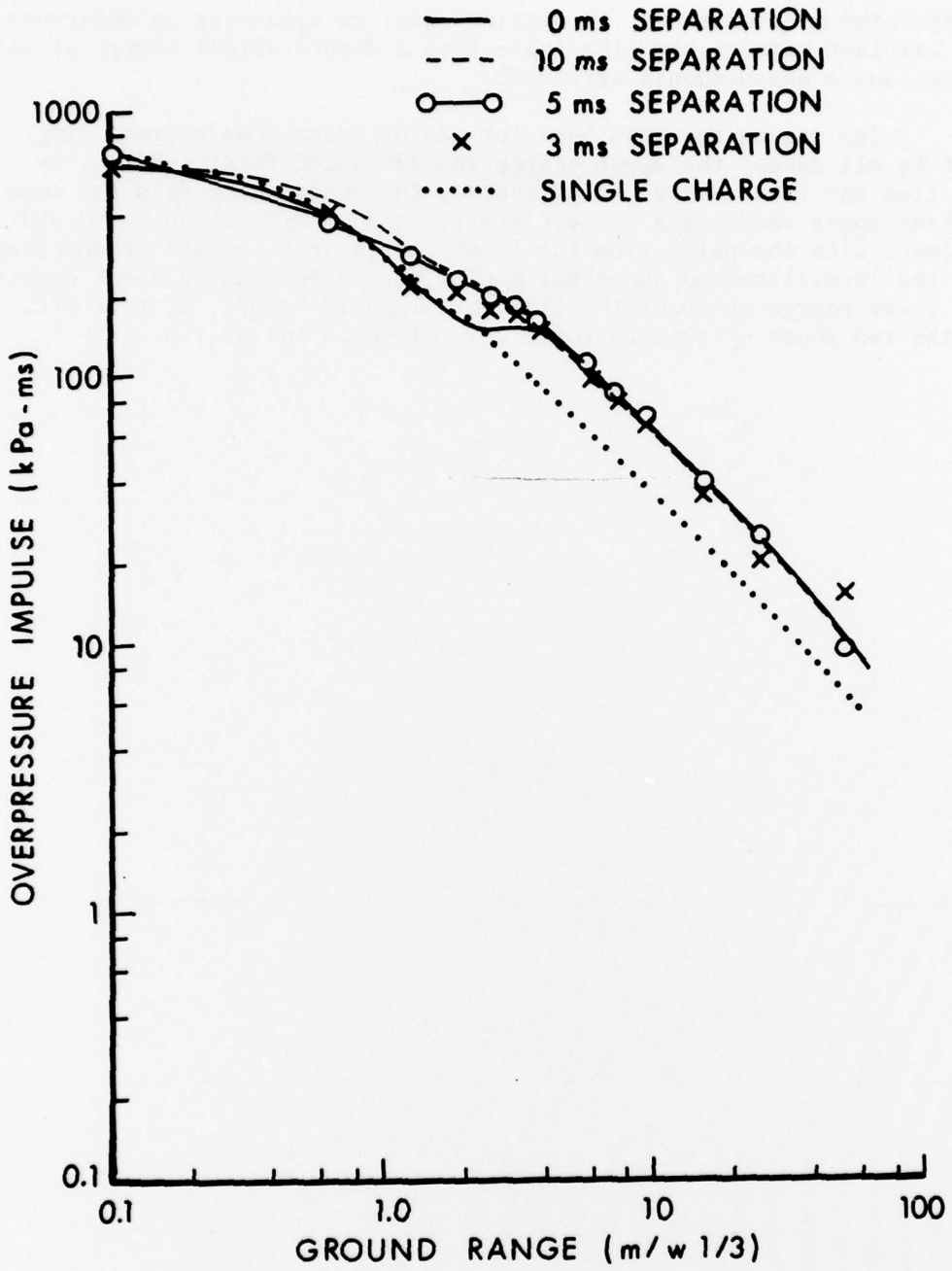

Figure 4.8. Peak Overpressure-Impulses versus Ground Range for Varying Degrees of Non-Simultaneity

delay between detonations, 10 milliseconds, no crossover is observed: the airblast effects are like those from a double-weight charge at all ranges where measurements were made.

The reason for this behavior can be understood by recalling that in all cases, the upper charge was detonated first. Hence, by the time the lower charge is detonated, the shock pulse from the more distant upper charge has a "head start," and it will catch up to and coalesce with the pulse from the lower charge at a smaller ground-range. For the 10-millisecond non-simultaneity, the upper-charge shock engulfs the lower charge at about the time, or slightly before, it goes off, so the two shock systems coalesce very close to the origin.

CHAPTER 5

CONCLUSIONS AND RECOMMENDATIONS

The DIPOLE WEST multiburst series, consisting of 16 events which were conducted over three summer testing periods, produced a large quantity of data. About 950 channels of electronic pressure records were obtained, plus a significant amount of high-speed photographic film. Analysis of this data has continued for several years, and some aspects of the analysis were continuing as this report was being prepared.

From this analysis, several conclusions and validations have been drawn. In addition, several recommendations for areas in which further study would be of interest have been made. This final chapter reiterates those conclusions which the authors perceive to be the most interesting and significant, and discusses some recommendations. The possibility that other conclusions may be drawn from the data at a later time, or that other areas of interest for additional study will emerge, is not precluded.

Among the more interesting results obtained were those concerning the redistribution of energy in blast waves as they pass over different types of real surfaces and over ideal surfaces. It seems clear that some redistribution occurs, and that the amount of energy affected is greater for soft, rough surfaces than for hard, smooth surfaces or for ideal surfaces. It is not clear if the absorbed energy is fed back into the shock system from the ground at a later time, or if energy from the higher elevations flows into the region where interactions with the ground are taking place. Clarification of the energy redistribution issue awaits more precise measurement and analysis techniques, with probes designed to take measurements within inches of the ground. Such small-scale measurement arrays are planned for MIGHTY MACH, a high-explosive test series to be fielded in the summers of 1978 and 1979.

Another significant result of the analysis of the DIPOLE WEST multiburst data was the development and refinement of the photogrammetric techniques. Although such techniques have been used before, the extent and sophistication of the analysis of these events are unprecedented. Much of the software for data handling and correcting, which will be useful for other photogrammetric analyses in the future, was developed during the course of this program.

The photogrammetric techniques have proven to be very effective. The shock trajectory analysis provided excellent information for visualization of the growth of the triple point, and for determination of the existence of a Mach stem under a variety of conditions.

A problem in the analysis was that of an appropriate shape to

choose for the Mach stem shock wave at the surface. Spherical and cylindrical shapes were assumed, but neither of these is totally accurate. A strong recommendation is made for a theoretical study of the shape of the Mach stem shock produced by a spherical shock wave reflecting from a plane surface.

Photogrammetric analysis of particle trajectories (smoke puffs) produced particle velocity and density fields over the vertical plane at various times. These results were then manipulated to produce, for the first time, dynamic pressure and energy fields. Although the energy calculation requires more precise data to produce useful results, the dynamic pressures, when further manipulated to produce overpressure and total head pressure records, provided outstanding agreement with similar records from the electronic pressure transducers. This agreement is felt to provide validation of both data collection and data handling techniques.

A third interesting result was that of the airblast at first appearing to arise from a single charge, and then later (or, actually, at greater ranges) switching over so that it appears to rise from a single double-weight charge. The extension of this observation into the non-simultaneous part of the series provided insight into the way shock waves of varying strengths overtake one another and interact with each other.

The most significant non-simultaneity effect to emerge was that of the failure of the system to develop a Mach stem at the interaction surface for non-simultaneities of 5 and 10 milliseconds. This lack of a Mach stem had been predicted for the 10-millisecond case, and the experimental result provided an excellent validation of the HULL hydrodynamic code. In the 5-millisecond case, however, it was only after analysis of the data did not show a Mach stem that the code results were studied closely enough to determine that the Mach stem did not appear here either. For the simultaneous and 3-millisecond delay cases, the Mach stem was seen to develop in the expected manner.

As was mentioned at the beginning of this report, code verification was a major objective and one of the main reasons for fielding the series. The validation provided by the non-simultaneous comparison discussed in the previous paragraph, plus the general agreement of parameters over all of the single- and double-burst events, was a strong confirmation of the value of hydrodynamic calculational techniques, and one of the more gratifying results of the undertaking.

Qualitative results concerning fireball interaction and cloud rise under multiburst conditions were obtained. These were particularly interesting in the case of non-simultaneous detonations, in which the lower fireball was observed to move up and become part of the upper fireball, so that a single fireball/torus system was formed.

Finally, scaling techniques used extensively for single-burst detonations were confirmed to apply to multiburst situations as well. Care must be taken, of course, to apply the scaling to dimensions of the configuration, such as the distance between charges and the height of burst, as well as to all other parameters.

Now that Mach stem formation over rough and smooth surfaces has been investigated, the understanding gained might usefully be applied to situations of practical interest for defense considerations. One possibility would be to consider, both theoretically and experimentally, Mach stem formation over igloos, hangars, and other buried or partially buried structures. Spacing of the structures should be considered, as well as various configurations of the multiburst environment. In this way, information with direct application to some of the problems presently faced by the defense community could be obtained.

REFERENCES

1. C. E. Needham and L. A. Wittwer, "The Air Force Weapons Laboratory Low Altitude Multiple Burst (LAMB) Model," AFWL-DYT-75-2, Air Force Weapons Laboratory, Kirtland Air Force Base, New Mexico 87117 (unpublished).

2. A. Karlsson and H. Wagner, "Photographic Study of the Reflection of Spherical Shock Waves, Mach Front Formation, and Front Velocities," August 1961. Translation by SCITRAN (Scientific Translation Service), Santa Barbara, California 93108.

3. J. H. Keefer and R. E. Reisler, "Multiburst Environment—Simultaneous Detonations, Project DIPOLE WEST," BRL Report No. 1766, USA Ballistic Research Laboratory, Aberdeen Proving Ground, Maryland 21005, March 1975. (AD # A009485)

4. R. E. Reisler and B. A. Pettit, "Project DIPOLE WEST—Multiburst Environment (Non-Simultaneous Detonations)," BRL Report No. 1921, USA Ballistic Research Laboratory, Aberdeen Proving Ground, Maryland 21005, September 1976. (AD # A031985)

5. John Wisotsky, "DIPOLE WEST Technical Photography," Denver Research Institute, Denver, Colorado 80208, DNA 4325F, Defense Nuclear Agency, Washington, D.C. 20305, February 1977.

6. R. E. Reisler and L. W. Kennedy, "Air Blast Dynamic Pressures from Simultaneous and Non-Simultaneous Multiburst Detonations," BRL Report TR-02043, USA Ballistic Research Laboratory, Aberdeen Proving Ground, Maryland 21005, February 1978. (AD #B027298L)

7. J. M. Dewey, D. F. Classen, and D. J. McMillin, "Photogrammetry of the Shock Front Trajectories on DIPOLE WEST Shots 8, 9, 10, and 11," UVIC PF 1-75, University of Victoria, British Columbia, Canada V8W-2Y2, July 1975 (also published by the Defense Nuclear Agency as DNA 3777F).

8. J. M. Dewey, D. J. McMillin, and D. Trill, "Photogrammetry of the Particle Trajectories on DIPOLE WEST Shots 8, 9, 10, and 11," University of Victoria, British Columbia, Canada, published by the Defense Nuclear Agency in four volumes as follows:

   Volume I - Shot 10, DNA 4326F-1, June 1977;
   Volume II - Shot 9, DNA 4326F-2, October 1977;
   Volume III - Shot 8, DNA 4326F-3, January 1978;
   Volume IV - Shot 11, DNA 4326F-4, March 1978.

9. J. M. Dewey, D. J. McMillin, and D. F. Classen, "Photogrammetry of Spherical Shocks Reflected from Real and Ideal Surfaces," University of Victoria, British Columbia, Canada, *Journal of Fluid Mechanics*, vol. 81, part 4, 1977 (published in Great Britain).

10. HULL documentation exists only in the form of comment cards within the code. Further information is available from the Air Force Weapons Laboratory, Kirtland Air Force Base, New Mexico 87117, ATTN: Mr. Charles Needham, DES.

11. R. E. Reisler, B. A. Pettit, and L. W. Kennedy, "Air Blast Data from Height-of-Burst Studies in Canada; Volume II, HOB 45.4 to 144.5 Feet," BRL Report No. 1990, USA Ballistic Research Laboratory, Aberdeen Proving Ground, Maryland 21005, May 1977.

12. R. E. Reisler, B. A. Pettit, and L. W. Kennedy, "Air Blast Data from Height-of-Burst Studies in Canada; Volume I, HOB 5.4 to 71.9 Feet," BRL Report No. 1950, USA Ballistic Research Laboratory, Aberdeen Proving Ground, Maryland 21005, December 1976. (AD #B016344L)

13. J. M. Dewey and D. J. McMillin, "Energy Density Calculations: DIPOLE WEST Shot 11," University of Victoria, British Columbia, Canada, to be published by USA Ballistic Research Laboratory, Aberdeen Proving Ground, Maryland 21005, 1978.

14. H. L. Brode, "A Calculation of the Blast Wave from a Spherical Charge of TNT," RM-1965, The RAND Corporation, Santa Monica, California, 1957. (AD # 144302)

15. C. E. Needham, "Numerical Simulation of Air Blast from Non-Simultaneous Detonations," to be published by the Air Force Weapons Laboratory, Kirtland Air Force Base, New Mexico 87117.

DISTRIBUTION LIST

No. of Copies	Organization
12	Commander Defense Documentation Center ATTN: DDC-DDA Cameron Station Alexandria, VA 22314
4	Director of Defense Research & Engineering ATTN: DD/TWP DD/S&SS DD/I&SS AD/SW Washington, DC 20301
3	Director Defense Advanced Research Projects Agency ATTN: Tech Library NMRO PMO 1400 Wilson Boulevard Arlington, VA 22209
6	Director Defense Nuclear Agency ATTN: STTL (Tech Lib, 2 cys) SPAS, Mr. J. Moulton DDST, Mr. P. H. Haas SPSS, Dr. George Ullrich SPAS, Mr. D. Kohler Washington, DC 20305
2	Commander Field Command, DNA ATTN: FCTMOF Kirtland AFB, NM 87115
2	Department of Defense Explosives Safety Board ATTN: R. Perkins Dr. Tom Zaker Room GS-270, Forrestal Bldg. Washington, DC 20314
1	Commander US Army Materiel Development and Readiness Command ATTN: DRCDMD-ST 5001 Eisenhower Avenue Alexandria, VA 22333
1	Commander US Army Aviation Research and Development Command ATTN: DRSAV-E P. O. Box 209 St. Louis, MO 63166
1	Director US Army Air Mobility Research and Development Laboratory Ames Research Center Moffett Field, CA 94035
1	Commander US Army Electronics Research and Development Command Technical Support Activity ATTN: DELSD-L Fort Monmouth, NJ 07703
1	Commander US Army Communications Rsch and Development Command ATTN: DRDCO-PPA-SA Fort Monmouth, NJ 07703
2	Commander US Army Missile Research and Development Command ATTN: DRDMI-R DRDMI-S, Ch Scientist Redstone Arsenal, AL 35809
1	Commander US Army Missile Materiel Readiness Command ATTN: DRSMI-AOM Redstone Arsenal, AL 35809

DISTRIBUTION LIST

No. of Copies	Organization
2	Commander US Army Tank Automotive Rsch and Development Command ATTN: DRDTA-UL DRDTA-RHT, LT P. Hasek Warren, MI 48090
2	Commander US Army Armament Materiel Readiness Command ATTN: SARRI-LR, B. Morris DRSAR-LEP-L, Tech Lib Rock Island, IL 61299
4	Commander US Army Armament Research and Development Command ATTN: DRDAR-TSS (2 cys) P. Angelotti Mr. Demitrack Dover, NJ 07801
4	Commander US Army Harry Diamond Labs ATTN: DRXDO-TI/012 DRXDO-NP, F. Wimenitz DRXDO-NP, J. Gaul DRXDO-NP, J. Gwaltney 2800 Powder Mill Road Adelphi, MD 20783
1	Director US Army Materials and Mechanics Research Center ATTN: Tech Lib Watertown, MA 02172
1	Commander US Army Foreign Science and Technology Center ATTN: Research & Data Branch 220 7th Street, NE Charlottesville, VA 22901
3	Commander US Army Nuclear Agency ATTN: ATCN-W, CAPT M. Bowling CDINS-E Technical Library 7500 Backlick Rd, Bldg. 2073 Springfield, VA 22150
1	Director US Army TRADOC Systems Analysis Activity ATTN: ATAA-SL, Tech Lib White Sands Missile Range NM 88002
1	HQDA (DAMA-AR, NCB Division) Washington, DC 20310
3	Director US Army Advanced BMD Technology Center ATTN: Mr. B. E. Kelley Mr. M. Capps Mr. Marcus Whitfield P. O. Box 1500 Huntsville, AL 35807
1	Commander US Army Ballistic Missile Defense Systems Command ATTN: SSC-DH, H. Solomonson P. O. Box 1500 Huntsville, AL 35807
1	Commander US Army Ballistic Missile Defense Program Office ATTN: DACS-SAE-S, J. Shea 5001 Eisenhower Avenue Alexandria, VA 22333

DISTRIBUTION LIST

No. of Copies	Organization
2	Commander US Army Engineer Waterways Experiment Station ATTN: Library W. Flateau P. O. Box 631 Vicksburg, MS 39180
3	Chief of Naval Research Department of the Navy ATTN: T. Quinn, Code 464 Technical Library J. L. Warner, Code 464 Washington, DC 20360
2	Commander Naval Ship Engineering Center ATTN: J. R. Sullivan NSEC 6105-G Technical Library Hyattsville, MD 20782
4	Commander Naval Surface Weapons Center ATTN: Code 1224, Navy Nuclear Programs Office Code 241, J. Petes Code 730, Tech Lib J. Pittman Silver Spring, MD 20910
1	Commander Naval Weapons Evaluation Facility ATTN: Document Control Kirtland AFB, NM 87117
1	Commander Naval Civil Engineering Lab ATTN: Dr. W.A. Shaw, Code L31 Port Hueneme, CA 93041
3	Director Naval Research Laboratory ATTN: M. Persechino G. Cooperstein Tech Lib, Code 2027 Washington, DC 20375
1	HQ USAFSC (DLCAW, Tech Lib) Andrews AFB Washington, DC 20331
1	AFOSR (OAR) Bolling AFB, DC 20332
1	RADC (Docu Lib, FMTLD) Griffis AFB, NY 13440
4	AFWL (CA, Dr. A. Guenther; DYT, Charles Needham; DYT, MAJ G. Gonong; S. Melzer) Kirtland AFB, NM 87117
1	AFCRL (F. Doherty) L. G. Hanscom Field Bedford, MA 01730
1	SAMSO (Library) P. O. Box 92960 Los Angeles, CA 90009
3	AFTAC (K. Rosenlof; R. McBride; G. Leies) Patrick AFB, FL 32925
2	AFML (G. Schmitt, MAS; D. Schmidt) Wright-Patterson AFB, OH 45433
2	Energy Research and Development Administration Dept of Military Applications ATTN: R&D Branch Library Branch, G-043 Washington, DC 20545

DISTRIBUTION LIST

No. of Copies	Organization
2	Director Los Alamos Scientific Lab ATTN: Dr. J. Taylor Technical Library P. O. Box 1663 Los Alamos, NM 87544
1	Director National Aeronautics and Space Administration Langley Research Center ATTN: Code 04.000 Langley Station Hampton, VA 23365
1	Director NASA Scientific & Technical Information Facility ATTN: SAK/DL P. O. Box 8757 Baltimore/Washington International Airport, MD 21240
1	National Academy of Sciences ATTN: Dr. Donald Groves 2101 Constitution Ave, NW Washington, DC 20418
1	Aerospace Corporation ATTN: Tech Info Svcs Bldg 105, Rm 2220 P. O. Box 92957 Los Angeles, CA 90009
1	Agbabian Associates ATTN: Dr. J. Malthan 250 N. Nash Street El Segundo, CA 90245
1	AVCO Government Products Gr. ATTN: Dr. W. Bade 201 Lowell Street Wilmington, MA 01887
1	AVCO-Everett Research Lab ATTN: Technical Library 2385 Revere Beach Parkway Everett, MA 02149
1	John A. Blume & Associates ATTN: Dr. John A. Blume Sheraton-Palace Hotel 100 Jessie Street San Francisco, CA 94105
1	Calspan Corporation ATTN: Library P. O. Box 235 Buffalo, NY 14221
1	Effects Technology, Inc. ATTN: E. Anderson 5383 Holister Avenue Santa Barbara, CA 93105
1	General Electric Co. - TEMPO ATTN: DASIAC 816 State Street, Drawer QQ Santa Barbara, CA 93102
10	General Electric Co. - TEMPO ATTN: Dr. Lynn Kennedy 7800 Marble Ave, NE, Suite 5 Albuquerque, NM 87110
1	H-Tech Laboratories, Inc. ATTN: B. Hartenbaum P. O. 1686 Santa Monica, CA 90406
1	Hughes Aircraft Company Systems Development Lab ATTN: Dr. A. Puckett Centinela and Teale Streets Culver City, CA 92032

DISTRIBUTION LIST

No. of Copies	Organization
1	Ion Physics Corporation ATTN: Technical Library South Bedford Street Burlington, MA 01803
1	Kaman Sciences Corporation ATTN: Dr. D. Sachs 1500 Garden of the Gods Road Colorado Springs, CO 80907
1	Kaman Avidyne, Division of Kaman Sciences ATTN: Dr. J. Ray Ruetenik 83 2nd Ave, NW Indust'l Park Burlington, MA 01803
1	KTECH Corporation ATTN: Dr. Donald V. Keeler 911 Pennsylvania NE Albuquerque, NM 87110
1	Lockheed Missiles & Space Company, Inc. Division of Lockheed Aircraft Corporation ATTN: J. Nickell P. O. Box 504 Sunnyvale, CA 94088
1	Management Science Associates ATTN: Kenneth Kaplan P. O. Box 239 Los Altos, CA 94022
1	Martin Marietta Aerospace Orlando Division ATTN: A. Ossin P. O. Box 5837 Orlando, FL 32805
1	Maxwell Laboratories, Inc. ATTN: A. Kolb 9244 Balboa Avenue San Diego, CA 92123
1	McDonnell Douglas Astronautics Corporation 5301 Bolsa Avenue Huntington Beach, CA 92647
1	Philco Ford Corporation Aeronutronic Division ATTN: L. K. Goodwin Newport Beach, CA 92663
2	Physics International Company ATTN: Document Control Fred Sauer 2700 Merced Street San Leandro, CA 94577
3	R&D Associates ATTN: Tech Library Jerry Carpenter Allen Kuhl P. O. Box 9695 Marina del Rey, CA 90291
1	Sandia Laboratories ATTN: Dr. J. Kennedy P. O. Box 5800 Albuquerque, NM 87115
2	Science Applications, Inc. ATTN: Mr. J. W. Miller Dr. John Cockayne 8400 West Park Drive McLean, VA 22101
1	Shock Hydrodynamics, Inc. ATTN: L. Zernow 4710-16 Vineland Avenue N. Hollywood, CA 91602
1	Systems, Science & Software ATTN: Technical Library P. O. Box 1620 La Jolla, CA 92036

DISTRIBUTION LIST

No. of Copies	Organization
1	Teledyne-Brown Engineering ATTN: Dr. M. Batel Research Park Huntsville, AL 35807
1	Union Carbide Corporation Oak Ridge National Laboratory ATTN: Tech Library P. O. Box X Oak Ridge, TN 37830
1	URS Research Company ATTN: Technical Library 155 Bovet Road San Mateo, CA 94002
1	Battelle Memorial Institute ATTN: Technical Library 505 King Avenue Columbus, OH 43201
2	Denver Research Institute University of Denver ATTN: Mr. John Wisotski P. O. Box 10127 Denver, CO 90210
1	Director Applied Physics Laboratory The Johns Hopkins University Johns Hopkins Road Laurel, MD 20810
1	Lovelace Research Institute ATTN: Dr. D. Richmond P. O. Box 5890 Albuquerque, NM 87108
1	Massachusetts Institute of Technology Aerophysics Laboratory Cambridge, MA 02139
1	New Mexico Institute of Mining and Technology ATTN: Mr. P. McClain Socorro, NM 87801
1	Northwestern Michigan College ATTN: Prof. D.C.Kennard, Jr. Traverse City, MI 49584
1	Southwest Research Institute ATTN: Dr. W. Baker 8500 Culebra Road San Antonio, TX 78206
1	Stevens Institute of Tech Dept of Electrical Eng. ATTN: Prof. R. Geldmacher Castle Point Station Hoboken, NJ 07039
1	Research Institute of Temple University ATTN: Technical Library Philadelphia, PA 19144
1	Texas Tech University Dept of Civil Engineering ATTN: Mr. Joseph E. Minor Lubbock, TX 79409
1	University of Arkansas Department of Physics ATTN: Prof. O. Zinke Fayetteville, AR 72701
2	University of California Lawrence Livermore Laboratory Technical Information Division ATTN: Technical Library Dr. Donald N. Montan P. O. Box 808 Livermore, CA 94550

DISTRIBUTION LIST

No. of Copies	Organization
1	University of Illinois Consulting Eng. Services ATTN: Nathan M. Newmark 1211 Civil Engineering Bldg Urbana, IL 61801
1	University of Maryland Department of Physics ATTN: Dr. E. Oktay College Park, MD 20742
1	The University of Michigan Gas Dynamics Laboratory ATTN: A. Gabrijel Aerospace Engineering Bldg Ann Arbor, MI 48109
1	The University of New Mexico Eric H. Wang Civ Eng Res Fac ATTN: Technical Library University Station, Box 188 Albuquerque, NM 87131
1	University of Oklahoma Department of Physics ATTN: Prof. R. Fowler Norman, OK 73069

Aberdeen Proving Ground

Dir, USAMSAA
ATTN: Dr. J. Sperrazza
DRXSY-MP, H. Cohen
Mr. R. Norman, GWD
Cdr, USATECOM
ATTN: DRSTE-SG-H